FEM simulations of the deep drawing process

van de Koolwijk, H.P.M.

Award date:
1993

Technische Universiteit Eindhoven
Faculteit der Werktuigbouwkunde
Vakgroep Produktietechnologie & Automatisering
Laboratorium voor Omvormtechnologie

FEM simulations of the deep drawing process

H.P.M. van de Koolwijk

TUE Eindstudierapport

June 1993
VF code D3 WPA 1517

Professor: prof. ir. J.A.G. Kals

Coaches: prof. dr. T. Altan
ir. R.J.J.M. Sniekers

EXECUTIVE SUMMARY

The focus area of the FEM code DEFORM is simulating processes such as extrusion, cold and hot forging. If DEFORM is found to be applicable also in deep drawing and stretching processes, the application area is much wider. The applicability of DEFORM and the accuracy of the predictions is investigated by comparing the results both with other FEM codes and experimental data. The agreement is good, although DEFORM requires a high CPU time to perform the simulation.

The influence of the tool geometry on bending effects is investigated by performing simulations using both DEFORM and SHEET_FORM, which is a membrane code based on the Finite Difference Method (FDM) called SHEET_FORM. DEFORM uses solid elements thus bending effects are included, while SHEET_FORM neglects bending effects. From these simulations one can give an indication whether bending effects can be neglected or not for a certain ratio of die corner radius, r_d, over thickness, t. The results from the membrane code improve by adding a bending correction to the strain values of the nodes contacting the die corner radius, while the computational efficiency remains.

Furthermore the possibilities of the 3-D FEM code SHEETFORM-3D [Darendeliler, 1991] are investigated by simulating the deep drawing of a square cup and comparing important results such as thickness strains with experimental data. There are some discrepancies with the experiments, but the general trend matches satisfactory.

Experiments and FEM simulations of deep drawing a round cup using several ratios of punch radius, R_p, over initial sheet thickness t_0, (R_p/t_0) are conducted. The influence of the product size on the friction is investigated. For increasing product size, it is stated that the frictional induced shear stresses have an increasing influence on the radial stress distribution, and thus on the drawability.

PROJECT DESCRIPTION

TECHNISCHE UNIVERSITEIT EINDHOVEN
FACULTEIT DER WERKTUIGBOUWKUNDE
VAKGROEP PRODUKTIETECHNOLOGIE & AUTOMATISERING

Student:	H.P.M. van de Koolwijk
Professor:	Prof. ir. J.A.G. Kals
Coaches:	Prof. dr. T. Altan
	ir. R.J.J.M. Sniekers
Period:	july 1st 1992 - july 1st 1993
Title:	FEM simulations of the deep drawing process

Subject

The last decade many computer codes have been developed in order to simulate sheet metal forming processes and to predict forming severity. If the process modelling is accurate, repeatable and robust, it is possible to obtain realistic results and to test the formability of the parts before the dies are manufactured. This will help to achieve better process designs and to reduce the number of trial-and-error steps involved in conventional die design.

Instruction

The overall objective is to investigate the applicability of DEFORM to deep drawing and stretch forming by comparing the most important results such as strains, wall thickness and punch force distributions with experimental results and the results of other FEM codes such as ABAQUS.

After finishing these simulations and the evaluation, DEFORM will be applied to the study of bending effects and blank holder force effects. The goal is to develop a control strategy to determine an optimum blank holder force in order to increase the drawing ratio.

Professor	Coach
Prof. ir. J.A.G. Kals	ir. R.J.J.M. Sniekers

FOREWORD

In july 1992 I started the project described in this report at the Engineering Research Center for Net Shape Manufacturing in order to graduate at the mechanical engineering department of the Eindhoven University of Technology.

ERC/NSM is established on May 1, 1986 and is funded by the National Science Foundation and the member companies. The focus of the center is net shape manufacturing with emphasis on cost-effective manufacturing of discrete parts. In addition to conducting industrially relevant engineering research, the Center has the objectives to:

a) establish close cooperation between industry and faculty
b) train students, and
c) transfer the research results to interested companies

This report summarizes my research conducted at the Engineering Research Center for Net Shape Manufacturing at The Ohio State University, Columbus, Ohio. A more detailed description of the research is found in report ERC/NSM-S-93-15.

It turned out to be very interesting to work at The Ohio State University. I would like to thank everyone that helped me performing the research and finishing my thesis. Especially I want to thank my direct advisor dr. M.A. Ahmetoglu for his helpful and interesting discussions, and professor T. Altan who made it possible for me to work at the ERC. Furthermore I would like to thank professor J.A.G. Kals for giving me the freedom to conduct my research at the ERC and ir. R.J.J.M. Sniekers who is my coach at the Eindhoven University of Technology for his comments and advice.

LIST OF SYMBOLS

t, t_0	sheet thickness, initial thickness	[mm]
r_d	die corner radius	[mm]
R_d	die opening radius	[mm]
r_p	punch corner radius	[mm]
R_p	punch radius	[mm]
R_m	radius of middle axis	[mm]
R_n	radius of neutral axis	[mm]
Θ	bending angle	[-]
v_p	punch velocity	[m/s]
u, u_0	blank radius, initial blank radius	[mm]
l	length of fiber after deformation	[mm]
l_0	initial fiber length	[mm]
μ	Coulomb friction coefficient	[-]
BHF	blank holder force	[N, kN]
C	strength coefficient	[N/mm^2]
n	strain hardening exponent	[-]
E	Young's modulus	[N/mm^2]
R	normal anisotropy factor	[-]
ϵ_0	effective pre-strain	[-]
ϵ_{inner}	inner surface strain in radial direction	[-]
ϵ_{outer}	outer surface strain in radial direction	[-]
ϵ_{middle}	middle surface strain in radial direction	[-]
ϵ_b	bending strain	[-]
σ_f	yield stress	[N/mm^2]
σ_r	radial stress	[N/mm^2]
σ_ϕ	circumferential stress	[N/mm^2]
τ_0	frictional induced shear stress	[N/mm^2]
p_{BH}	blank holder pressure	[N/mm^2]
ß, $ß_0$	drawing ratio, initial drawing ratio	[-]

TABLE OF CONTENTS

CHAPTER 1 INTRODUCTION

The application of deep drawing processes is widely spread especially in the automotive industry. It is possible to produce complex products once a) the process parameters such as blank holder force, lubrication, b) tool parameters such as punch and die corner radii, and c) the material parameters are optimized. Until recently, optimizing and adjusting of these parameters was mostly done by experimental trial-and-error method, which is a time and money consuming process.

By using analytical methods like the upper bound theory, one can model the process and easily see the influence of the process-, material- and tool parameters. However, this is only possible for relatively simple parts or products, for example round cups or plane-strain deep drawing.

Another method to predict the strains and the influence of the process and tool parameters, is simulating the deep drawing process using the Finite Element Method (FEM). By performing numerical simulations the number of experimental trial-and-errors can often be reduced. Advantages of using numerical methods are:

a) the method has the capability to overcome complexities arising from geometrical and material non-linearities
b) the deformation can be predicted and optimized before machining the tooling
c) complex non-symmetric geometries can be analyzed when using 3D-FEM codes

Disadvantages of FEM codes are:

a) a well educated operator is required to use the program and interpret the predicted results
b) in general, the required computation time is high
c) one still can not solely rely on the predicted results thus experimental verification of the numerical predictions is still necessary

In this report four topics are investigated, which are listed below:

a) the applicability of DEFORM in deep drawing
b) investigation of influence of toolgeometry on bending effects

c) 3-D FEM simulations of deep drawing a square cup

d) investigation of influence of product size and friction on deep drawing process

Ad a): The applicability of the FEM code DEFORM in deep drawing is investigated in this report by performing several simulations. DEFORM is developed to simulate billet forming processes such as forging and extrusion. If one can also simulate deep drawing processes, the application area is wider and more general.

Ad b): An important parameter influencing the amount of bending in deep drawing is the ratio of die corner radius r_d over the sheet thickness t, which is written as the r_d/t ratio. The bending strains can reach significant values for small r_d/t ratios. Fig. 1.1 shows the three areas in which bending occurs when deep drawing a round cup. As draw-in starts, the sheet located under the blank holder bends over the die corner radius (area 1), then slides over the die corner radius and enters the unsupported region where it is straightened and unbent (area 2). The sliding and unbending causes some strain hardening in the unsupported region, thus higher strains. Since there is hardly sliding over the punch corner radius in axisymmetric deep drawing, no sliding and unbending occurs but only bending over the punch corner radius (area 3).

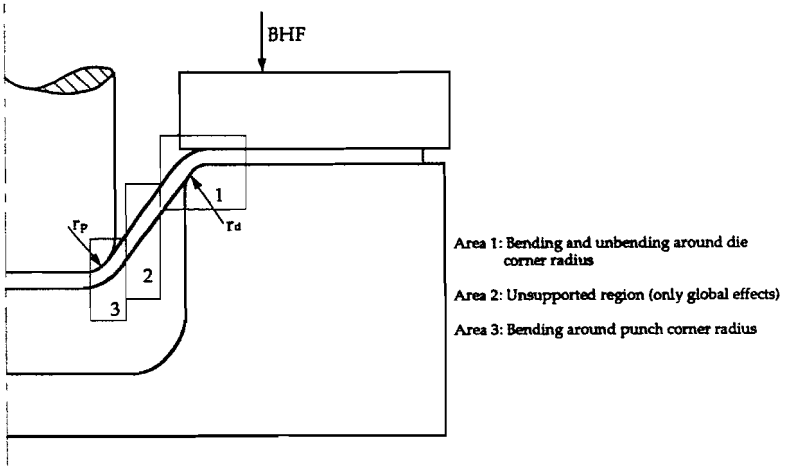

Fig. 1.1 Deep drawing of a round cup with the three bending areas

Membrane based FEM codes neglect bending effects while solid or shell based codes include them. Using either solid or shell codes increases the CPU time but the results are more realistic. Simulations using DEFORM are performed using different die corner radii to investigate the effect on bending strains. From these results it is possible to provide an

indication for which r_d/t ratio the bending strains are small enough to be neglectable. In that case one can use a fast membrane code without getting inaccurate.

To improve the results from a membrane code, a bending correction can be included. Then the bending strain is added to the radial strain values of the nodes of the sheet contacting the die corner radius. The improvement of adding bending correction is investigated by performing three simulations using different r_d/t ratios both with DEFORM and SHEET_FORM and comparing the radial strains from DEFORM with those from SHEET_FORM, where SHEET_FORM is equipped with the bending correction. If the comparison is satisfactory, the computational efficiency of the membrane code remains while obtaining more realistic results.

Ad c): For the analysis of complex geometries, 3-D FEM codes are developed. For example in the automotive industry very complex parts are deep drawn. The 3-D FEM code SHEETFORM-3D is used in simulating deep drawing of a square box. First of all the results are compared with experiments performed by [Darendeliler, 1991] to get an impression of the accuracy of SHEETFORM-3D. Secondly, the influence of the BHF on thickness strain is investigated by performing three simulations using a different BHF in deep drawing a square cup. The two major failure modes in deep drawing are the occurrence of wrinkling and necking (fracture). Preventing failure is mainly done by adjusting the blank holder force (BHF) in such a way that the BHF is high enough to prevent wrinkling and low enough to prevent fracture. So there is a certain range in which the BHF should be. The thickness strain can be a criteria to predict fracture.

ad d): Additionally to the research conducted at the ERC/NSM, the influence of the product size and friction on the deep drawing process is investigated. The total power needed to draw a cup can be divided into power required to overcome a) deformation in the flange, b) bending, sliding, and unbending over the die corner radius, and c) friction in the flange and d) friction over the die corner radius. For an increasing product size it can be stated that the part of the power due to friction increases, [Doege, 1992]. Thus, the increase of the product size increases also the radial stress in the flange. Both experiments and FEM simulations are performed, using several product sizes to investigate the effect on the friction.

CHAPTER 2 APPLICATION OF "DEFORM" IN DEEP DRAWING

The FEM code DEFORM is developed by Oh et al., [1991], to simulate billet forming processes. To investigate the applicability of DEFORM in sheet metal forming, axisymmetric and plane-strain deep drawing (with hemispherical and cylindrical punches) and plane-strain stretch forming are simulated by the author using DEFORM. The results are compared both with other FEM codes and experiment to investigate the accuracy of DEFORM. In Chapter 2 of ERC/NSM-S-93-15 a introduction concerning the deep drawing process and FEM codes is described. In Chapter 3 of ERC/NSM-S-93-15, pp. 35-62 an extended description of the comparison is found.

2.1 DEFORM compared with benchmark test

A benchmark test for sheet metal forming analyses has been performed by twenty five research groups and the results were published by Lee et al., [1990]. To compare with the benchmark test, axisymmetric deep drawing using a hemispherical punch as shown in Fig. 2.1 is simulated in DEFORM. The blank is defined by 1120 elements, four elements are defined in thickness direction to obtain strain distributions in thickness direction.

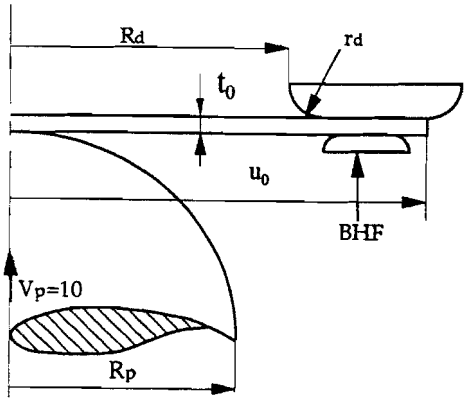

R_p	= 50.8 mm
r_p	= 50.8 mm
R_d	= 53.8 mm
r_d	= 6.35 mm
u_0	= 80 mm
t_0	= 1 mm
BHF	= 69 kN
C	= 589 N/mm^2
μ	= 0.15
ϵ_0	= 10^{-4}
n	= 0.216

Fig. 2.1 Geometry and process parameters as used in Benchmark test

In the comparison with DEFORM the results of some codes were cut and not considered since their predictions of the radial strain distribution were far out of the reasonable range and thus very questionable. The radial strains at a punch travel of 40 mm for both the benchmark test results and DEFORM are shown in Fig. 2.2. The DEFORM prediction is nearly within the range of reasonable benchmark test results. The CPU time to perform the simulation is about 70 hours on a HP700s workstation. More information and results can

be found in ERC/NSM-S-93-15, pp. 41-49. Another comparison with the Benchmark test simulating plane-strain stretch forming is described in ERC/NSM-S-93-15, pp. 57-62.

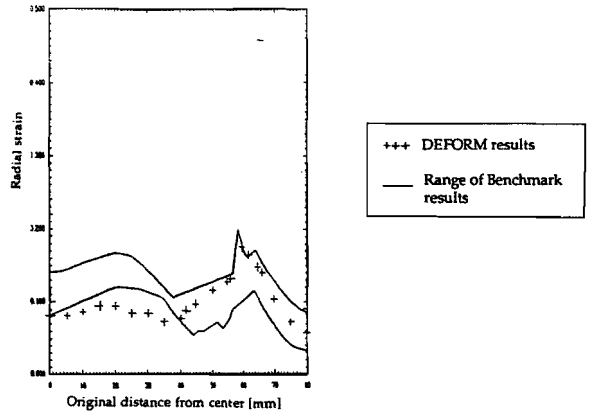

Fig. 2.2 Radial strain distribution for both DEFORM and benchmark test results

2.2 DEFORM compared with ERC experimental results

Ahmetoglu et al., [1992] conducted experiments of deep drawing a round cup using High Strength Galvanized steel. The geometry is shown in Fig. 2.3. DEFORM is used to simulate the experiment. The blank is defined by 2436 elements, four elements in thickness direction. The outer surface radial strains of the cup for both the experiment and simulation at a punch travel of 60 mm are shown in Fig. 2.4. The general trend matches well with the experiment. Some jumps in the experimental strain values occur, probably due to inaccurate measurements. More information can be found in ERC/NSM-S-93-15, pp. 52, and pp. 56-58.

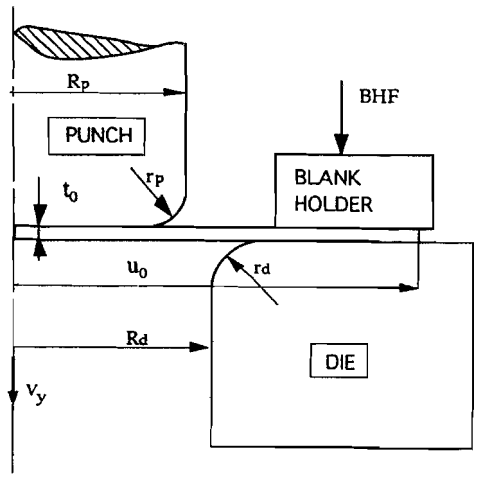

R_p	= 76.2	mm
r_p	= 20.07	mm
R_d	= 53.8	mm
r_d	= 79.12	mm
u_0	= 127	mm
t_0	= 0.889	mm
BHF	= 117	kN
C	= 603.8	N/mm^2
μ	= 0.13	
ϵ_0	= 3.28*10^{-4}	
n	= 0.143	
R	= 1.4 (normal anisotropy)	

Fig. 2.3 Geometry and process parameters as used in experiment and DEFORM simulation

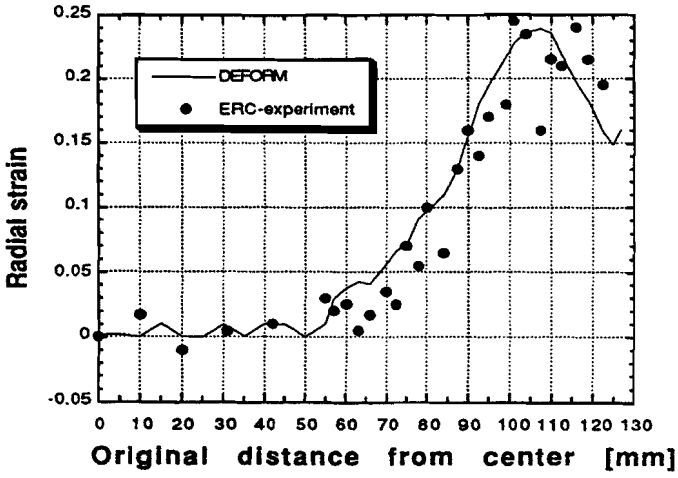

Fig. 2.4 Radial strain for both DEFORM and experiment at 60 mm punch travel

2.3 DEFORM compared with ABAQUS

A simulation where DEFORM is compared with ABAQUS results in deep drawing a round cup can be found at pp. 47-55 of ERC/NSM-S-93-15. The wall thickness variation is compared, and is shown in Fig. 2.5 for both DEFORM and ABAQUS. During the iteration, a lot of contact changes occur under the punch, which increases the CPU time. In order to reduce the contact changes, two different DEFORM simulations are performed, one where a pressure of 2.5 MPa (called DEFORM-pressure) is specified under the punch nose and one where a velocity (magnitude and direction equal to punch velocity, called DEFORM-velocity). The strain distributions from these two DEFORM simulations are quite similar, however, in the necking area around the punch corner radius are some differences.

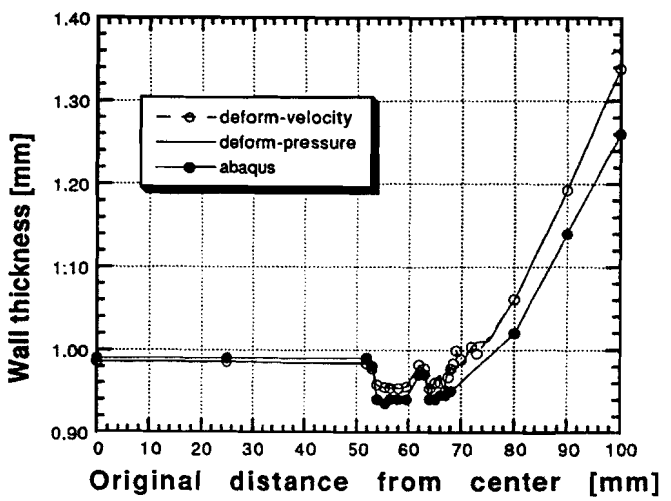

Fig. 2.5 Wall thickness variation for both DEFORM and ABAQUS results

2.4 Conclusions and comments considering DEFORM in deep drawing

In general, the results obtained with DEFORM such as strain distributions are satisfactory. The comparison with experiments as well as with other FEM codes is found to be good.

The CPU time for these above described DEFORM simulations is between 70 to 140 hour on a HP700s workstation, depending on number of elements, blanksize, stroke and tool geometry.

First reason for the high CPU time are the contact changes, which occur between:
a) the blank and both the die and blank holder
b) the punch and blank.

During the simulation, contact between blank and tools change from closed to open, i.e. from contacting to no contact. In order to proceed to the next iteration step, the contact condition has to be stabilized which means no contact changes may occur. To reduce the number of contact changes, the sheet is clamped at the punch by specifying a pressure under the punch. In the area around the flange a velocity field is specified for the nodes of the blank contacting the die. The velocity of these nodes on the flange in vertical direction is defined to be zero. Now these nodes can not move in y-direction and therefore the number of contact changes is reduced and thus the contact is more stabilized.

Another reason for the high CPU time is the automatic mesh generator. It is only possible to define elements which have about the same length as height. This is preferable in billet forming. However in sheet metal forming the blanks are mostly thin, thus it is preferrable to use rectangular or oblong elements. The total number of elements needed to define the blank increases when using square elements, especially when specifying several layers of elements in thickness direction. Depending on a) blank diameter, b) sheet thickness, and c) the desired number of elements in the thickness direction, the number of elements can reach up to 2500. Rectangular or oblong elements would reduce the number of elements significantly and thus the CPU time, since the CPU time increases for an increasing number of elements.

CHAPTER 3 INFLUENCE OF GEOMETRY ON BENDING

3.1 Introduction

The main parameters affecting the amount of bending strain in axisymmetric deep drawing are a) the blank holder force and b) the ratio of die corner radius r_d over sheet thickness t (r_d/t ratio). In this paragraph only the effect of the r_d/t ratio is investigated. Several papers subscribe and confirm the significance of the die corner radius on the bending effects and thus on the strain distributions, such as Stoughton, [1985], and Ohwue, [1991]. During a deep drawing operation, bending occurs in different areas. The part of the sheet which is originally located under the blank holder undergoes three types of deformation as draw-in continues. First the sheet bends over the die corner radius, then it slides over the die corner radius. After that it is straightened and unbent as it enters the unsupported region, i.e. the wall of the cup. Thus, the portion of the sheet located at the unsupported region shows an increased effective and radial strain, due to this bending, sliding and unbending. The part of the sheet located at the punch nose only bends over the punch corner radius, if the punch is axisymmetric there is little sliding and unbending over the punch corner radius. The influence of the die corner radius is investigated by the author by performing simulations using both DEFORM and the membrane Finite Difference Method SHEET_FORM. A more extended description of this topic is found in ERC/NSM-S-93-15, pp. 63-97.

The objectives of these investigations are:

a) Investigate the influence of the ratio of the die corner radius, r_d, over sheet thickness, t, (r_d/t) on the radial strain distribution.

b) Compare the results of the modified membrane code SHEET_FORM after the bending correction is added to the strain values of the nodes contacting the die corner radius with DEFORM.

c) Determine a minimum value for the r_d/t ratio for which bending effects can be neglected and one thus can use the membrane formulation.

Considering a sheet bent over the die corner radius (under plane-strain conditions) as shown in Fig. 3.1. The pure bending strain ε_b at the outer side of a sheet bent over the die corner radius is calculated according to Equation 3.1, when no restraining force is considered, where '+' is for convex surfaces and '-' for concave surfaces (if the reference point is the

center of the die corner radius), [Wang, 1992].

$$\epsilon_b = \ln\left(\frac{l}{l_0}\right) = \ln\left(1 \pm \frac{t}{2R_m}\right) \tag{3.1}$$

The influence of the r_d/t ratio on the bending strain can be seen from this equation. The radius of the middle axis R_m ($R_m = r_d + {}^1/_2.t$) is assumed to be equal to the radius of the neutral axis. According to Equation 3.1, the bending strain is significant for small r_d/t ratios.

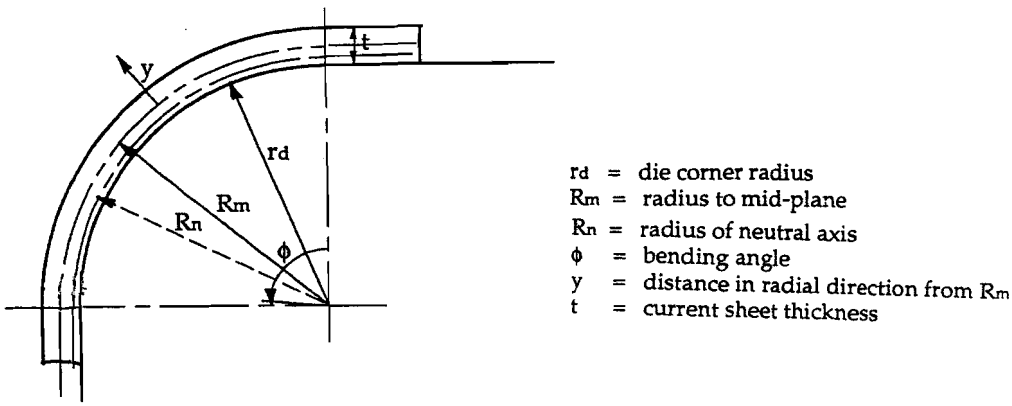

Fig. 3.1 A sheet bent over the die corner radius

3.2 DEFORM simulations using different r_d/t ratios

Simulations using different values of the r_d/t ratio are performed using DEFORM to investigate the influence of the r_d/t ratio on the bending strain. The tool geometry and process parameters for these three r_d/t ratios are shown in Table 3.1, and the material properties of the High Strength Galvanized steel are equal to the properties specified in Fig. 2.3.

Table 3.1 Process parameters as used in axisymmetric simulations

Name in graphs	r_d [mm]	r_d/t [-]	t [mm]	R_d [mm]	R_p [mm]	r_p [mm]	R [mm]	μ [-]	BHF [kN]
AX18	16	18	0.889	79.12	76.2	20	127	0.13	117
AX9	8	9	0.889	79.12	76.2	20	127	0.13	117
AX5	4.45	5	0.889	79.12	76.2	20	127	0.13	117

The radial strains at a punch stroke of 45 mm are shown in Figures 3.2, 3.3, and 3.4 for AX18, AX9, and AX5. The peaks of the outer and inner layer strain located in the area around the die corner radius are obviously increasing for decreasing r_d/t ratios.

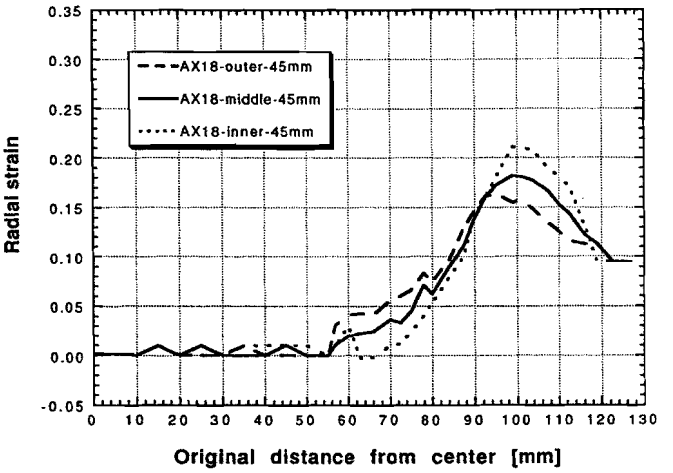

Fig. 3.2 Radial strain distribution for AX18 at 45 mm punch travel

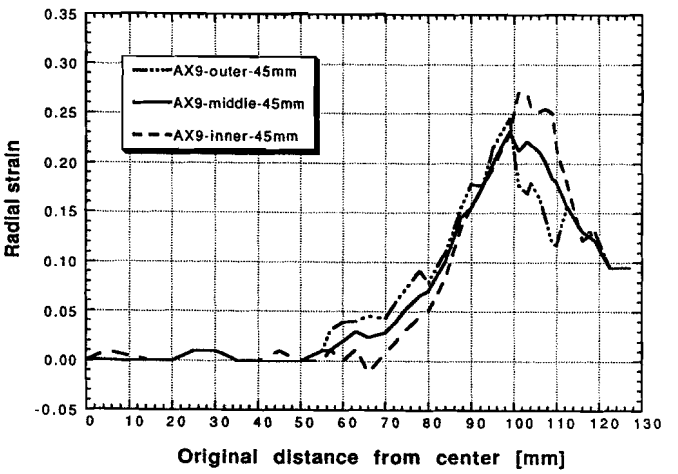

Fig. 3.3 Radial strain distribution for AX9 at 45 mm punch travel

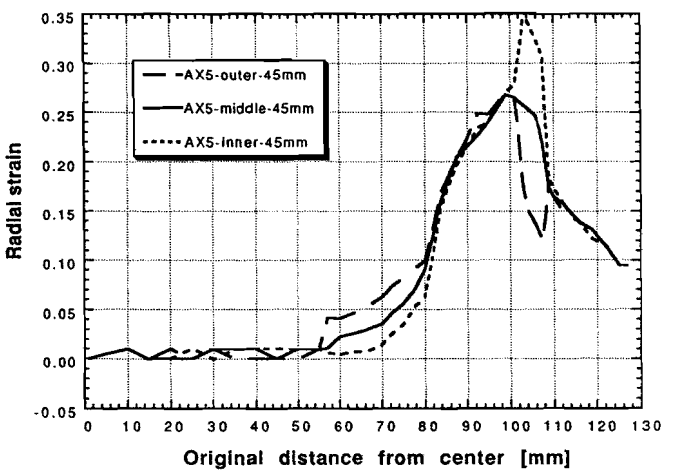

Fig. 3.4 Radial strain distribution for AX5 at 45 mm punch travel

The comparison of the bending strain from DEFORM with the theoretical bending strain as in Equation 3.1 is shown in Fig. 3.5, where the bending strain at the inner surface is calculated as (ε_{inner} - ε_{middle}) and the bending strain at the outer surface as (ε_{outer} - ε_{middle}). Fig. 3.5 shows that the trend of the DEFORM results matches the theoretical values (from Equation 3.1) reasonable, but there are some irregularities. A first reason is that the sheet has no constant bending radius. The sheet is not fully contacting since the bending angle is not equal to 90 degrees. This increases the bending radius and thus the bending strain decreases. When using the theoretical values from Equation 3.1, it is assumed that in the bending area the sheet has a constant bending radius. The second reason is that Equation 3.1 is only valid for plane-strain bending without tension, while the drawn cup is axisymmetric. Furthermore, no shift of the neutral axis is considered when using Equation 3.1, while the blank holder force generates a tensile force in the cup. The load-stroke diagrams are shown in Fig. 3.6. There is an increase in the required punch load as the r_d/t ratio decreases, due to the increased force needed to bend and unbend the sheet.

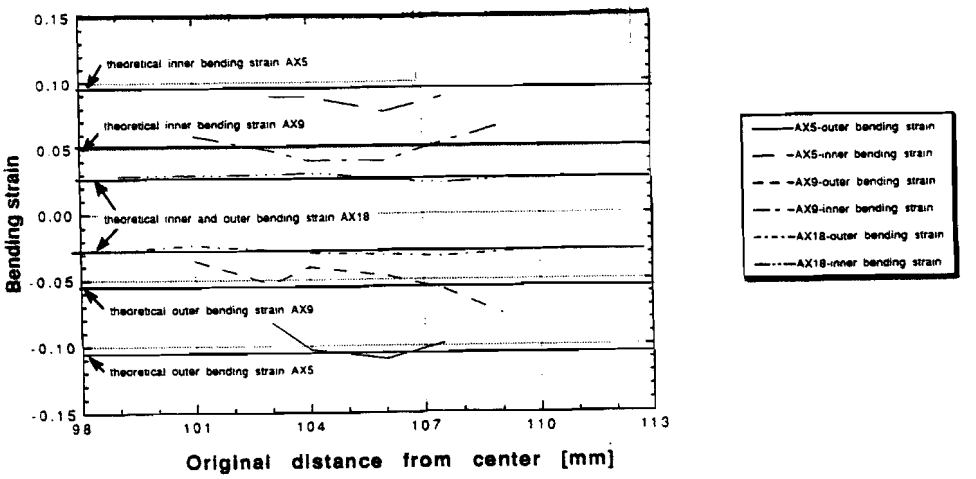

Fig. 3.5 Bending strain from DEFORM and theoretical bending strain 45 mm stroke

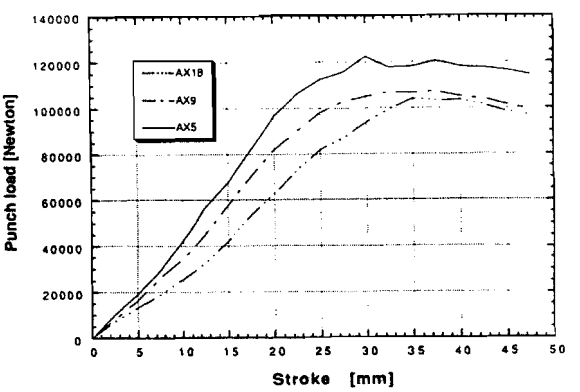

Fig. 3.6 Load-stroke diagrams for AX18, AX9, and AX5

3.3 SHEET_FORM simulations using different r_d/t ratios

The same processes as described before (AX18, AX9 and AX5) are simulated by the author using the FDM membrane code SHEET_FORM [Ahmetoglu, 1990]. The objectives are:

a) the agreement of SHEET_FORM with DEFORM for different r_d/t ratios

b) the improvement achieved by adding the bending correction in SHEET_FORM.

In SHEET_FORM the strain values of the nodes contacting the die corner radius are corrected at the inner and outer layer of the sheet. At these nodes, the radius is determined and the bending strain is calculated using Equation 3.1 and added to the membrane strain. Figures 3.7, 3.8, and 3.9 show the radial strain distributions for both SHEET_FORM and DEFORM.

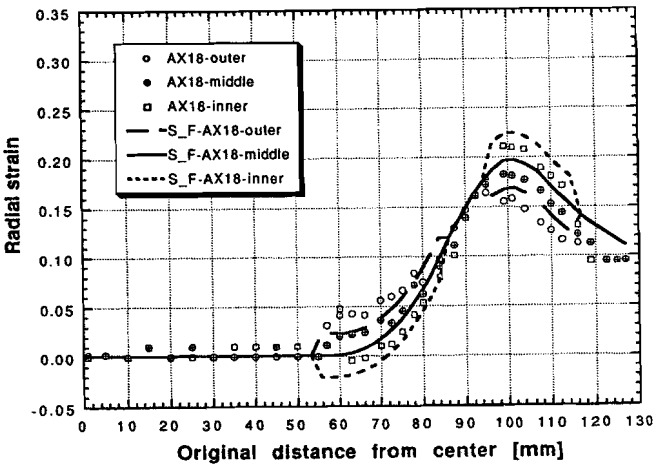

Fig. 3.7 Radial strain distribution for AX18 (r_d/t = 18), where the symbols represent DEFORM and the lines SHEET_FORM

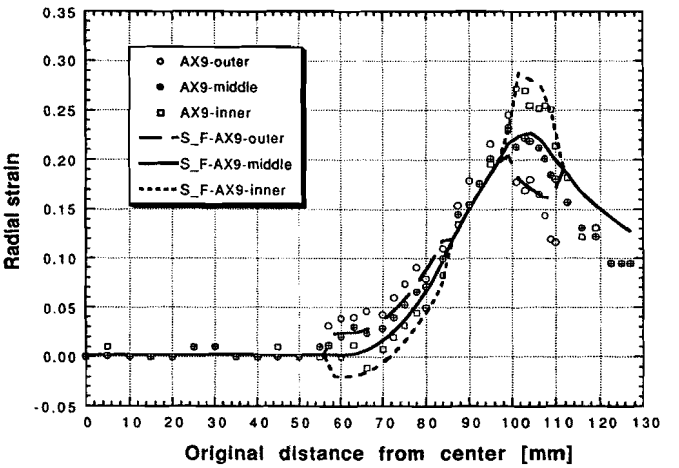

Fig. 3.8 Radial strain distribution for AX9 (r_d/t = 9) where the symbols represent DEFORM and the lines SHEET_FORM

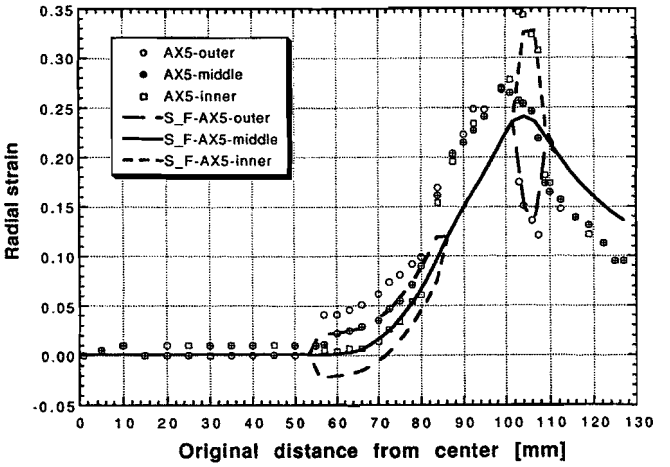

Fig. 3.9 Radial strain distribution for AX5 (r_d/t = 5) where the lines represent DEFORM and the lines SHEET_FORM

For AX18 (Fig. 3.7) the agreement of SHEET_FORM with DEFORM is satisfactory, however for AX5 (Fig. 3.9) the difference in the strain values of the nodes located at the unsupported region is high, because of a) the strain hardening effect which is not included in the bending correction method, b) the sheet has no constant bending radius in deep drawing while it is assumed to be constant in the bending correction and c) the bending correction is actually only valid for plane-strain bending where furthermore the tension due to the friction in the flange area is not considered. For plane-strain cases two simulations using DEFORM and SHEET_FORM are performed, where a r_d/t ratio of 9 and 5 is defined. Additional information can be found in paragraph 4.5 of ERC/NSM-S-93-15, pp. 87-99.

3.4 Conclusions considering bending effects

The bending strain increases significantly for decreasing r_d/t ratios. For AX18 the logarithmic bending strain is about 2 to 3%, for AX9 from 4 to 7%, and for AX5 in the range of 8 to 11%. For r_d/t ratios larger than 9, bending effects can be neglected and thus one can use a fast membrane code. When using a membrane code the predictions of the radial strain distributions improve by including bending correction.

CHAPTER 4 3-D SIMULATIONS OF DEEP DRAWING A SQUARE BOX

Initially, one of the goals of the project was to study the blank holder force effects and to develop a control strategy using DEFORM. Due to the very high CPU time, DEFORM will hardly be used to perform deep drawing simulations. Furthermore it would not be possible for the author to develop and test this control strategy within the available time. Instead of that, deep drawing of a square box is simulated using the implicit 3-D FEM membrane code SHEETFORM-3D developed by Darendeliler, [1991]. The advantage of 3D codes is the ability to simulate complex geometries, such as square and rectangular boxes. SHEETFORM-3D uses constant strain triangular elements. First of all a comparison with experiments is made, secondly the influence of the blank holder force on thickness strains is investigated. Additional information about this topic can be found in ERC/NSM-S-93-15, pp. 100-120.

4.1 Comparison with experiments

Deep drawing of either square or rectangular boxes is far more complicated than axisymmetric cups, since the deformation states and the metal flow vary along the periphery of the box. A simulation using the geometry and process parameters as shown in Fig. 4.1 is performed and compared at a punch travel of 20 mm with experiments conducted by Darendeliler, [1991]. The CPU time on a CRAY supercomputer is about an hour, which is relatively high. The thickness strains in both horizontal direction (line y-y in Fig. 4.1) and diagonal direction (line y-x in Fig. 4.1) are shown in Fig. 4.2 and Fig. 4.3 respectively. The predicted trend matches with the experiments, however there are differences

4.2 Influence of blank holder force on thickness strain

The blank holder force (BHF) significantly affects the process. Once the BHF is too low, wrinkling may occur under the blank holder, but if the BHF is too high fracture may occur in the corners at the punch nose. Thinning or necking can be predicted by a high peak in the thickness strain located in the vicinity of the punch corner. In order to investigate the influence of the BHF on the thickness strain, three simulations are performed using a BHF of 0.82 kN, 1.64 kN and 5 kN respectively. Sommer's [1986] empirical relation for the required BHF results in a BHF of 1.64 kN. The thickness strains in diagonal (y-x) direction

and horizontal direction (y-y) are shown in Fig. 4.4 and Fig. 4.5 respectively. These figures show that the maximum thinning occurs in the diagonal direction while the maximum

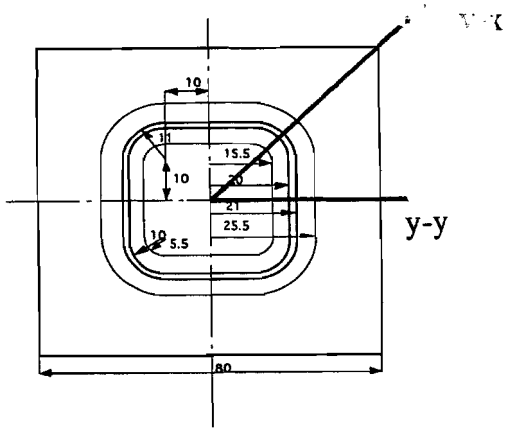

Deep Drawing Steel:

C	= 560	N/mm^2
μ	= 0.04	
ϵ_0	= 0.0135	
n	= 0.27	
E	= 210,000	N/mm^2
t_0	= 0.75	mm

Fig. 4.1 Geometry and process parameters as used in simulation and experiment

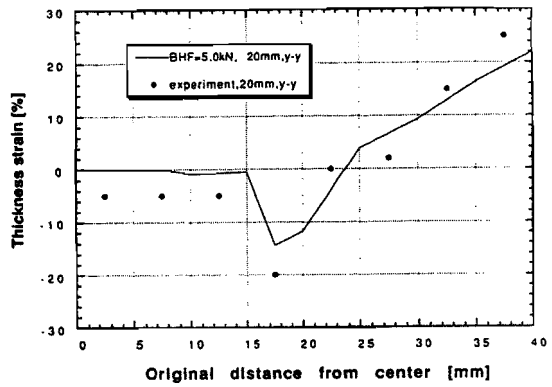

Fig. 4.2 Thickness strain in horizontal direction (y-y) at 20 mm stroke for experiment and SHEETFORM-3D simulation

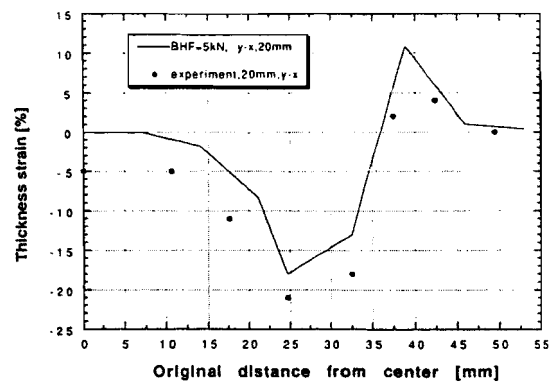

Fig. 4.3 Thickness strain in diagonal direction (y-x) at 20 mm punch travel for both experiment and SHEETFORM-3D simulation

thickening in the flange occurs in the horizontal direction. Note that the thickness strain

distributions are only valid for this specific geometry. Depending on parameters such as punch corner radius, maximum thickening may occur in the corner instead of the side wall. Furthermore the thinning increases for increasing blank holder force. The thickening in horizontal and diagonal direction decreases for increasing blank holder force, since there is less draw-in and thus less compressive stresses.

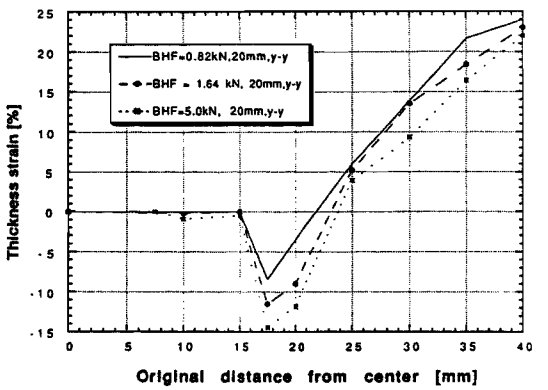

Fig. 4.4 Thickness strain in diagonal direction for BHF of 0.82 kN, 1.64 kN and 5 kN

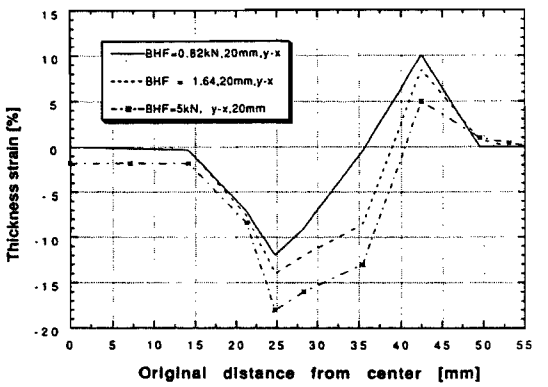

Fig. 4.5 Thickness strain in horizontal direction for BHF of 0.82 kN, 1.64 kN and 5 kN

4.3 Conclusions considering deep drawing a square box using SHEETFORM-3D

In the comparison with the experiments, it is found that the trend of the thickness strain matches. However quantitatively there are differences due to:a) the large elements (chosen to reduce the CPU time) and b) some parameters such as C, n, ε_0, μ may be different from the experimental value, thus it is important to determine these parameters as accurate as possible. The BHF affects the thickness strain significant. For an increasing BHF, the thickening in horizontal and diagonal direction decreases, while the thinning decreases.

CHAPTER 5 INFLUENCE OF PRODUCT SIZE AND FRICTION

5.1 Introduction

In addition to the research conducted at the ERC/NSM, deep drawing experiments and FEM simulations using ABAQUS were performed at the Eindhoven University of Technology. Objective was to investigate the combined influence of the product size and the friction in the flange on the deep drawing process.

In order to investigate the influence of the product size and friction on drawability, the relative product size is used. The relative product size can be defined as the ratio of punch radius R_p over the initial sheet thickness, t_0, i.e., the R_p/t_0 ratio. When using this ratio, a reduction of the thickness has the same effect as an increase of the punch radius with the same factor. When performing experiments the advantage is that by varying the initial sheet thickness, the relative product size is varied, without changing the toolings. Thus one can vary the relative product size fast and at low costs in experimental investigations.

5.2 Friction in the flange of a cup

The total power required to draw a cup is divided into:

a) the power to compress the flange, i.e. to reduce the flange diameter
b) the power to bend, and unbend the sheet over the die corner radius
c) the power to overcome the friction in the area around the die corner radius
d) the power to overcome the friction in the flange

As the relative product size increases, the part of the total power due to friction in the flange will increase, [Doege, 1992]. A cup with initial sheet thickness t_0 is drawn, where in Fig. 5.1 the shear stresses in the blank and the frictional stresses acting on the flange are shown. The blank holder force creates a frictional induced shear stress on the surfaces between blank and both die and blank holder. Due to the frictional induced shear stresses, there is an increase in the radial stress in the flange. The values of the frictional stresses are independent of the sheet thickness. The increase of the radial stress due to frictional stresses however depends on the sheet thickness. A decrease in sheet thickness (which is an increase of relative product size) results in an increase in the radial stress.

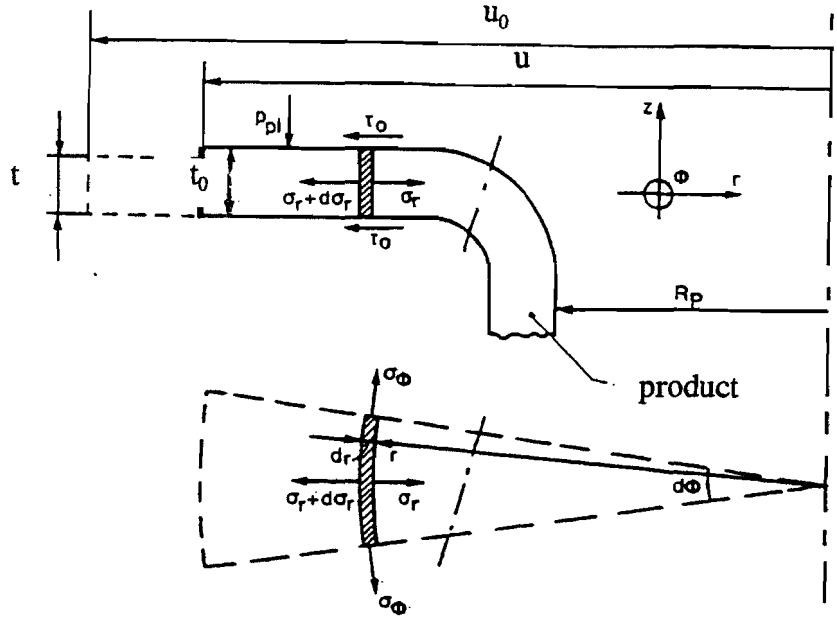

Fig. 5.1 The stresses acting on the flange of a cup, [Ramaekers, 1988]

If the relative product size keeps on increasing, the radial stress increases until the critical stress is reached. Then the radial stress is too high and fracture will occur. The location of the fracture is in the vicinity of the punch corner radius, because the sheet is not as much strain hardened as the sheet located in the unsupported region, and therefore the weakest.

The combined influence of the relative product size and friction on total power is subscribed by Equation 5.1. It describes the force needed for the deformation in the flange. The parameter $\mu p_{BH} R_p/t_0$ shows clearly the combined influence of relative product size and friction on the required power. The required force increases linearly with the $\mu p_{BH} R_p/t_0$ parameter. Equation 5.1 is derived in Appendix 2, similar to [Ramaekers et al., 1988] except for the friction model. Coulomb friction is used instead of Von Mises friction.

$$F^*_{flange} = 1.1 \sqrt{\frac{\beta_0}{\beta} \ln\beta + 2\mu\, p_{BH} \frac{R_p}{t_0} \{ \beta - 1 \}} \tag{5.1}$$

5.3 Experimental investigations

In the experiments the BHF is varied for several initial sheet thicknesses t_0 investigate for which value of the BHF fracture will occur. By varying the initial sheet thickness, the relative product size is varied. St. 12 is used, and tensile tests are performed in three directions (0°, 45°, and 90°) to obtain the material properties. The material properties and the geometry of the tool and blank are shown in Fig. 5.2. The properties are needed since

FEM simulations will be performed and compared with experimental results.

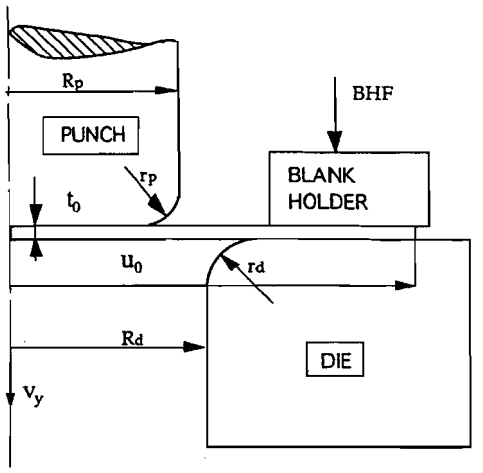

	C [N/mm²]	n [-]	R [-]	ϵ_0 [-]
0°	514	0.25	1.62	0.0
45°	522	0.25	1.14	0.00348
90°	507	0.25	1.95	0.0
Average	514	0.25	1.57	0.00116

R_p = 25 mm
r_p = 7 mm
R_d = 27.6 mm
r_d = 3.5 mm
u_0 = 48.9 mm
t_0 = 0.5 mm for relative product size of 100
t_0 = 1.0 mm for relative product size of 50
t_0 = 1.5 mm for relative product size of 33.3
t_0 = 2.0 mm for relative product size of 25
μ = 0.08 (die/blank) in FEM simulation
μ = 0.15 (punch/die) in FEM simulation

Fig. 5.2 Geometry of the tooling and material properties as used in experiments

The criteria in the experiments and simulations is whether fracture occurs. Fig. 5.3 shows for several relative product sizes at what BHF fracture occurs. For decreasing product size, the maximum BHF before fracture increases. Since the relative product size is varied by changing the sheet thickness, the blank area remains unchanged. Thus the BHF is directly related to the blank holder pressure and to the frictional induced shear stresses when using Coulomb friction. The influence of the friction increases as the product size increases.

5.4 FEM simulations

FEM simulations of these above described experiments are performed using ABAQUS to investigate whether the simulations show a similar trend as the experiments. Appendix 3 describes these simulations more detailed. In Fig. 5.3 the results from the simulations are shown. Fracture can be detected in ABAQUS by observing the elements located at the punch corner radius. If fracture occurs these elements are extremely elongated and thinned. The trend is similar with the experiments, however, fracture does not occur at the same BHF as in the experiments, probably due to the selected coefficient of friction. It is very hard to determine the coefficient of friction in deep drawing accurately. In the punch/blank surface, μ = 0.15 is selected, and in the die/blank surface μ is chosen as 0.08. In the experiments μ is probably about 0.05 in the die/blank surface. This shows again the importance of the friction in deep drawing.

5.5 Conclusions on influence of product size and friction on deep drawing

Using both the results from experimental and numerical methods learns the influence of relative product size and friction on drawing process. For an increasing productsize, the part of the total power needed to overcome the friction increases. Due to this increase fracture occurs at a lower BHF.

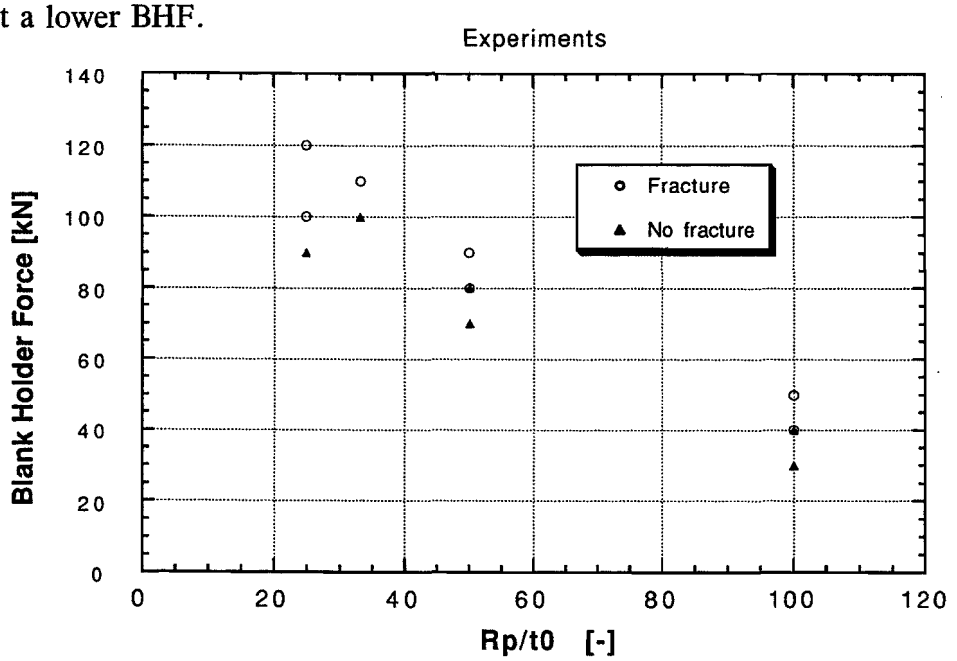

Fig. 5.2 The combined influence of relative product size and friction on drawability from experimental investigation

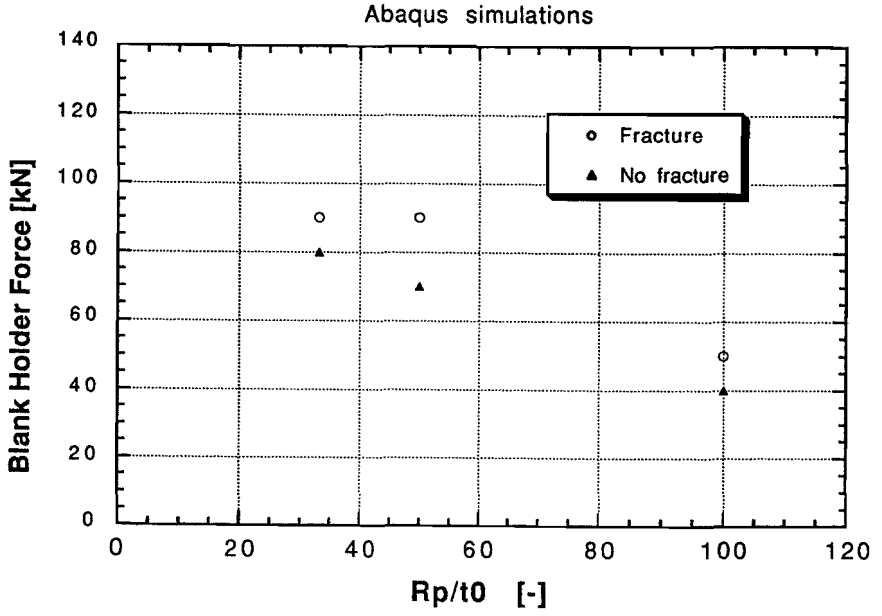

Fig. 5.3 The combined influence of relative product size and friction on drawability from FEM simulations using ABAQUS

CHAPTER 6 CONCLUSIONS AND RECOMMENDATIONS

In the comparison of DEFORM with an experiment and other FEM codes, the accuracy of the results obtained with DEFORM, such as strain distributions and load-stroke diagrams were found to be satisfactory. However, the CPU time when using DEFORM in simulating deep drawing is too high for practical use ($>$ 70 hours on a HP700s workstation) due to: a) the large number of elements required to model the blank and b) the contact conditions that have to be satisfied in DEFORM. A decrease in CPU time can be achieved by modifying: a) the mesh generator and b) the contact formulation

For small r_d/t ratios (smaller than 9) bending effects are significant and can not be neglected. For r_d/t ratios larger than 9, membrane codes provide good results. The disagreement of the results of the membrane code SHEET_FORM with those of the solid code DEFORM can reach up to 30% of the strain value for a ratio of 5.

Adding local bending correction to membrane codes improves the prediction of the surface radial strains. However, for small r_d/t ratios there are still discrepancies because a) the correction is only valid for plane-strain geometries, b) no shift of the neutral axis due to tensile force is considered, c) the bending radius is not constant as assumed in the correction, and d) strainhardening is not included in the correction. Thus, one should use a solid or shell based code for small r_d/t ratios (<9) to obtain realistic strain distributions.

In simulating deep drawing of a square cup by using SHEETFORM-3D, the trend of the thickness strain matches reasonable with the experimental results. However, due to the use of large elements and possible inaccuracies in the experimental determination of parameters such as C, n, and μ, there are still quantitative discrepancies. Furthermore the BHF significantly affects the thickness strain. If the BHF is doubled, the maximum thickness strain increases up to 35% of the calculated value for the specific investigated geometry.

The inluence of relative product size and friction on deep drawing process is investigated by performing both experiments and FEM simulations. The relative product size R_p/t_0 and friction (μp_{BH}) significantly affect the drawability. For an increasing product size, the radial stress in the flange increases due to the increased influence of the parameter $\mu p_{BH} R_p/t_0$ on the total required power. Therefore fracture occurs at a lower BHF.

LIST OF REFERENCES

Ahmetoglu, M.A., 1990, Kinzel, G.L., and Altan, T., *"Sheet Metal Forming Processes, State of the Technology and Analysis"*, Report No. ERC/NSM-S-90-46, Ohio State University, Columbus, OH

Ahmetoglu, M.A., 1992, Coremans, A.L.P., Kinzel, G.L. and Altan, T., *"Deep Drawing of Round Cups using Variable Blank Holder Force (BHF)"*, Report No. ERC/NSM-S-92-50, Ohio State University, Columbus, OH

Darendeliler, H., 1991, Ph.D dissertation, *"Computer Aided Deformation Analysis of Deep Drawing"*, Middle East Technical University, Ankara, Turkey

Doege, E., 1992 and Hesberg, U., *"Eigenschaften und Umformverhalten oberflachenveredelten Feinbleches beim Tiefziehen"* Blech Rohre Profile 39, pp. 25-30

Hibbit, Karlson and Sorenson, Inc., *"ABAQUS: User's, Examples and Theory manuals, version 4.6"*

Lee, J.K., 1990, Wagoner, R.H. and Nakamichi, E., *"A Benchmark Test for Sheet Metal Forming Analysis"*, Report No. ERC/NSM-90-22-2, Ohio State University, Columbus, OH

Oh, S.I., 1991, Wu, W.T., Tang, J.P., and Vedhanayagam, A., *"Capabilities and applications of FEM code DEFORM: the perspective of the developer"*, Journal of Materials Processing Technology, Elseviers Science Publishers B.V., pp.25-41

Ohwue, T, 1991 and Nakamichi, E., *"Finite element analysis of box shaped cup drawing and comparison with experiments"*, VDI berichte 894, "FE-simulation of 3-D Sheet Metal Forming processes in automotive industry", VDI Verlag, pp.153-166

Ramaekers, J.A.H., 1988, Houtackers, L.J.A., and Peeters, P.B.G., *"Plastisch bewerken van metalen, Procesbeheersing in de onderdelenfabricage"*, ISBN 90-6808-007-5, Uitgave Omtec stichting, Mierlo

Stoughton, T.B., 1985, *"Finite Element Modelling of 1008 AK steel Stretched over A Rectangular Punch with Bending Effects"*, Research Report No.-Ph.-1228, General Motors Research Laboratorium

Wang, C.T. ,1992, Kinzel, G.L., and Altan, T., *"Plane Strain Sheet Bending -Part 2-Advanced Topics, Chapter VI"*, Report No. ERC/NSM-S-47-92, Ohio State University, Columbus, OH

APPENDIX 2 PROCESS DESCRIPTION OF THE FLANGE

Fig. 1 shows the flange of a cup with the stresses acting on it. When deep drawing the flange is drawn in from the initial blank radius u_0 to u. Due to the compressive stresses, the flange thickens from t_0 to t. As a simplification it is assumed that the thickness remains constant.

$$t \neq t(r) \tag{1}$$

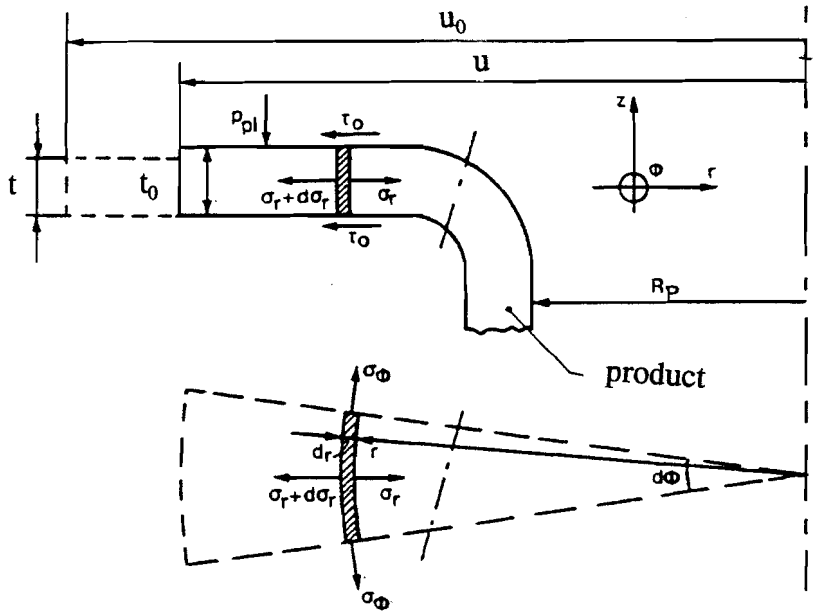

Fig. 1 Equilibrium at the flange in deep drawing with blank holder, [Ramaekers, 1988]

Considering axisymmetric deep drawing, gives the following relations.

$$\sigma \neq \sigma(\phi) \tag{2}$$

$$\tau \neq \tau(\phi) \tag{3}$$

The blank holder pressure is very small, compared to the yield stress of the material, thus it is assumed that:

$$\sigma_z = 0 \tag{4}$$

Furthermore at the outer edge of the flange, unidirectional stress is assumed.

$$\sigma_{r\,(r=u)} = 0 \tag{5}$$

The process modelling is finished by Eqations 1 to 5. The material behavior is assumed to be ideal plastic, thus σ_f = constant = C. In order to describe the friction, the Coulomb friction model is used, as in Equation 6.

$$\tau_f = \mu\, p_{BH} \tag{6}$$

Equilibrium in Fig. 1 results in:

$$+(\sigma_r + d\sigma_r)(r + dr)d\phi t - \sigma_r\, rd\phi t - 2\sigma_\phi \frac{d\phi}{2} + 2\tau_0 rd\phi dr = 0 \tag{7}$$

This can be simplified as:

$$d\sigma_r + (\sigma_r - \sigma_\phi)\frac{dr}{r} + 2\tau_0 \frac{dr}{t} = 0 \tag{8}$$

In order to solve the differential Equation 8, σ_ϕ has to be expressed in σ_r. The most simple solution is to use the Tresca yield criteria, as in Equation 9. Substitution of Equation 9 into Equation 8 results in Equation 10.

$$\sigma_r - \sigma_\phi = \sigma_{max} - \sigma_{min} = 1.1\ \sigma_f \tag{9}$$

$$\int_{\sigma_r(r=r)}^{\sigma_r(r=u)} d\sigma_r = \int_{\sigma_r}^{0} d\sigma_r = -1.1\sigma_f \int_{r=r}^{r=u} - 2\tau_0 \int_{r=r}^{r=u} \frac{dr}{t} \tag{10}$$

After integration Equation 10 is written as:

$$\sigma_r = 1.1\sigma_f \ln\frac{u}{r} + 2\tau_0 \frac{u-r}{t} \tag{11}$$

The total force is calculated using equation 11:

$$F_{flange} = 2\pi R_p t \sigma_r(r=R_p) \tag{12}$$

For ideal plastic material behavior (σ_f is constant and equal to C) the force is written as:

$$F^*_{flange} = \frac{t}{t_0}[1.1\ \ln\frac{u}{R_p} + 2\mu p_{BH}\frac{u-R_p}{t}] \tag{13}$$

Where:

$$F^*_{flange} = \frac{F_{flange}}{2\pi R_p t_0 C} \tag{14}$$

At the edge of the flange, $\sigma_{r(r=u)} = 0$.

Using Levy-Von Mises relations results in the following expression:

$$\epsilon_{r\,(r=u)} = \epsilon_{z\,(r=u)} = -\frac{1}{2}\epsilon_{\phi\,(r=u)} \tag{15}$$

Thus, according to the strain definition:

$$\ln\frac{t}{t_0} = -\frac{1}{2}\ln\frac{u}{u_0},\ thus\ t = t_0\sqrt{\frac{u_0}{u}} \tag{16}$$

Then, substituting Equation 16 into Equation 13 results in:

$$F^*_{flange} = \sqrt{\frac{u_0}{u}}\{1.1\ \ln\frac{u}{R_p} + 2\mu\ p_{BH}\frac{R_p}{t_0}\{\frac{u}{R_p} - 1\}\sqrt{\frac{u}{u_0}}\} \tag{17}$$

The initial drawing ratio and the drawing ratio are defined as:

$$\beta_0 = \frac{u_0}{R_p} \quad ; \quad \beta = \frac{u}{R_p} \tag{18}$$

Substituting these ratios into Equation 17 gives the following expression for the force in the flange.

$$F^*_{flange} = 1.1\sqrt{\frac{\beta_0}{\beta}}\ln\beta + 2\mu\ p_{BH}\frac{R_p}{t_o}(\beta - 1) \tag{19}$$

From this equation, it is clear that both the friction coefficient, blank holder pressure and the relative product size influence the power. An increasing relative product size, coefficient of friction, or blank holder pressure increases the required power to draw the cup.

APPENDIX 3 FEM SIMULATIONS USING ABAQUS

By performing experiments and simulations the combined influence of the relative product size and friction on the deep drawing process is investigated. The FEM code ABAQUS is used to simulate several combinations of relative product sizes and blank holder forces. The simulations are compared with experimental results to investigate whether both the experiments and FEM results show the same trend.

The blank is defined by 240 elements, three layers in thickness direction. The main reason to defince several layers in thickness direction is to add more bending stiffness to the blank. The used element type is CAX4R. This elements has four nodes with a billinear displacementsfield. For additional information is referred to the users manual by Hibbit, Karlson and Sorenson. When simulating the same process with increasing initial sheet thicknesses, the height of the elements increases accordingly.

The friction coefficient in the blank and die surface is set to be $\mu = 0.08$. At the punch blank surface, μ is defined as 0.15. These values are relatively high, and probably higher than the friction coefficient in the experiments. Thus fracture will occur at a lower BHF compared with the experiments. As an additional investigation, it is recommended to simulate the process with a decreased friction coefficient in both the die, blank holder and punch surface. Then the agreement with the experiments will probably improve. The elastic-plastic material behavior is defined by a piecewise linear approximation.

ERC/NSM-S-93-15

FEM simulations of the deep drawing process

H.P.M. van de Koolwijk

Appendix 1

June 1993

VF code D3 WPA 1518

NSF Engineering Research Center for
Net Shape Manufacturing
The Ohio State University
1971 Neil Avenue
Columbus, Ohio 43210-1271

Afstudeerhoogleraar: prof. ir. J.A.G. Kals

Begeleiders: prof. dr. T. Altan
ir. R.J.J.M. Sniekers

FOREWORD

This document has been prepared for the Engineering Research Center for Net Shape Manufacturing. The main topics are:

(a) FEM simulations of the deep drawing process using FEM code DEFORM
(b) Investigations regarding influence of tool geometry on bending effects and comparison of membrane vs. solid FEM codes
(c) Investigation of blank holder force (BHF) effects in 3-D FEM simulation of square cups

ERC/NSM was established on May 1, 1986 and is funded by the National Science Foundation and the member companies. The focus of the center is net shape manufacturing with emphasis on cost-effective manufacturing of discrete parts. The research is concentrated on manufacturing from engineering materials to finish or near finish dimensions via processes that use dies or molds. In addition to conducting industrially relevant engineering research, the Center has the objectives to:

a) establish close cooperation between industry and faculty
b) train students, and
c) transfer the research results to interested companies

Information about the ERC for Net Shape Manufacturing can be obtained from the office of the Director, Professor Taylan Altan, located at 339 Baker Systems Engineering Building, 1971 Neil Avenue, Columbus, Ohio 43210-1271

EXECUTIVE SUMMARY

FEM codes are used to simulate sheet metal forming processes in order to predict the influence of process parameters on strain distributions. The FEM code DEFORM is developed to simulate billet forming processes. In this report the use of DEFORM in deep drawing is investigated. Several simulations are performed using DEFORM and compared with the results of the other FEM codes and experimental data.

Bending effects are investigated by performing both axisymmetric and plane-strain simulations in which the ratio of die corner radius, r_d, over thickness, t, (r_d/t) is varied. The influence of the r_d/t ratio on the radial and thickness strain distributions is analyzed. The results such as local bending strain, shift of the neutral axis, and global bending effects are compared with the (plane-strain) theory whenever possible. Several layers of elements in the thickness direction are used in the DEFORM simulations in order to determine the variation of the strains in the thickness direction. Mid layer strains calculated using DEFORM are compared to the membrane strains calculated obtained from SHEET_FORM. Although SHEET_FORM has a membrane formulation it performs a local bending correction on the membrane strains to estimate the inner and outer surface strains at the locations of tool curvatures. The accuracy of the local bending corrections in the SHEET_FORM results is checked by comparing with the DEFORM results.

Three dimensional FEM simulations in deep drawing a square cup are performed. A comparison with experiment is made and the influence of BHF (blank holder force) on deformation is investigated. The main objective of these simulations is to predict the variation of thickness strain as the BHF changes and to evaluate the advantages of using the 3-D FEM code SHEETFORM-3D.

TABLE OF CONTENTS

LIST OF FIGURES

LIST OF TABLES

LIST OF SYMBOLS

t	Sheet thickness	[mm]
t_0	Initial thickness	[mm]
R_p	Punch radius	[mm]
r_p	Punch corner radius	[mm]
R_d	Die opening radius	[mm]
r_d	Die corner radius or die profile radius	[mm]
R	Blank radius	[mm]
Rm	Radius of middle axis	[mm]
R_n	Radius of neutral axis	[mm]
d	Shift distance of neutral axis	[mm]
R_i	Inner radius of bent sheet	[mm]
R_o	Outer radius of bent sheet	[mm]
d_{fo}	Fictious diameter of square punch	[mm]
A_0	Initial surface area of blank	[mm^2]
A	Surface area of punch	[mm^2]
v_y	Punch velocity	[m/s]
K_t	Tangent stiffness matrix	[N/mm]
F	Applied force vector	[N]
I	Incremental force vector	[N]
Δu	Incremental displacement	[m]
u	Displacement	[m]
$\dot{u}$	Velocity	[m/s]
$\ddot{u}$	Acceleration	[m/s^2]
t	Time	[s]
M	Mass matrix	[kg]
v	Velocity vector	[m/sec]
v_s	Sliding velocity in tangential direction	[m/sec]
t	Traction vector	[N]
t_s	Traction (due to friction)	[N]
n	Unit normal to contact surface	[-]
K_i	Penalty constant to penalize penetration	[-]
V	Volume of workpiece	[mm^3]
S	Surface of workpiece	[mm^2]
w	Width	[mm]
$\bar{\varepsilon}$	Effective strain	[-]
ε_{memb}	Membrane strain	[-]

$\dot{\bar{\varepsilon}}$	Effective strain-rate	[1/sec]
$\bar{\varepsilon}_0$	Effective pre-strain	[-]
ε_0	Yield strain	[-]
ε_{outer}	Outer surface radial strain	[-]
ε_{inner}	Inner surface radial strain	[-]
ε_{mid}	Middle axis radial strain	[-]
$\bar{\varepsilon}_{outer}$	Outer surface effective strain	[-]
$\bar{\varepsilon}_{inner}$	Inner surface effective strain	[-]
$\bar{\varepsilon}_{mid}$	Middle axis effective strain	[-]
$\bar{\sigma}$	Effective stress	[N/mm^2]
σ_N	Normal stress	[N/mm^2]
σ_Y	Yield stress	[N/mm^2]
σ_b	Flow stress	[N/mm^2]
σ_{ij}	Stress component	[N/mm^2]
τ_f	Friction stress	[N/mm^2]
δ_{ij}	Kronecker delta	[-]
σ_m	Tensile strength	[N/mm^2]
K	Reference stress value	[N/mm^2]
n	Strain hardening exponent	[-]
m	Strain rate sensitivity exponent	[-]
E	Young's modulus	[N/mm^2]
υ	Poisson's ratio	[-]
R	Normal anisotropy factor	[-]
r_{max}	Maximum anisotropy	[-]
r_{min}	Minimum anisotropy	[-]
r_m	Average of anisotropy ($0.5*(r_{max} + r_{min})$)	[-]
M	Exponent in Hill's yield function	[-]
ξ_i	Weight factor	[-]
BHF	Blank holder force	[N, kN]
s	Punch stroke	[mm]
l_e	Distance after deformation	[mm]
l_0	Initial distance	[mm]
F_p	Punch load	[N, kN]
β	Drawing ratio	[-]
DBF	Draw bead force	[n, kN]
ϕ	Bending angle, wrapping angle	[rad]
μ	Coulomb friction coefficient	[-]
m	Tresca friction coefficient	[-]

F	Friction force	[N]
T	Tensile force	[N]
M	Bending moment	[Nm]
T_s	Tensile force after sliding and unbending	[N]
T_b	Tensile force before sliding and unbending	[N]
M_s	Bending moment after sliding and unbending	[Nm]
M_b	Bending moment before sliding and unbending	[Nm]

CHAPTER 1

INTRODUCTION

Sheet metal forming is widely used in the industry, for production of automobiles, office furniture, construction supplies etc. These products are usually produced in large quantities, because of the high tooling costs and the high investments in machines such as presses. The main reasons for the high tooling costs are a) high machining costs to manufacture the die and punch and b) many trial-and-errors steps required to design the dies. A die design method which reduces the number of trial-and-error steps results in considerable amount of time and money savings.

In order to reduce the trial and error steps, it is necessary to analyze the deformation process during the design stage and predict stresses, strains and possible failure (fracture and wrinkling) in order to achieve a better control of the process parameters.

Finite Element (FEM) and Finite Difference (FDM) based codes are usually used to obtain information on important parameters, such as strain distributions, wall-thickness variations and load-stroke diagram. Main objective is to predict and optimize the behavior of the sheet in the die by performing FEM simulations. The tool geometry and the process parameters are optimized by varying the blank geometry, material parameters, and blank holder force (BHF).

There is a large number of FEM codes developed in the last decade. One of them is DEFORM which is originally developed for simulating billet forming processes such as forging, extrusion etc. With its automatic mesh generator and user-friendly preprocessing, it is relatively easy to use. In this report, the applicability of DEFORM in sheet metal forming is investigated by performing simulations and comparing the results with other codes and experimental data.

FEM codes can be divided into two categories, a) membrane formulation which neglects bending effects, and b) solid and shell formulation which includes bending effects. DEFORM includes bending effects, since it uses solid elements. The advantage of the membrane code is the computational efficiency and its simplicity. However, for certain geometries, it is not correct to use this formulation, since the bending effects can not be neglected anymore. As the die corner radius over sheet thickness radio (r_d /t) decreases, bending effects increase very fast. Thus, one should use a solid or shell approach.

In order to investigate the influence of r_d /t ratio on the radial and thickness strain distributions, three axisymmetric simulations with r_d/t ratios of 18, 9 and 5 and two plane-strain simulations with ratios of 9 and 5 are performed. By including local bending correction in the membrane codes such as SHEET_FORM, the results improve. This improvement is investigated by comparing the results from DEFORM simulations with SHEET_FORM (with and without local bending correction).

If the theory provides a good estimation of the bending effects, then, the membrane codes can be equipped with a bending correction module. This combines the computational efficiency of the membrane codes as well as the accuracy of the solid codes.

The BHF affects the drawability of a cup significantly. Since the tendency to wrinkling and fracture occur at a different punch stroke, it is possible to increase the drawing ratio by varying the BHF as a function of the stroke. Previous investigations on BHF variations by Ahmetoglu, [1992] in deep drawing of round cups confirm this. The influence of BHF in deep drawing of square cups is investigated using a 3D FEM code called SHEETFORM-3D. The deformation state in a square cup is not uniform for all the cross-sections. Therefore it may be necessary to have different BHF variations in different regions of the square cup.

In Chapter II, literature about FEM simulations in deep drawing is reviewed, and several important aspects of the process such as wrinkling, necking and the FEM codes are described to provide a background.

In Chapter III, DEFORM simulations are performed to compare with other FEM codes and with experimental data. The processes that are simulated with DEFORM are:

- Axisymmetric Deep Drawing with hemispherical and cylindrical punches (comparison with other codes and experiment)
- Plane-strain Stretch Forming with hemispherical punch (comparison with other codes)
- Plane-strain Deep Drawing (Chapter IV)

The bending effects using both DEFORM and SHEET_FORM are investigated in Chapter IV. Axisymmetric as well as plane-strain deep drawing is simulated with several die corner radii. As the die corner radius decreases, the agreement of SHEET_FORM predictions with that of DEFORM gets worse, as expected. The improvement of the SHEET_FORM results when bending correction is added is also investigated.

In Chapter V the influence of the BHF is investigated by performing 3D FEM simulations of the drawing of a square cup. The results such as thickness strain distributions, draw-in, and load-stroke diagram are presented.

Chapter VI summarizes the concluding remarks and gives recommendations for future work.

CHAPTER II

SIMULATION OF DEEP DRAWING USING THE FINITE ELEMENT METHOD

2.1 Introduction

During the last decade, the numerical simulation of the deep drawing operation using FEM was extensively studied. To speed up the process from die design to mass production, it is desirable to obtain information regarding strain distribution, occurrence of wrinkles, draw-in at the edges and springback. With the use of presently available FEM codes, not all of this desired information is obtainable through the numerical simulation of the deep drawing operation.

There are several design parameters which can be varied, to observe their influences on the process. The most important parameters are blank holder pressure, design of draw beads, tool geometry, friction and properties of the formed material. An extended review of the finite element analysis of sheet metal forming processes was done by Choudry and Lee, [1990]. The goals of this chapter are to describe the different types of numerical methods and codes, to summarize the results of previous deep drawing simulations, and to make comparisons with experiments.

For the numerical simulation of an axisymmetric deep drawing process, two major methods may be used: (1) the Finite Difference Method (FDM), and (2) the Finite Element Method (FEM). The application of FDM is only possible for simple geometries such as an axisymmetric or plane-strain deep drawing or stretch forming operation. An example of an FDM code is SHEET_FORM, [Sitamaran, 1989]. In an FDM analysis, the stresses during the forming process are calculated by numerical integration and iteration, making several assumptions to reduce the complexity of the problem, [Lange, 1990]. The most

important assumptions are related to the equilibrium equations, volume conservation, and material properties.

2.2 Elastic-plastic and rigid-plastic formulations

Some FEM codes assume the material behavior to be elastic-plastic, others rigid plastic. In Fig. 2.1, the strain hardening curves for both elastic-plastic and rigid-plastic are shown, [Besdo, 1991]. With an assumption of elastic-plastic material behavior, one can simulate the forming process to predict the springback and residual stresses. On the other hand, the computation time increases. For stretch forming operations, springback has a minor influence on the final geometry of the workpiece, compared to deep drawing because more material is deformed plastically. In deep drawing, the flange moves, and the cup radius increases due to springback as shown in Fig. 2.2. The amount of springback depends on several material and geometrical parameters. The most important parameters affecting springback are die corner radius (r_d) and sheet thickness (t), i.e., the r_d/t ratio.

The formulation which is based on rigid-plastic assumption was developed by Kobayashi et al., [1977]. In this case, the elastic effects are neglected because of the large plastic strains. The step sizes used during the numerical iteration can be larger by neglecting the elastic behavior. The CPU (Central Processing Unit) time, thus, decreases compared with the elastic-plastic formulation. The disadvantage of this method is that springback can not be predicted.

According to Redekop and Nguyen, [1986] FEM methods have the capability to handle complex problems. There are two different formulations describing variations of stresses and strains, [Finckenstein, 1987]. The total Lagrangian formulation chooses the reference state to be the initial undeformed shape. The other formulation is the updated Lagrangian formulation, which considers the current configuration as the reference state. In the FEM method, the deformation of any continuous body can be simulated by dividing it into a finite number of elements. These elements must be connected at a series of nodes. There are three approaches that can be used for the simulation:

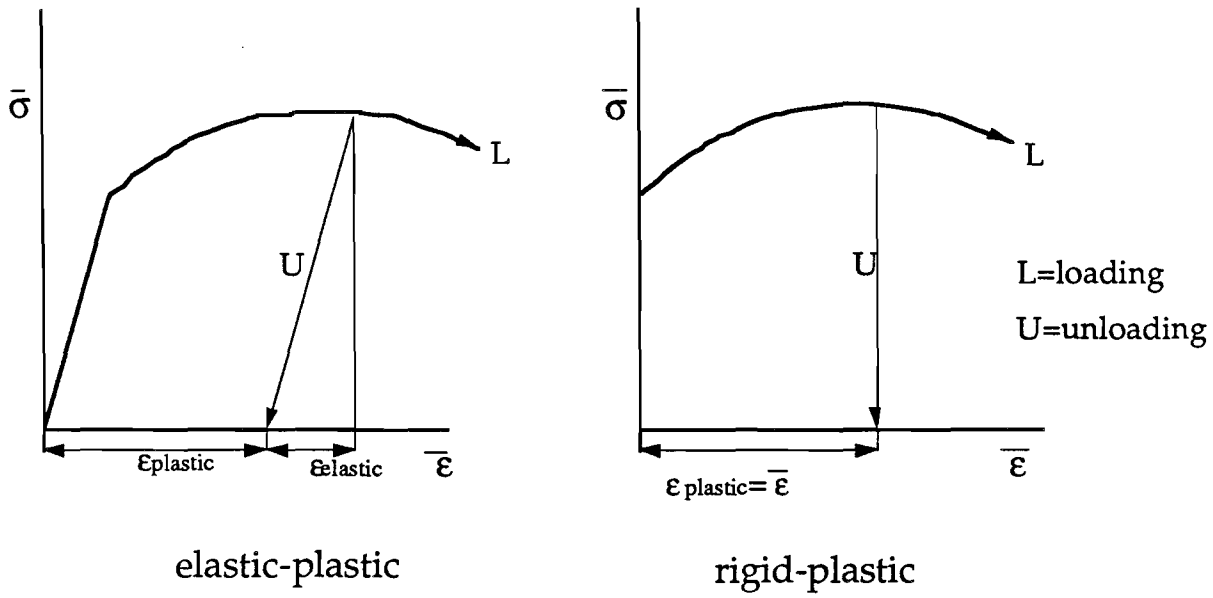

Fig. 2.1 Strain hardening curves for elastic-plastic and rigid-plastic behavior, [Bosde, 1991]

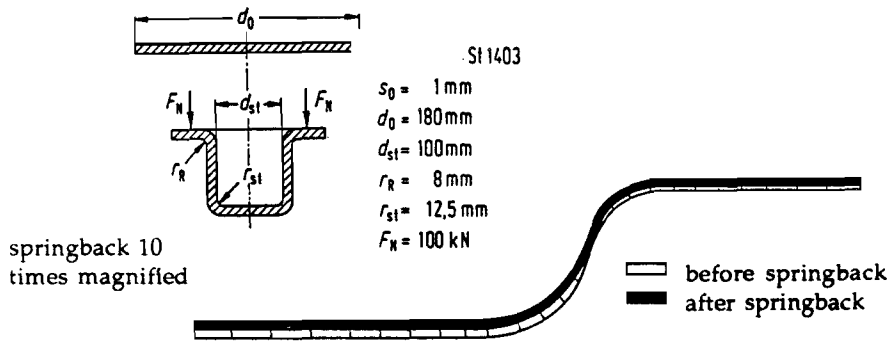

Fig. 2.2 Springback after deep drawing, material St1403, [Lange, 1990]

-1 membrane theory (no bending effects)
-2 solid approach
-3 shell theory

The complexity in simulating the deep drawing problem is caused by the geometrical and material non-linearities, and the friction that occurs during the process at the blank-tool interface. The three main problems encountered in FEM simulation of the deep drawing operation are:

-1 description of tool geometry
-2 contact and friction conditions
-3 effective finite element formulations to use with two sided contact (the flange portion of the part contacts the punch as well as the blank holder). Sometimes two sided contact problems can be solved by remeshing the elements in the flange after the blank holder is removed (as the draw continues to obtain a cup without a flange).

2.3 Implicit and explicit FEM methods:

FEM techniques can be divided into implicit and explicit time integration methods. Nagtegaal and Taylor [1992] made comparisons of these two methods in the analysis of sheet forming problems. Important characteristics are shown in Table 2.1.

Table 2.1 Differences between explicit and implicit codes, using two examples

Explicit (Dyna3D)	Implicit (ABAQUS)
- Only time impact problems	-Both static and dynamic analysis
- Only dynamic analysis	-Sensitive for convergence problems
- Faster (sometimes)	-For simple problems
- More robust and efficient	-Needs careful specification of boundary conditions

2.3.1 Implicit solution procedure

The implicit solution procedure uses an incrementation strategy based on the success rate of a full Newton iterative solution method. The Newton scheme that is used to solve the incremental equations has the standard form as in Equation (2.1):

$$\Delta u^{(i+1)} = \Delta u^{(i)} + K_t^{-1}.(F^{(i)} - I^{(i)}) \qquad (2.1)$$

Where: K_t = current tangent stiffness matrix
F = applied load vector
I = internal load vector
Δu = incremental displacement

The history dependent behavior is obtained on the basis of the incremental displacements Δu and the state at the start of the increment. Various criteria are used to make sure that the solution converges. The most important requirement is that the residuals should be sufficiently small, (the maximum value of $F^{(i)} - I^{(i)}$ must be smaller than a specified tolerance parameter ε times an average force measure obtained from F and I). The contact condition must be completely stabilized. If a contact condition changes from closed to open, another iteration will be made. Depending on convergence speed, the next increment is chosen smaller or larger. When the changes in contact are infrequent the implicit analysis procedure can proceed very effectively.

2.3.2 Explicit solution procedure

The explicit procedure uses an explicit integration rule along with the use of diagonal element mass matrices. The equations of motion for the body are integrated using an explicit central difference integration rule according to expressions (2.2) and (2.3).

$$u^{(i+1)} = u^{(i)} + \Delta t^{(i+1)}.\dot{u}^{(i+1/2)} \qquad (2.2)$$

$$\dot{u}^{(i+1/2)} = \dot{u}^{(i-1/2)} + \left(\frac{\Delta t^{(i+1)} + \Delta t^{(i)}}{2}\right)\ddot{u}^{(i)} \qquad (2.3)$$

Where:

u	= displacement	[m]
$\dot{u}$	= velocity	[m/s]
$\ddot{u}$	= acceleration	[m/s^2]
t	= time	[s]

The central difference integration operator is explicit in that the kinematic state may be advanced, using known values of $\dot{u}^{(i-1/2)}$ and $\ddot{u}^{(i)}$ and from the previous increment. The accelerations at the beginning of the increment are computed by:

$$\ddot{u}^{(i)} = M^{-1}.(F^{(i)} - I^{(i)}) \tag{2.4}$$

Where:

M	= mass matrix
F	= applied load vector
I	= internal force vector
$\ddot{u}$	= acceleration at time step i

The explicit integration procedure does not require any iterations and tangent stiffness matrix. To compare the numerical results, ABAQUS implicit and explicit modules were used by Nagtegaal and Taylor, [1992]. In ABAQUS, contact between elements and the rigid surface is considered by 'interface' elements. Honecker, [1989] used DYNA3D which is another FEM code based on explicit time integration and especially intended for impact problems. DYNA3D is originally developed for impact problems, i.e., to simulate short time events (of the order of milliseconds). Thus, in using DYNA3D, the punch speed should be very high to obtain these short process times. Honecker, [1989] compared DYNA3D (explicit) with ABAQUS (implicit).

Implicit codes, such as ABAQUS and DEFORM, can simulate both static and dynamic problems, while explicit codes only can be used in dynamic simulations. The disadvantage of implicit codes is their sensitivity to convergence problems in the solution of non-linear equations and the problems that occur if the contact condition is not stabilized.

2.3.3 Deep drawing using a flat bottomed cylindrical punch

Deep drawing of an axisymmetric cup was simulated by Nagtegaal and Taylor, [1992] using both implicit and explicit solution procedures. There are 744 finite strain shell elements used in the simulation. Table 2.2 and Fig. 2.3 show the geometry and tool parameters used in this simulation. The objective of the study was to investigate springback and the possibility of wrinkling. Therefore it was very essential to model the bending behavior properly, because wrinkling is considered as bending with a very small bending radius.

In the implicit formulation the simultaneous contact between two rigid surfaces and the shell elements is not allowed since this will make the Lagrange multipliers undetermined. To solve this problem, the blank holder surface was softened with a stiffness equal to that of the blank but in reverse direction. The punch nose was slightly rounded to prevent (a) occurrence of undetermined contact between punch and blank and (b) prevent the separation of nodes.

Table 2.2 Tool geometry and process parameters used by Nagtegaal and Taylor, [1992], symbols as in Figure 2.3, using aluminum killed steel

Ludwik-Hollomon hardening $\bar{\sigma} = K(\bar{\varepsilon} + \bar{\varepsilon}_0)^n$			
Strength coefficient K	=	513	MPa
Strain hardening exponent n	=	0.223	[-]
Punch radius (R_p)	=	50	m m
Punch corner radius (r_p)	=	13	m m
Die radius (R_d)	=	51.25	m m
Die corner radius (r_d)	=	5.0	m m
Blank radius (R)	=	100	m m
Blank thickness (t)	=	0.82	m m
Blank holder force	=	100	kN
Friction coefficient μ (die and sheet)	=	0.15	[-]
Friction coefficient μ (punch and sheet)	=	0.125	[-]
Stroke	=	60.0	m m

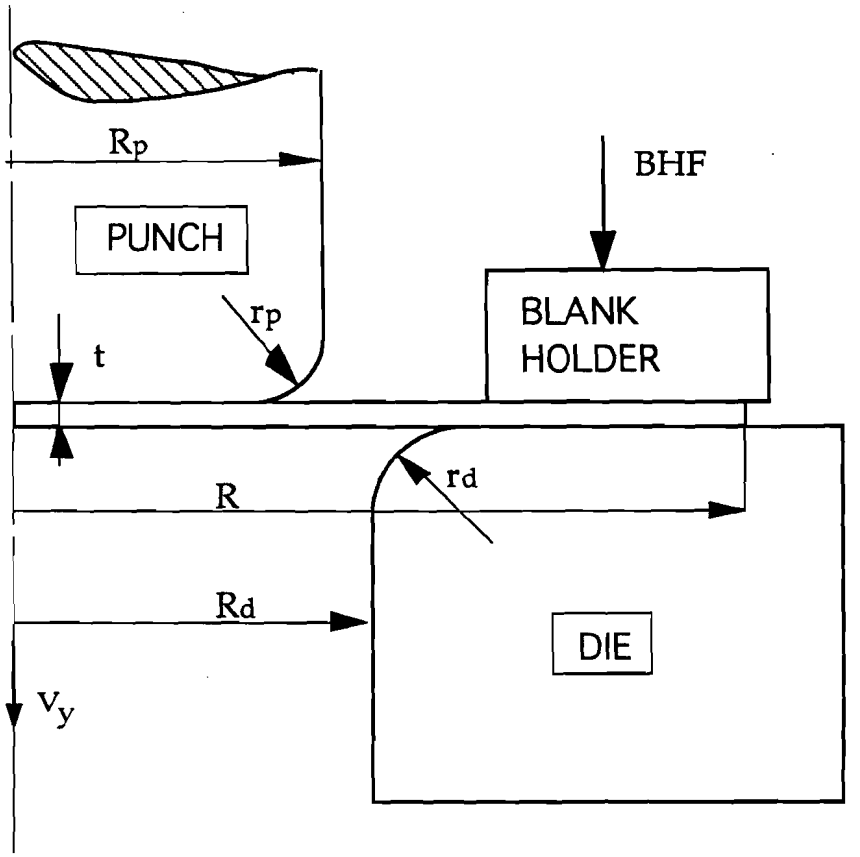

Fig. 2.3 Geometry of deep drawing process and definitions of the symbols

The blank holder force was 25 kN for the simulated quarter of the model. In the explicit analysis, discontinuities along the edge of the punch caused concentric bending "waves" when the sheet slides over the punch, which results in oscillatory bending strains in the center of the sheet. A pressure of 0.5 MPa was applied to the blank under the flat part of the punch. This prevented the propagation of the waves to the center and damped out the bending waves. For relatively lower punch speeds (to 30 m/sec), implicit and explicit formulations generate about the same results. As the punch speed increases (up to 100 m/sec), the overall solution is more influenced by the waves. Very high and unrealistic punch speeds (in practical drawing operations the ram speed is in the range of 250 mm/sec to 10 mm/sec) were chosen because the explicit analysis can only handle impact type problems with very small deformation times.

In this example, the implicit analysis provides more realistic results. The CPU time varies from some minutes up to 36 hours (low punch speed). The explicit analysis is faster than the implicit analysis. For simple problems, the implicit method provides accurate results, and it can even be faster than the explicit method (at low punch speed). However, the boundary and contact conditions should be very carefully specified in the implicit method, [Nagtegaal and Taylor, 1992].

2.3.4 Deep drawing using a hemispherical punch

Honecker, [1989] compared implicit ABAQUS and explicit DYNA3D methods by simulating the deep drawing with a hemispherical punch. The geometry and process parameters are shown in Table 2.3 using the symbols as defined in Fig. 2.3.

A quarter of the blank was defined by 400 shell elements in the DYNA3D simulation while in ABAQUS only 24 shell elements were used. The punch velocity was prescribed to follow a sine curve with zero velocity at punch depths s = 0 and s = 60 mm (maximum stroke). The process time was 10^{-3} sec, thus the average punch speed was about 60 m/sec which is extremely high when compared with practical average punch speeds of 50 to 250 mm/sec.

The load-stroke diagram, given in Fig. 2.4a, is smoother in the case of ABAQUS because simulating deep drawing is a dynamic analysis and this kind of problems can be better solved by an implicit solution procedure.

Table 2.3 Tool geometry and process parameters used by Honecker [1989], symbols as in Figure 2.3

Effective stress - effective strain relation $\bar{\sigma} = K(\bar{\varepsilon} + \bar{\varepsilon}_0)^n$			
Strength coefficient K	=	598	MPa
Strain hardening exponent n	=	0.216	[-]
Punch radius (R_p) (hemispherical)	=	50	m m
Punch corner radius (r_p) (hemispherical)	=	50	m m
Die radius (R_d)	=	52.83	m m
Die corner radius (r_d)	=	6.35	m m
Blank radius (R)	=	80	m m
Blank thickness (t)	=	1.00	m m
Blank holder pressure	=	1.0	N/mm^2
Friction coefficient μ	=	0.15	[-]
Stroke	=	60.0	m m

Increasing process time, or increasing the blank holder force, or filtering the resulting data (usually done in dynamic analysis) will make the curve smoother for the DYNA3D case. The strain distributions as predicted by both the codes are reasonable close as shown in Fig. 2.4b. Friction is described by specifying (a) a Coulomb friction coefficient and (b) sticking conditions. Sticking is a contact interface condition which limits the maximum allowable shear stress at the interface. It is equal to the shear stress when plastic deformation starts, [Honecker et al., 1989]. For a very high normal pressure the shear stress generated by the friction reaches the yield shear strength. Then the material will shear off inside the body of the workpiece instead of sliding over the tool surface because this path requires less energy. The sticking condition is defined by an elastic stiffness that limits the elastic deflection of the elements. The convergence in ABAQUS is very sensitive to the value of the "stiffness in sticking".

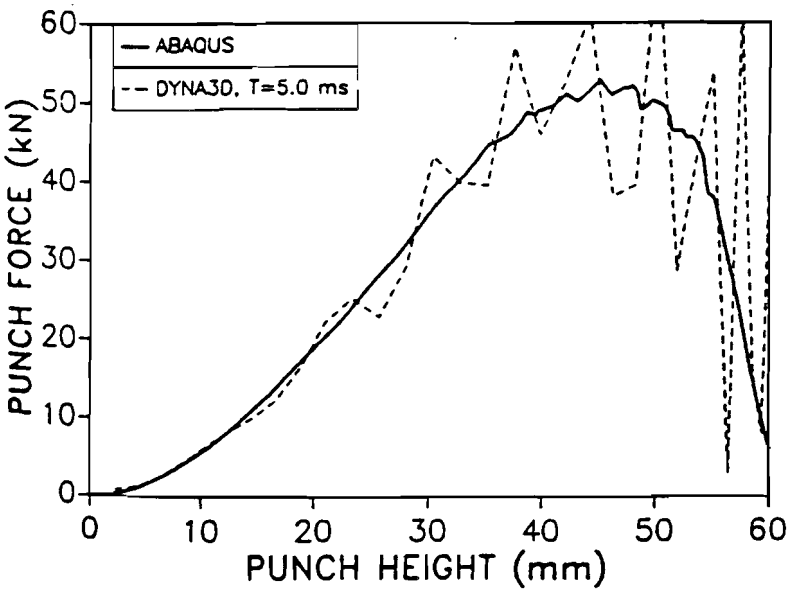

Fig. 2.4a Punch force versus punch displacement, [Honecker et al., 1989]

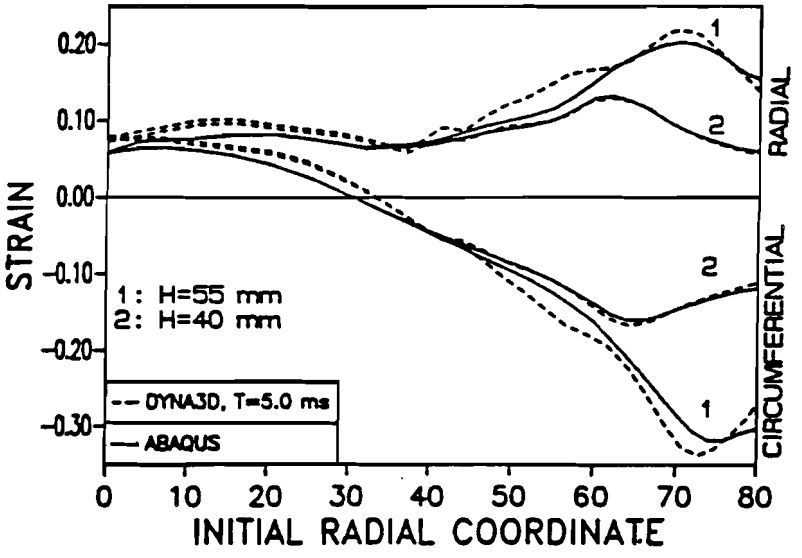

Fig. 2.4b Radial and circumferential strain distributions at punch displacements of 40 and 55 mm, [Honecker et al., 1989]

Honeckers' conclusions are that (a) DYNA3D analyses can provide acceptable results for process times in the range of one to five milliseconds, and (b) implicit codes are less robust and efficient (for complex process geometries). For large scale 3D-problems explicit codes are primarily applicable, while implicit codes should be used in parametric studies and simple forming operations where maximum accuracy is desired. CPU times are 1.68 CPU-hours on a CYBER 910-500 workstation for the DYNA3D case and 2.38 CPU-minutes on an IBM 3090 for the ABAQUS case.

2.4 Prediction of defects using FEM

In deep drawing, defects such as wrinkles or necking can occur. Levaillant and Chenot, [1992] divided these defects in two categories: (a) wrinkles which are mechanics (i.e. state of stress and strain) dependent and (b) necking and fracture which are material dependent.

2.4.1 Wrinkles

Wrinkling is caused by excessive in-plane compression stresses which occur in the flange as soon as the draw-in starts. There are two types of wrinkles. First order wrinkles occur under the blank holder and the second order wrinkles occur at the unsupported region of the deforming sheet. The exact time of occurrence of the wrinkles is not well defined. There are two cases: (a) wrinkles that are squeezed indicating deformation by contact of the sheet with die and blank holder and (b) wrinkles which seem to have developed without any restriction indicating that wrinkling occurred in the springback stage after the blank holder is removed. In order to prevent first order wrinkles, a blank holder is used. There is a certain amount of friction between the blank holder and the sheet metal blank. The friction force causes a radial tensile stress in the flange. During the deep drawing, this tensile stress must be well controlled. If it is too high, fracture can occur near the punch corner radius but if it is too low, wrinkles can occur. Friction is not the only factor affecting the occurrence of wrinkles. Tool geometry (especially the clearance between die and punch), BHF, blank diameter and material properties also play an important role.

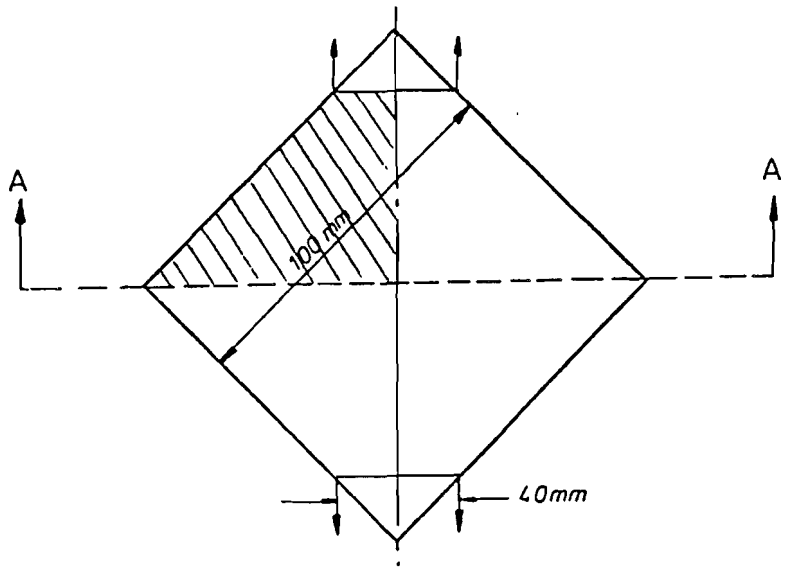

Yoshida Buckling Test Specimen

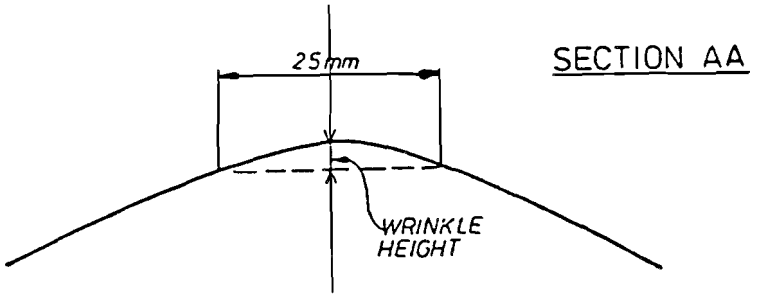

Measurement of Wrinkle Height

Fig. 2.5 Yoshida buckling test specimen stretched perpendicular to the section A-A, and measurement of the wrinkle height, [Ni et al., 1990]

Increasing sheet thickness or work hardening can reduce or prevent wrinkling. If there are wrinkles under the blank holder, it is because the blank holder force (BHF) is too low or the blank diameter is too large.

Wrinkles can be compared with a plastic buckling process in which the wavelength of the buckles is very short. The experimental Yoshida buckling test (Fig. 2.5) involves no friction, and the single buckle geometry can easily be monitored continuously. In the deep drawing operation, there is friction between the die and the metal sheet and between the blank holder and the metal sheet, [Levaillant et al., 1992].

In the Yoshida buckling test, a thin square plate is non-uniformly stretched in its diagonal line. This causes wrinkles, and it is reported that the wrinkling behavior of real forming processes may be analyzed by the experimental results from the Yoshida test. Wrinkling and buckling are due to an in-plane compressive stress. There is no simple approach to predict buckling. Batoz et al., [1989] presented a formulation that has the possibility to analyze pre and post wrinkling behavior. The Yoshida buckling test has been simulated and the numerical results are in good agreement with previous experiments.

There are two approaches to simulate the buckling problem. The first is the equilibrium method, [Ni et al., 1990] which is concerned with the equilibrium configuration of the perfect system. It is based on the observation that the transition from stability to instability may be marked by the appearance of an additional equilibrium configuration in the vicinity of the one for the perfect system. The additional equilibrium positions may be determined by solving the eigenvalue problem of the system, [Ni et al., 1990]. The second one is known as the imperfection method and applies the equilibrium method to predict the wrinkle height of a metal sheet for in-plane loading conditions. This method tries to predict the value of the load for which the displacements become excessive, or even infinite. This approach is based on the observation that small eccentricities in a loading condition, or small imperfections in flat geometries can never be avoided in reality. The finite element model includes the presence of these imperfections and the obtained solution can be used to determine if for a certain value of the load, the equilibrium configuration becomes different from the one of the unloaded system.

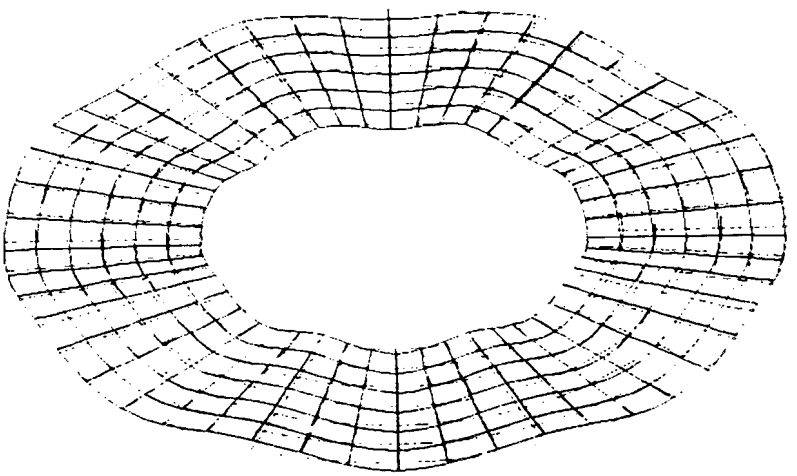

Fig. 2.6 Wrinkle pattern of a circular sheet with free edge, predicted with the FEM code ABAQUS, [Ni et al., 1990]

When using two dimensional FEM techniques, it is very hard to determine the occurrence of wrinkles. In FEM simulations, prediction of wrinkling was also made using shell elements. According to Ni et al., [1990] who used the FEM code ABAQUS (3D) to predict the flange wrinkling behavior of a circular blank in deep drawing for a reliable analysis an elastic-plastic shell element is required because the sheet metal undergoes finite deformation as the wrinkles grow or multiply. The predicted wrinkle pattern of the deep drawing process without a blank holder is shown in Fig. 2.6. The compressive strains that cause wrinkling are small, varying from -0.02% to -0.5%.

2.4.2 Necking

Two different types of necking may occur in deep drawing; namely diffused necking and localized necking. The major cause for the occurrence of necking is the amount of deformation. During a deep drawing operation, material from the flange will draw-in and bend over the die corner radius. Then, as draw-in continues, the material will unbend and enter the unsupported region. Due to strain hardening, this material is strengthened. However, the material just above the punch nose is only bent and thus not as much strengthened as the material that has entered the unsupported region. Since fracture occurs at the weakest spot, mostly it is at the punch nose, depending on the value of the strain hardening exponent.

Levaillant and Chenot, [1992], describe a frictionless test. This is the only way to determine the effect of material properties on necking and fracture. A uniaxial tensile test with rectangular parallel gauge length is conducted. Then the friction, due to contact with a solid tool, is surpressed. This is the most common test used for identification and validation of the constitutive equations. The most materials are strain-rate sensitive, temperature sensitive, non-isotropic. Thus, these parameters should be included in the constitutive equation to give a realistic description of the material behavior. The temperature sensitivity means that increasing the temperature decreases the yield stress and strains. Mostly, the higher the R-value (normal anisotropy factor) the better is the formability. This means that fracture occurs at a larger punch travel, so the drawing ratio can be increased. Some tests involve friction such as the Olsen or Erichsen ball punching test, hemispherical dome test. For deep drawing, there is an

axisymmetric case namely the Swift Cup test with a flat bottomed cylindrical punch. Depending on lubrication (friction) and blank holder pressure, failure will occur in the flange or at the punch corner radius.

Most laboratory tests are conducted at a tensile rate of about 10^{-3} s^{-1}, but the tensile rate in stamping is about a few s^{-1}. This is a very complex problem. Increasing the tensile rate causes the onset of necking earlier, but post uniform elongation can be increased. This means that the total rupture elongation may decrease or increase depending on material properties. In summary it is very important to describe the material behavior carefully including anisotropy, temperature, and strain rate sensitivities.

2.5 Discussion on previous simulations

Simulations neglecting bending effects are usually performed using membrane elements. Bending effects can be neglected during the simulations depending on the tool geometry. The most important parameters of the tool geometry influencing the amount of bending are (a) the die corner radius r_d, (b) the punch corner radius r_p, and (c) the sheet thickness t. The BHF is also very important. These symbols are shown in Fig. 2.3. The influence of bending effects is especially significant when the r_d/t ratio decreases in nearly plane strain conditions. Including the bending effects in the simulation (by using solid or shell elements) increases the CPU time, but the results are more realistic. Choudry and Lee, [1990] simulated several sheet metal forming processes including bending effects. The membrane theory neglects bending effects, so it is only possible to obtain realistic results for large r_d/t ratios. If the r_d/t ratio is less than 10, the bending effects can not be neglected anymore, according to Batoz et al., [1989]. Then, because membrane codes neglect stress and strain variations through the thickness direction, the results are no longer realistic. If the bending effects are not included, it is impossible to simulate local or global wall wrinkling, [Batoz et al., 1989]. Bending effects in deep drawing are discussed in more detail in Chapter 4.

2.5.1 Simulations neglecting bending effects

Rebelo, Nagtegaal and Hibitt, [1989] used the FEM code ABAQUS to simulate axisymmetric deep drawing. Membrane elements (120) with a low bending stiffness are used for the blank. Four elements through the thickness are used to compensate this low bending stiffness and to observe stress and strain gradients through the thickness. The geometry and process parameters are shown in Table 2.4 using the symbols shown in Figure 2.3. Observing the r_d/t and r_p/t ratios shows that according to Batoz et al., [1989] bending effects are not negligible anymore. However, in this simulation the effects are neglected. Rigid bodies are used to define the tools. Coulomb friction is assumed. An additional limit on the maximum allowable shear stress (stiffness in sticking) is specified to prevent that the surfaces slide in any direction or may be stuck rigidly together. The surfaces can stick if the shear force is smaller than the friction force. After deep drawing, the thickness changes are from (-12 %) over the punch corner to (+16 %) at the edge of the formed cup. CPU times, punch force distributions and strain distributions are not included in the paper.

Table 2.4 Tool geometry and process parameters used by Rebelo et al., [1989] symbols as in Fig. 2.3, using aluminum killed steel

Ludwik-Hollomon hardening $\bar{\sigma} = K(\bar{\varepsilon} + \bar{\varepsilon}_0)^n$			
Strength coefficient K	=	513	MPa
Strain-hardening exponent n	=	0.223	[-]
Punch radius (R_p)	=	50	m m
Punch corner radius (r_p)	=	13	m m
Die radius (R_d)	=	51.25	m m
Die corner radius (r_d)	=	5.0	m m
Blank radius (R)	=	100	m m
Blank thickness (t)	=	0.82	m m
Blank holder force	=	100	kN.
Friction coefficient μ (die and sheet)	=	0.15	[-]
Friction coefficient μ (punch and sheet)	=	0.125	[-]
Stroke	=	60.0	m m

Saran, Schedin, Samuelsson, Melander and Gustafsson, [1990] also simulated the axisymmetric deep drawing process. The elastic-plastic material description with Hill's anisotropic model (R=1.65) is assumed. Membrane, triangular, constant strain elements are used. Thus bending effects are not included. The process parameters and tool geometry using the symbols shown in Figure 2.3 are listed in Table 2.5. The punch speed is 25 mm/sec and the effictive stress-effective strain relation is given by the Ludwik-Hollomon expression $\bar{\sigma} = K(\bar{\varepsilon})^n$. The draw-in at the flange area is compared with experimental results for five different materials. The result for 70/30 brass steel is shown in Fig. 2.7a. The comparison of the radial and circumferential strain predictions with the experimental measurements in deep drawing of Deep Drawing Quality Steel is shown in Fig. 2.7b. A good agreement between experiments and simulation is found for the different materials.

A parametric study was conducted to show the influence of n (work hardening exponent), K (Strength coefficient), R (normal anisotropy value), and μ (Coulomb friction coefficient) on the punch force. These results are shown in Fig. 2.7c. Most of these parameters have an evident influence on the punch force, so they should be very carefully determined. However, the value of R (normal anisotropy value) has a minor influence on the punch force.

Table 2.5 Tool geometry and process parameters used by Saran et al., [1990], symbols as in Fig. 2.3 using Deep Drawing Quality Steel

Material follows Ludwik-Hollomon relation $\bar{\sigma} = K(\bar{\varepsilon})^n$			
Strength coefficient K	=	895	MPa
Strain-hardening exponent n	=	0.42	[-]
Punch radius (R_p)	=	50.0	mm
Punch corner radius (r_p)	=	13.0	mm
Die radius (R_d)	=	51.25	mm
Die corner radius (r_d)	=	5.0	mm
Blank radius (R)	=	100	mm
Blank thickness (t)	=	0.70	mm
Blank holder force	=	80.0	kN
Friction coefficient μ (die and sheet)	=	0.22	[-]
Friction coefficient μ (punch and sheet)	=	0.22	[-]
Stroke	=	40.0	mm

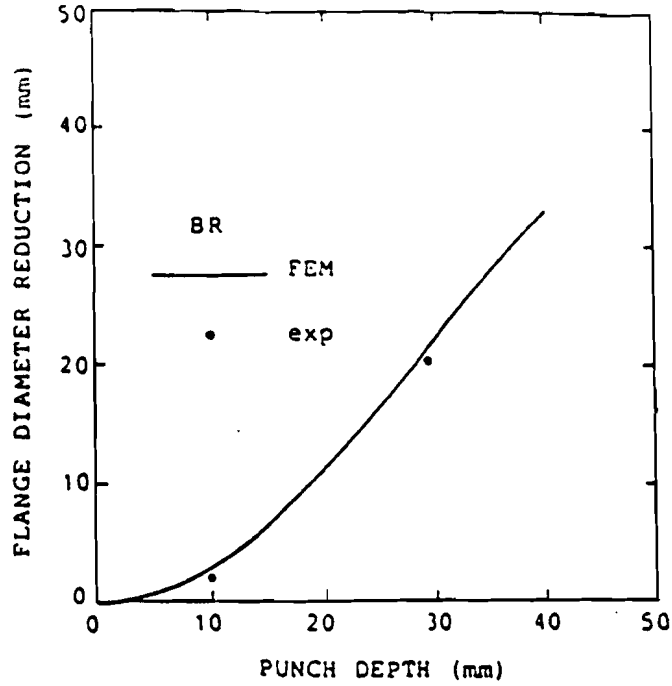

Fig. 2.7a Draw-in of the flange for 70/30 brass steel, [Saran et al., 1990]

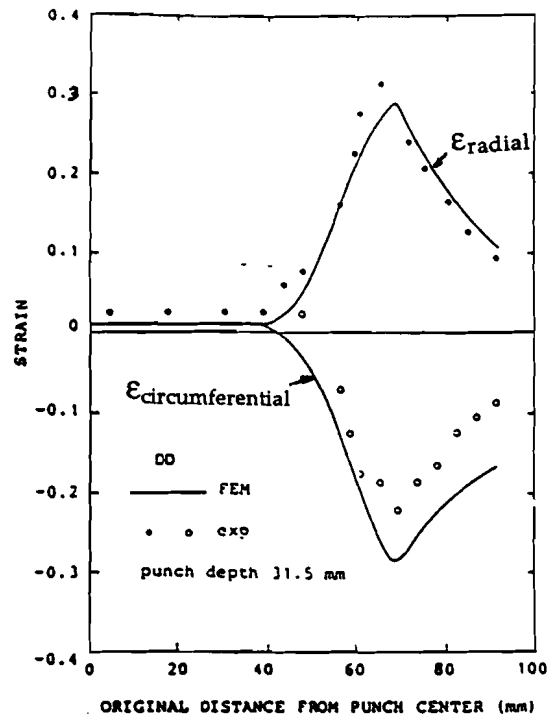

Fig. 2.7b Numerically and experimentally determined radial and circumferential strain distributions for deep drawing quality steel, [Saran et al., 1990]

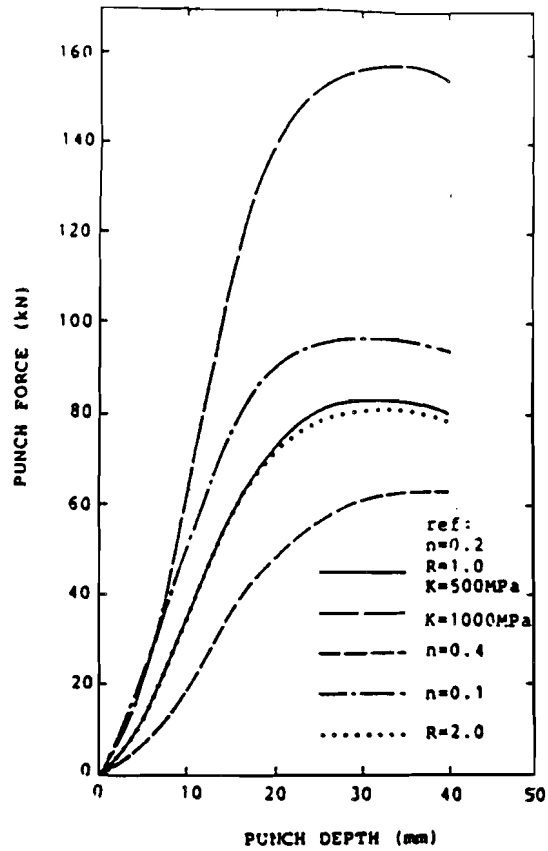

Influence of material parameters on punch force

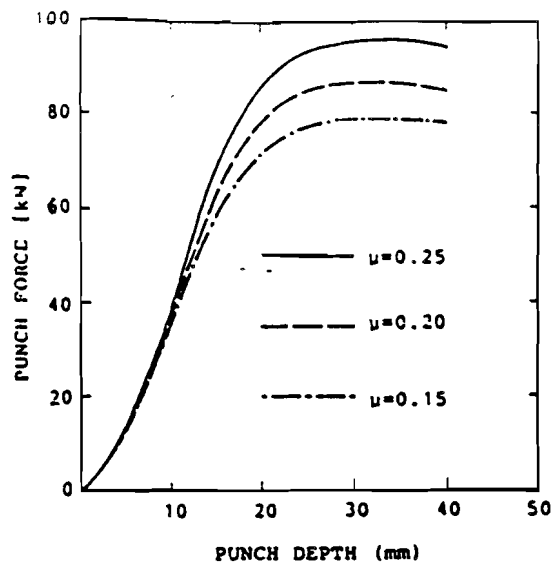

Influence of the friction on the punch force tested for deep drawing steel

Fig. 2.7c Results from parametric study, showing the influence of n, K, R and μ on the punchforce, [Saran et al., 1990]

Deits, Van Tyne and Matlock [1990] simulated the axisymmetric deep drawing process by modeling the tools as elastic bodies, instead of being rigid as commonly assumed. The tool geometry and process parameters are shown in Table 2.6 using the parameters shown in Figure 2.3. The mesh distribution to define the tools and the workpiece is shown in Fig. 2.8. NIKE2D is used to simulate the forming process. The elastic-plastic workpiece is defined by 600 elements. The material properties are not specified.

Table 2.6 Tool geometry and process parameters used by Deits et al., [1990], symbols as in Fig. 2.3

Punch radius (R_p)	=	25.4	m m
Punch corner radius (r_p)	=	6.35	m m
Die radius (R_d)	=	26.2	m m
Die corner radius (r_d)	=	6.35	m m
Blank radius (R)	=	50.8	m m
Blank thickness (t)	=	0.76	m m
Blank holder force	=	4.0	kN
Friction coefficient μ(die and sheet)	=	0.10	[-]
Friction coefficient μ(punch and sheet)	=	0.10	[-]
Stroke	=	38.1	m m

Three layers of elements are used in the sheet thickness direction in order to observe strain or stress gradients through the thickness. The CPU time on a VAX 8600 was 480 hours. The Coulomb friction law is used to describe the friction in the interfaces.

The load-stroke diagram agrees well with conducted experiments as shown in Fig. 2.9. The binderplate displacement is an indication of the thickening of the flange. In the lower die, there are two stress peaks. One of them is where the sheet bends around the die radius, the second one is where the sheet separates from the die.

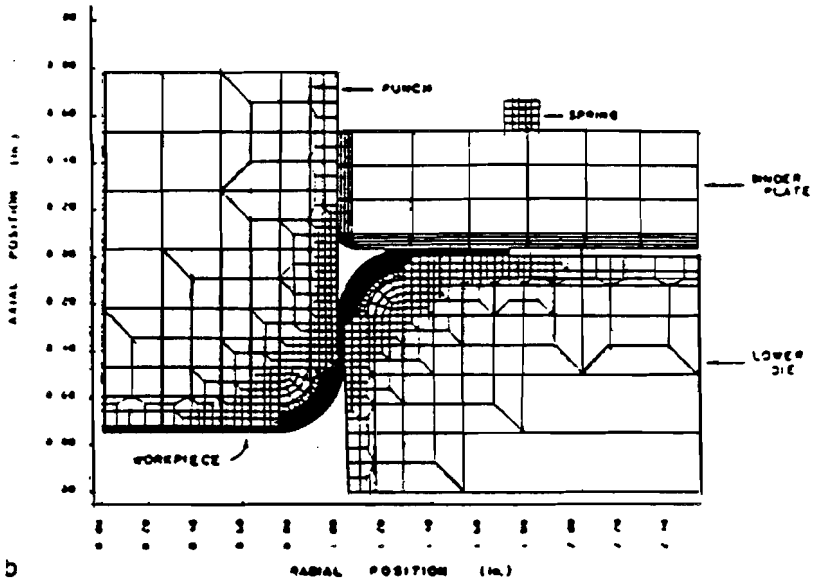

Fig. 2.8 FEM mesh of workpiece and tooling after a punch displacement of 0.75 inches, [Deits et al., 1990]

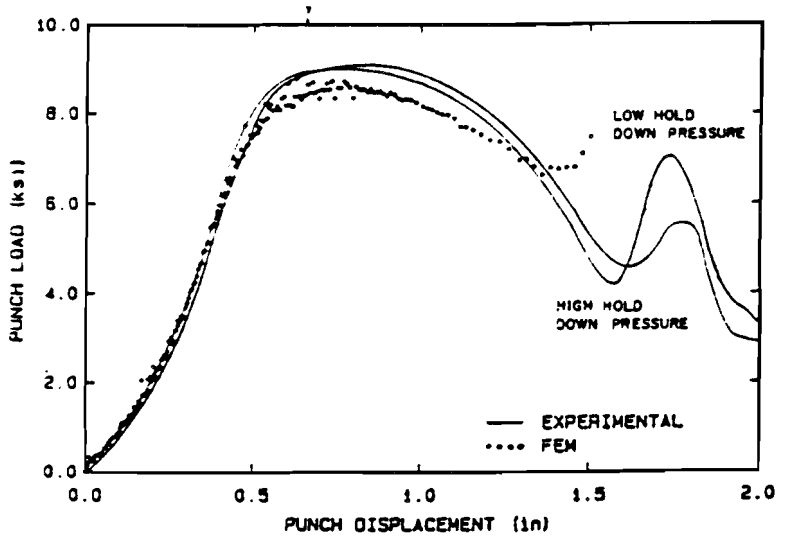

Fig. 2.9 Load-stroke diagram showing experimental and numerical results, [Deits et al., 1990]

2.5.2 Simulations including bending effects

Herrmann and Lange, [1988] simulated the deep drawing processes using solid elements to include bending effects. The geometry and process parameters are shown in Table 2.7, using the symbols shown in Fig. 2.3.

Table 2.7 Tool geometry and process parameters used by Hermann and Lange, [1988], symbols as in Fig. 2.3, material SAE 1006 (deep drawing steel)

Material follows Ludwik-Hollomon law: $\bar{\sigma} = K(\bar{\varepsilon})^n$			
Strength coefficient K	=	554	MPa
Strain-hardening exponent n	=	0.24	[-]
Punch radius (R_p)	=	30	m m
Punch corner radius (r_p)	=	12	m m
Die radius (R_d)	=	32	m m
Die corner radius (r_d)	=	10	m m
Blank radius (R)	=	60	m m
Blank thickness (t)	=	2	m m
Blank holder force	=	unknown	
Friction coefficient μ (die and sheet)	=	0.0	[-]
Friction coefficient μ (punch and sheet)	=	0.0	[-]
Stroke	=	19.2	m m

In this geometry, bending effects are no longer negligible to model the process properly, because the r_d/t ratio is 5. In Chapter 4 it is shown that the bending strains are about 10 % for this ratio. The FEM code used in the simulation is EPDAN (Elastic Plastic Deformation ANalysis). The plastic behavior of the material is described by the Ludwik-Hollomon expression ($\bar{\sigma} = K(\bar{\varepsilon})^n$). The workpiece is defined by 160 quadrilateral elements, using four elements in thickness direction. Friction is assumed to be zero. As the results, the spread of the plastic zone at several stages during the drawing, the velocity fields for different punch travels, and tangential and radial stresses are represented. At the beginning of the deep drawing process the flange remains completely elastic and the deformation is localized at the zone of free bending between die and punch radius. While deformation proceeds, the flange is the first part to be totally plastic.

Belingardi et al., [1989] used the FEM code MARC to simulate the deep drawing process. The geometry of the tools and process parameters are shown in table 2.8 (using the symbols shown in Fig. 2.3) and Fig. 2.10. Material properties were not specified. The workpiece was modeled in three different ways to observe the influence of the different types of elements and the mesh configuration on the radial strain distribution. The three models are (see Fig. 2.10 for sketch of mesh):

1) one row of 50 solid elements
2) three rows of 100 solid elements (tools are defined by gap elements)
3) one row of 40 shell elements (tools are defined by rigid surface elements).

Table 2.8 Tool geometry and process parameters used by Belingardi et al., [1989], symbols as in Fig. 2.3

Punch radius (R_p)	=	57.5	m m
Punch corner radius (r_p)	=	16.5	m m
Hemispherical punch radius	=	115	m m
Die radius (R_d)	=	59	m m
Die corner radius (r_d)	=	15	m m
Blank radius (R)	=	99	m m
Blank thickness (t)	=	1.5	m m
Blank holder pressure	=	0.6	N/mm^2
Friction coefficient μ(die and sheet)	=	0.0	[-]
Friction coefficient μ(punch and sheet)	=	0.0	[-]
Stroke	=	65	m m

The results agree well with the experiments for the three cases. Using 50 axisymmetric solid elements is enough to obtain a good insight in the strain distributions. Refinement of the mesh improves the results, but also increases the CPU time. If the workpiece is defined by 50 solid elements the CPU time is 49 minutes on a VAX8840 machine, while the arrangement in three rows results in a CPU time of 584 minutes on the same machine. Using shell elements seems to be a good compromise between modeling of the bending behavior and a reasonable CPU time (40 minutes on an IBM 3090/150 machine).

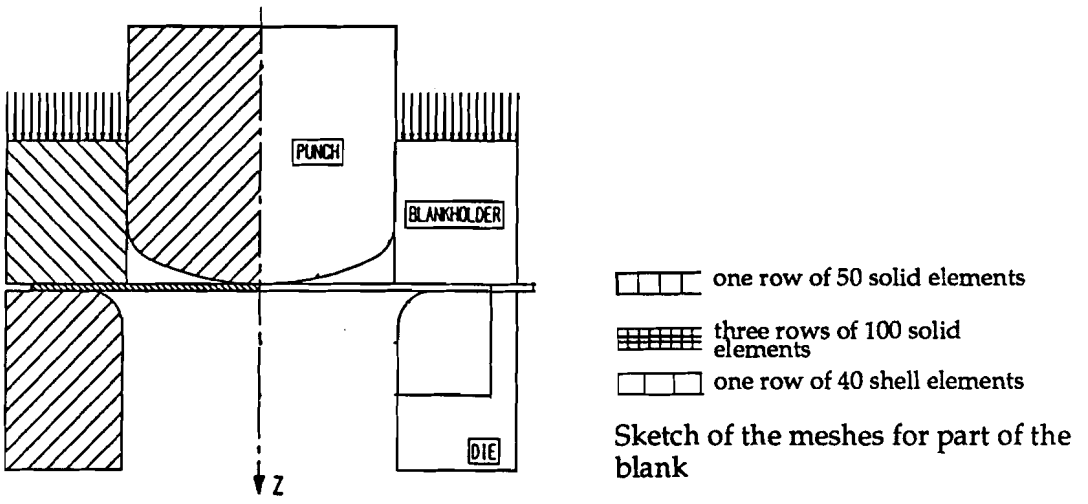

Fig. 2.10 Geometry of blank, punch, and die and sketch of different meshes as used by Belingardi et al., [1989]

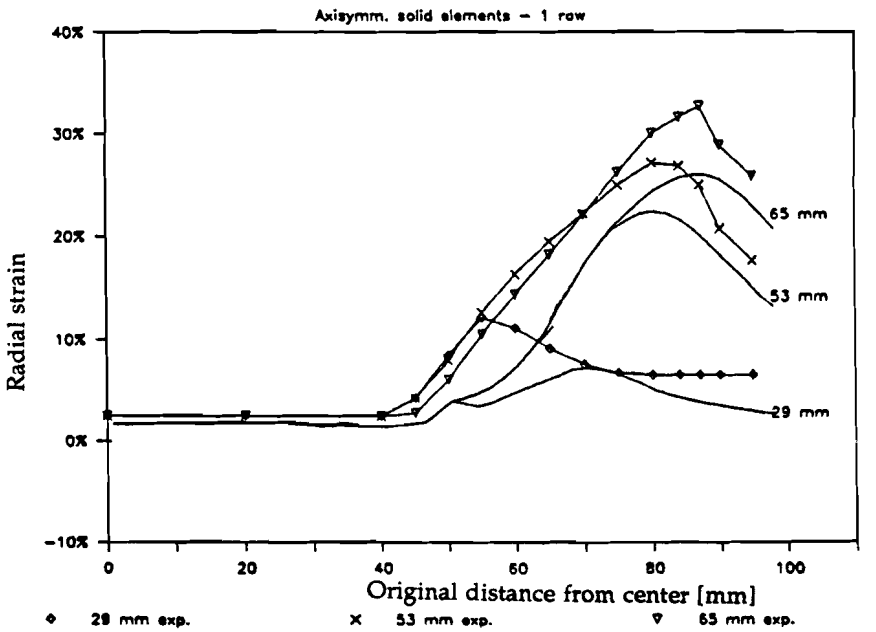

(a) Radial strain distribution for one row of 50 solid elements

Fig. 2.11 Radial strain distributions for different mesh configurations, [Belingardi et al., 1989]

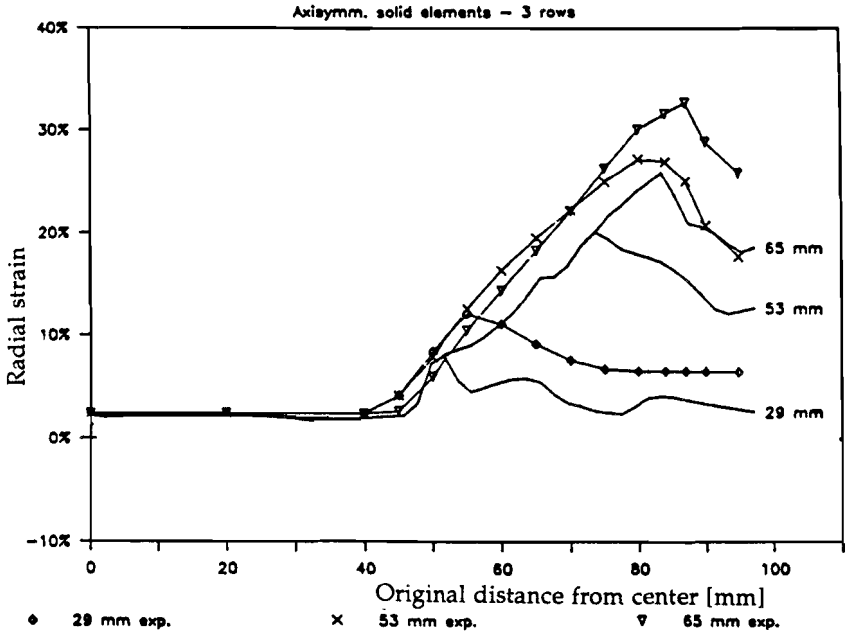

(b) Radial strain distribution for three rows of 100 solid elements

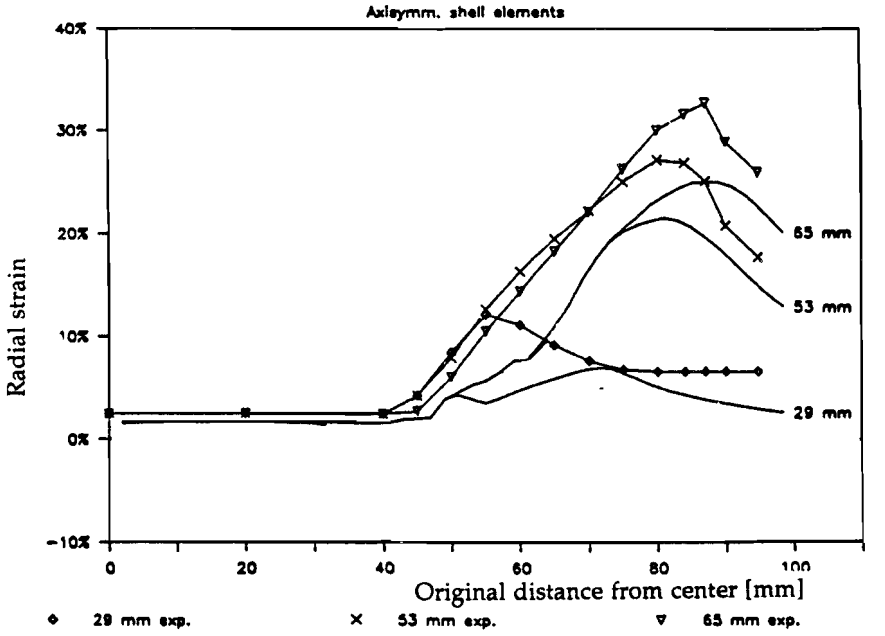

(c) Radial strain distribution for one row of 40 shell elements

Fig. 2.11 Continue

Belingardi et al., [1990] simulated the deep drawing of a complete cup in two drawing steps. In the first step, the same geometry as in Belingardi, [1989] was used as shown in Table 2.8 and Fig. 2.10. The geometry of the tools and process parameters for the second drawing step are shown in Table 2.9 using the symbols as shown in Fig. 2.3. The blank was simulated by one row of 50 axisymmetric solid elements using the FEM code MARC. Assuming elastic-plastic material behavior is necessary to observe the springback between the first and second step and at the end of the second step.

Table 2.9 Tool geometry and process parameters for second drawing step as used by Belingardi et al., [1989], symbols as in Fig. 2.3

Punch radius (R_p)	=	50	m m
Punch corner radius (r_p)	=	38.0	m m
Hemispherical punch radius	=	69	m m
Die radius (R_d)	=	52	m m
Die corner radius (r_d)	=	15	m m
Initial cup radius (R)	=	59	m m
Blank thickness (t)	=	1.5	m m
Friction coefficient μ(die and sheet)	=	0.0	[-]
Friction coefficient μ(punch and sheet)	=	0.0	[-]
Stroke	=	52	m m

After finishing the first drawing step, the tools were withdrawn in order to eliminate any contact. Now, the formed cup has its own configuration under its internal stresses. Then, the second step can start with a punch stroke of 52 mm. The thickness changes during the second step are very small, less than 0.1 mm, probably because of the small drawing ratio from the first to second step (drawing ratio is 1.13). If the drawing ratios from the first to the second step are small, the critical phases are concentrated in the first step (from blank to cup). To compare the influence of the second step another simulation was conducted. In this simulation the first step was bypassed. Then the maximum reduction in thickness strain is 0.25 mm. In Fig. 2.12. the thickness strains after the first step and the second step are shown during six different stages of the punch travel. If the friction is added, the thickness reduction can be higher because the friction force reduces material under the punch corner from sliding to the punch corner and it lets the material stick at the center.

Hambrecht et al., [1989] used 2D solid, 2D membrane and bending (or shell) finite element models in axisymmetric punch stretching to investigate the influence of bending effects. The specified friction coefficients were assumed to be 0.30. The geometry of the tools and the process parameters are given in Table 2.10. Three different programs (a membrane program, NIKE2D and BEND (1D shell elements)) were used in the simulations. The membrane program uses 64 constant strain triangular elements. In NIKE2D the solid element is quadrilateral and suitable for plane-strain, plane stress and axisymmetric geometries. The BEND program uses only 24 1D-shell elements resulting in a CPU time of 6 minutes on a VAX8850 machine to reach a punch height of 37.7 mm. The material model is elastic-plastic. In the NIKE2D simulation the CPU time is 1.25 hours on a VAX 8850 machine using 3 layers of 100 elements. Hambrecht concluded that for sharper tool radii (increasing bending effects) solid and shell models provided more realistic results. The shell model is more efficient because solid models require a larger number of elements to define sufficient degrees of freedom. The radial and circumferential strains are shown in Fig. 2.13a and b. The difference between membrane codes and shell and solid codes is not significant in this case since there is no sliding and unbending in punch stretching.

Table 2.10 Tool geometry and process parameters used by Hambrecht et al., [1989], symbols as in Fig. 2.3, using 70/30 brass steel

Power hardening law:	$\bar{\sigma} = K\bar{\varepsilon}^n \dot{\bar{\varepsilon}}^m$, m = 0		
Strength coefficient K	=	786	MPa
Strain hardening exponent n	=	0.47	[-]
Punch radius (R_p)	=	52.85	m m
Punch corner radius (r_p)	=	6.35	m m
Die radius (R_d)	=	57.95	m m
Die corner radius (r_d)	=	6.35	m m
Blank radius (R)	=	60	m m
Blank thickness (t)	=	0.94	m m
Blank holder pressure	=	0.0	N/mm^2
Friction coefficient μ (die and sheet)	=	0.3	[-]
Friction coefficient μ (punch and sheet)	=	0.3	[-]
Stroke	=	12	m m

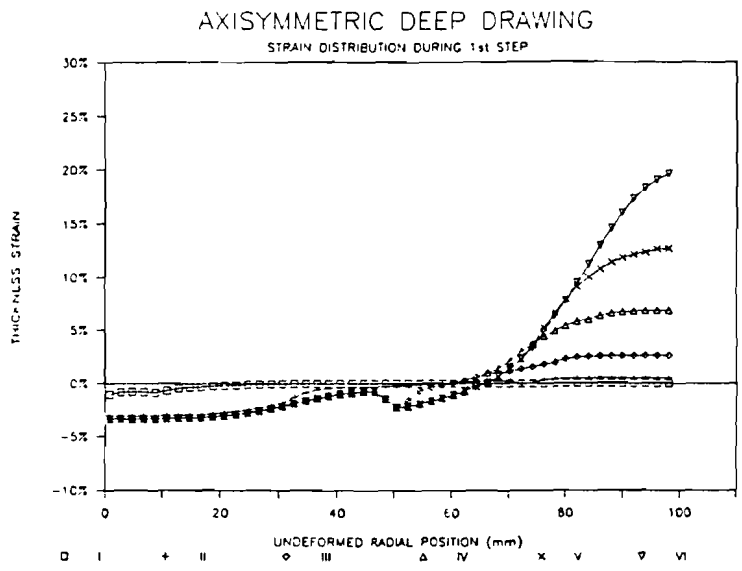

Fig. 2.12a Thickness strains during different stages of the punch travel for first drawing step, [Belingardi et al., 1990]

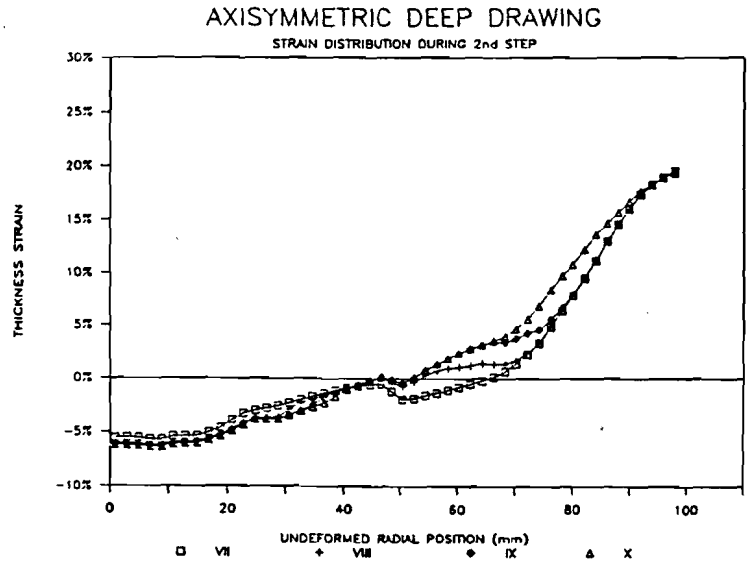

Fig. 2.12b Thickness strains during different stages of the punch travel for the second drawing step, [Belingardi et al., 1990]

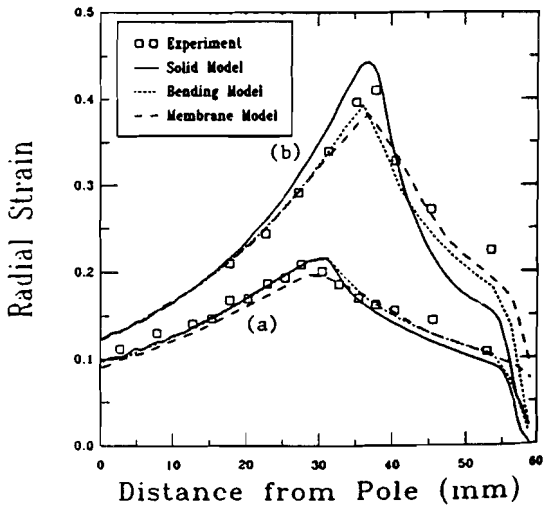

Fig. 2.13a Radial strains at the outside of the cup at punch stroke of (a) 29.2 and (b) 37.7 mm, [Hambrecht et al., 1989]

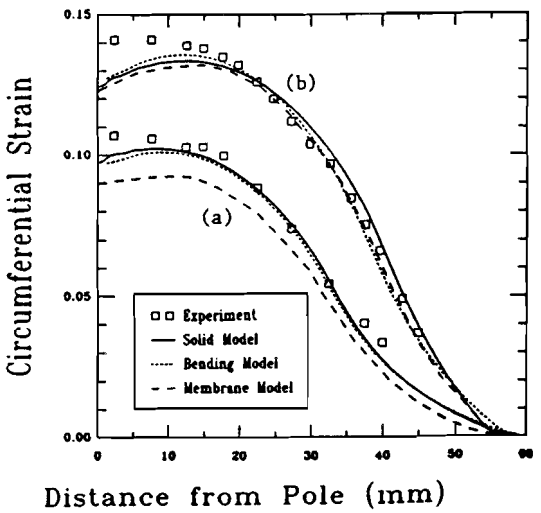

Fig. 2.13b Circumferential strains at the outside of the cup at punch stroke of (a) 29.9 and (b) 37.7 mm, [Hambrecht et al., 1989]

CHAPTER III

APPLICATIONS OF "DEFORM" IN SHEET METAL FORMING

In this chapter, a brief background on DEFORM is given and the results of the DEFORM simulations in deep drawing and stretch forming are presented. Comparisons are made with the Benchmark test (deep drawing as well as plane-strain stretch forming), ABAQUS, and experiments. These comparisons are made to investigate the applicability of DEFORM in sheet metal forming and to validate the use of DEFORM in the further investigations of this report.

3.1 Brief background on DEFORM

The basic concept of the finite element method is one of discretization. The construction of the finite element model is as follows: In the domain of the function, a number of finite points (nodal points) and the values of the function and its derivatives are specified. The domain of the function is approximately represented by a finite collection of subdomains (finite elements). Assembling the elements and connecting them appropriately on their boundaries defines the domain. Within each element, the function is approximated locally by continuous functions which are uniquely described in terms of the nodal point values associated with the particular element. The path of the solution of a finite element problem consists of five specific steps, [Oh et al., 1989]:

a) identification of the problem
b) definition of the elements
c) establishment of the element equations
d) assembly of element equations
e) numerical solution of the global equations

The formulation of element equations is accomplished from one of four directions:

a) direct approach
b) variational approach
c) method of weighted residuals
d) energy balance method

The basis of the finite element metal flow modeling, using the variational approach as used in DEFORM, is to formulate proper functionals, depending on specific constitutive relations. The solution of the original boundary value problem is obtained by the solution of the dual variational problem in which the first order variation of the functional vanishes. The functional is expressed locally within each element with the nodal point values, by choosing an approximate interpolation function for the field variable in the elements. Then the local equations are assembled into the overall problem and the functional is approximated by a function of global nodal-point values. The stiffness equations are obtained by the condition of the function to be stationary. These stiffness equations are then solved under appropriate boundary conditions, [Kobayashi, Oh and Altan, 1989].

DEFORM means Design Environment for Forming and the main application of the 2D code is to simulate billet forming such as bulk forming processes, cold and hot forging, extrusion and rolling. The material behavior is based on rigid-viscoplastic FEM formulation.

3.1.1 Pre-Processing in DEFORM

In the pre-processing mode of a FEM code the problem has to be defined and modeled. This means the tools have to be defined, the workpiece must be divided into elements, the interface boundary conditions between the workpiece and the tool surfaces have to be defined.

Definition of tool geometry and mesh generation

In DEFORM the tools can be defined as rigid, elastic and porous bodies. If they are rigid, the definition of the tools is done just by entering and connecting geometrical simple standard features such as lines and arcs. When the tools are

elastic or plastic, they have to be divided into elements. DEFORM has an automatic mesh and remesh generator which consists of two program modules, one for the determination of the optimum density distribution and the second one for the mesh construction. The mesh generator creates the mesh automatically using 4-node quadrilateral solid elements, and determines the optimum density. The optimum mesh density is determined by (a) the geometric shape of the object to be meshed, (b) the strain rate distribution, (c) the temperature distribution and, (d) the strain distribution, [Oh et al., 1991]. This can be user defined (the mesh density can be changed if necessary) or system defined (in this case the mesh density is constant which means that each element has the same initial dimensions).

To ensure a proper approximation of the FEM mesh, a geometric shape criterion is necessary. The strain-rate and temperature distributions are used to distribute the solution error uniformly in a similar manner to that of the adaptive meshing method. The strain distribution is in general not included in the solution error analysis directly. However, to preserve the accumulated strain distribution during remeshing operations a mesh density based on the strain distribution is necessary. The automatic mesh generator constructs the mesh automatically using 4 node quadrilateral elements once the optimum mesh density is determined at every point of the domain to be meshed.

If there is a considerable amount of plastic deformation, FEM simulations require mesh regeneration during the simulation. In DEFORM, the AMG (Automatic Mesh Generator) automatically (no user interference) carries out the following tasks during remeshing:

- determine the need for remeshing
- determine the optimum mesh density based on the geometric shape and the previous solution behavior
- construct the mesh based on the optimum mesh density
- transfer all necessary information including boundary conditions from the old mesh to the new
- continue the simulation for completion

Definition of the material properties

The material properties of the workpiece to be specified are elastic or plastic and/or thermal properties. For the rigid-plastic formulations, the Hollomon equation is used:

$$\bar{\sigma} = K(\bar{\varepsilon} + \bar{\varepsilon}_0)^n \dot{\bar{\varepsilon}}^m + \sigma_y \qquad (3.1)$$

Where	$\bar{\sigma}$	=	effective stress	[N/mm²]
	K	=	strength coefficient	[N/mm²]
	$\bar{\varepsilon}$	=	effective strain	[-]
	$\bar{\varepsilon}_0$	=	effective pre strain	[-]
	n	=	strain hardening exponent	[-]
	$\dot{\bar{\varepsilon}}$	=	effective strain-rate	[1/sec]
	m	=	strain-rate sensitivity exponent	[-]
	σ_y	=	yield stress	[N/mm²]

It is not necessary to define the material to be strain-rate sensitive, and the yield stress of the material does not have to be specified. When specifying a tool or workpiece as a fully elastic body the following material input data are required:

E	=	Young's modulus	[N/mm²]
υ	=	Poissons ratio	[-]

Friction models in DEFORM

Boundary conditions and, if necessary, initial conditions such as pre-strain, initial temperature, etc., need to be specified for the tools and workpiece at a range of nodal points through graphics or alpha numerical. DEFORM is able to generate movement control, prescribed velocity, force, pressure, heat exchange with environment, prescribed heat, temperature and temperature flux boundary conditions. Friction is defined as a slave-master or master-slave contact. Coulomb or Tresca friction can be chosen in DEFORM

Coulomb friction: $\tau_f = \mu\sigma_n$ (3.2)

Where	τ_f	=	Friction stress	[N/mm²]
	μ	=	Coulomb friction coefficient	[-]
	σ_n	=	Normal stress	[N/mm²]

Coulomb friction is proportional to the normal force and it is independent of the size of the contact area.

Tresca friction: $$\tau_f = m\frac{\sigma_y}{\sqrt{3}} \qquad (3.3)$$

Where	τ	=	Friction stress	[N/mm²]
	m	=	Tresca friction coefficient ($0 < m < 1$)[-]	
	σ_y	=	Yield stress	[N/mm²]

Tresca friction is proportional to the yield stress of the material.

Interface conditions and formulation

To incorporate interactions between tools and the workpiece the contact conditions need to be defined by the interface formulation (interface boundary conditions). In Appendix A the contact condition is more detailed described. The basic equations that have to be satisfied during a forming process are given in Appendix A, using a variational approach as in DEFORM.

3.1.2 Post-Processing in DEFORM

The DEFORM post-processor provides three basic functions

- alphanumeric output of results for user inspection
- alphanumeric output of results for CAD/CAM interface
- graphic display of results

The standard features of the graphic display are:

- FEM mesh display for each stored step
- Contour display of effective strain, strain rate, stresses
- Temperature distribution
- Velocity distribution
- Load-stroke diagram

In the post-processing mode, however it is not possible to obtain the radial strain, thickness strain, or circumferential strain directly. Those have to be calculated using another program or manually using the point tracking option, which provides the coordinates of any specified points during the deep drawing operation at any specified steps.

3.1.3 DEFORM in sheet metal forming

If the automatic mesh generator is used (system defined), the elements are all defined as squares by the system. The aspect ratio = 1, which is the ratio between element length and element width. DEFORM is mainly used in bulkforming using workpieces (billets) which are square or very thick compared to blanks used in sheet forming operations. Then it is useful to create square elements. However, in sheet metal forming, using thin sheets actually requires rectangular elements. To obtain stress and strain components through the thickness, several layers of elements should be defined in the sheet thickness direction. Therefore, the number of elements increases dramatically. For example, a sheet of 100 mm and 1 mm thickness requires 100 elements when using one element in the thickness direction, 400 for 2 layers, 900 for 3 layers, etc. Because of the fact that the required computation time depends quadratically with the number of elements, it is expected that DEFORM needs a large CPU time for sheet metal forming operations. Patwardhan, [1991] simulated some sheet metal forming problems such as plane strain V-bending, punch stretching, and deep drawing using DEFORM. Separation occurred in V-bending because the bend radius of the workpiece did not follow the radius of the punch. Punch stretching and deep drawing simulations were performed and some results were compared with NIKE2D simulations. However in these simulations there was no blank holder used because the sheet was very thick and as results only stress components were presented, no strain components. So it was still not very clear whether DEFORM was able to generate accurate strain predictions or not.

Using Coulomb friction is more realistic in sheet metal forming especially in deep drawing because the normal stress or pressure does not remain constant especially at the interface between blank holder and blank during the process. Due to the decrease of the flange area during the drawing operation, the blank

holder pressure will increase when using constant BHF. Thus, the friction stress will increase as well.

3.2 Axisymmetric Deep Drawing

Three axisymmetric simulations are performed to compare the results from DEFORM with other codes and with an ERC experiment. The main objective of these simulations was to validate the use of DEFORM in sheet metal forming, especially in deep drawing.

3.2.1 Comparison of DEFORM with the Benchmark test

The Benchmark test for sheet forming analysis has been performed by twenty five research groups world wide in 1990 and the results were published by Lee, Wagoner, and Nakamichi, [1990]. The main objective was to have a meaningful comparison of results obtained by various analytical methods, using a standard, well defined set of benchmark test. Thus it was possible to compare the accuracy of predictions and the approximate computation times. The test problems consist of simple geometries. Punch stretch and draw forming of a thin sheet under the plane strain and axisymmetric conditions with three different values of coefficient of friction have been simulated. The compared criteria are the load-stroke diagram and the radial strain at a punch travel of 20 and 40 mm. The DEFORM simulation is performed only for the axisymmetric case, with one coefficient of friction, μ = 0.15. This friction occurs at the die sheet interface, the punch sheet interface and the drawbead (blank holder) surface.

The geometry of the tools is shown in Fig. 3.1. The boundary conditions in the draw-in simulations are a constant drawbead force/length DBF = 100 kN/m at a radius of 66 mm. Uniform Coulomb's friction is used, friction coefficient μ=0.15.

Material properties

The material law, isotropic hardening:

$\sigma = 589\ (10^{-4} + \varepsilon)^{0.216}$ (Swift hardening) [N/mm^2]

The elastic properties:

E= 69004 (Young's modulus) [N/mm^2]

$\upsilon = 0.3$ (Poissons's ratio) [-]

(Since the material behavior of the workpiece is assumed to be rigid-plastic in DEFORM, the elastic properties are not necessary)

The draw-in boundary condition (at a radius of 66 mm in Fig 3.1.) can be simulated in many ways, but the physical conditions are:

1) $\Delta U_{edge} = 0$ if $F_{i(stretch)} < DBF$

$F_i = F_d$ if $F_{i(stretch)} > DBF$

Where:

ΔU_{edge} = incremental displacement of node where boundary condition is applied.

F_i = internal force at boundary node

$F_{i(stretch)}$ = internal force at radius of 66 mm when $\Delta U_{edge} = 0$ is the boundary condition

DBF = maximum drawbead resistance force

2) Draw-in could stop if F_i falls below DBF.

The modeling of the draw bead force in DEFORM:

The most important characteristic of this simulation is the way of modeling the drawbead force. As stated in the Benchmark test description, it should be applied at the nodes which are on a radius of 66 mm. The drawbead force is simulated in several ways in DEFORM to investigate what the possibilities and limitations are. The following options are considered:

- Option 1 Apply the drawbead force at the specified nodes (radius = 66 mm)
- Option 2 Elastic blank holder at a radius of 66 mm, on which a pressure is applied which creates a friction force equal to the required drawbead force, i.e. 100 N/mm.
- Option 3 Rigid blank holder at a radius of 66 mm, on which a force is applied which creates a friction force equal to the required drawbead force.

Evaluation of the options

Option 1:

It is impossible in DEFORM to apply the required drawbead force at a radius of 66 mm, because one must specify the range of nodes.

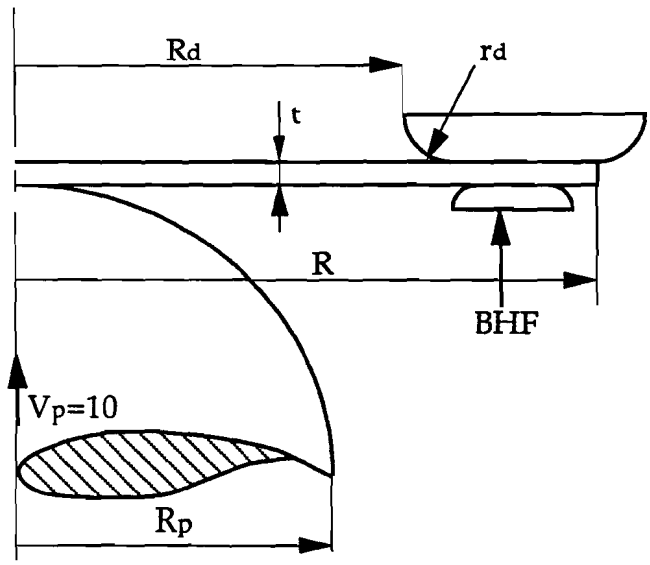

R_p =	50.8	mm
r_p =	50.8	mm
R_d =	53.8	mm
r_d =	6.35	mm
R =	80	mm
t =	1	mm
F =	69000	N
μ =	0.15	[-]

Fig. 3.1 Geometry of the axisymmetric Benchmark test, [Lee, et al., 1990]

It is not possible to select a range of nodes through the thickness direction, then all the nodes from that radius until the outer radius of the metal sheet are selected. However, it is possible to apply the drawbead force at the outer nodes of the sheet (radius = 80 mm), but this is not realistic when modeling a drawbead.

Option 2:
This simulation caused convergence problems, it was impossible to converge within the limits after a very small displacement of the punch. Probably, this is due to the high shear stress acting in the drawbead (blank holder). The coefficient of friction value is varied to investigate its influence, but this did not solve any convergence problems. Because of the increased number of elements used for the blank holder, the CPU time will also increase.

Option 3:
This is probably the method that provides the best results. Less convergence problems than in the other options occur during the simulation. If the flange of the sheet thickens because of the compressive circumferential stresses, the blank holder is automatically displaced in negative y-direction in order to secure the constant 69,000 Newton BHF. A force of 69,000 Newton is applied in the positive y-direction. This creates a friction force of 20,700 Newton in the radial direction with the specified friction coefficients. Both the upper die surface and the blank holder (drawbead) have a coefficient of friction $\mu = 0.15$. Thus, in this situation the drawbead force is 100 N/mm as specified in the Benchmark test.

Limitations when using DEFORM:

The punch nose is slightly flattened to obtain more nodes contacting the punch in the initial stage. In the original geometry, only one node contacts the punch in the beginning of the drawing. This caused convergence problems. After flattening the punch nose, five nodes are contacting in the beginning of the simulation. The total number of elements is 1120 and 4 elements are defined in thickness direction. In Fig. 3.2 the deformed geometry is shown at a punch stroke of 0, 20, and 40 mm. If the sliding error is not specified, the deformed geometry is attracted to the tools, so that the shape is not realistic as shown in Fig 3.2. The unsupported region should be straight because of the tensile stress.

Specifying a sliding error mostly increases the CPU time, and it may cause convergence problems in some cases.

Results and comparison

The Benchmark test was performed by research groups all around the world. Some results of this researchers are very questionable, because of their extreme peaks in the strain distribution. DEFORM is not compared with these results. In Table 3.1 the researchers, whose strain distributions are in a reasonable range, and their FEM code which DEFORM is compared with, are listed. In Fig 3.3 the load-stroke diagram is shown where the two solid lines represent the range of Benchmark results and the crosses represent the DEFORM results. As can be seen there is a good agreement with the most results from the Benchmark test. The CPU time needed to complete the simulation is about 70 hours on a HP 700 series workstation.

Table 3.1 Researchers and their codes compared with DEFORM

Name/Employee	FEM Code	cpu sec, computer	# of element /DOF
ERC/NSM	DEFORM	70 hr, HP700	1240
Lee/Choudry/OSU	Sheet-B, RVP	850 VAX8550	30 el., 124 DOF
Tang/VW-Gedas	Tiefsim, EP	65 CRAY XMP 14	mem., 124 el., 325 DOF
Yang/Kaist	?, RP	610 SUN3/110	mem., 248 el., 441 DOF
Mattiasson/Volvo	ABAQUS, EP	60 IBM3090/300E	solid
Mattiasson/Volvo	ABAQUS,EP	97 IBM 3090/300E	shell
Flower/LLivermore	NIKE2D	26 CRAY XMP	?
Nagtegaal/Hibbitt	ABAQUS , EP	160 VAX 8800	shell 37 el., 93 DOF
Guerra/Los Alamos	NIKE2D, EP	?	solid
Logan*/	SQUIRREL	147 IBM/PS-2386	mem, 20 el., 21 DOF
Rebelo*	MARC	3150 Alliant FX8	104 elements
Sitaraman/OSU	SHEET_FORM, RP	181 VAX8550	100 el., 80 DOF

RVP=rigid visco-plastic, EP=elastic-plastic, RP=rigid-plastic, DOF is degrees of freedom and '*' indicates that their results are out of the specified range (in Fig. 3.5) at a punch stroke of 40 mm , [Lee et al., 1990]

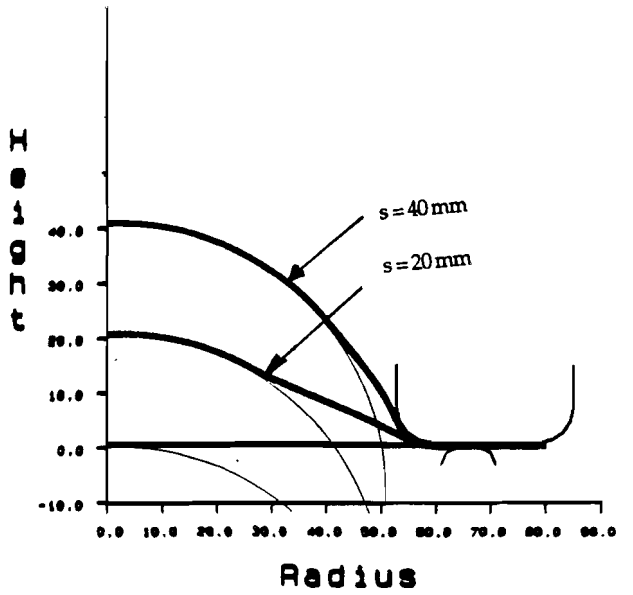

Fig. 3.2 Deformed geometry from DEFORM at a punch stroke of 0, 20 and 40 mm

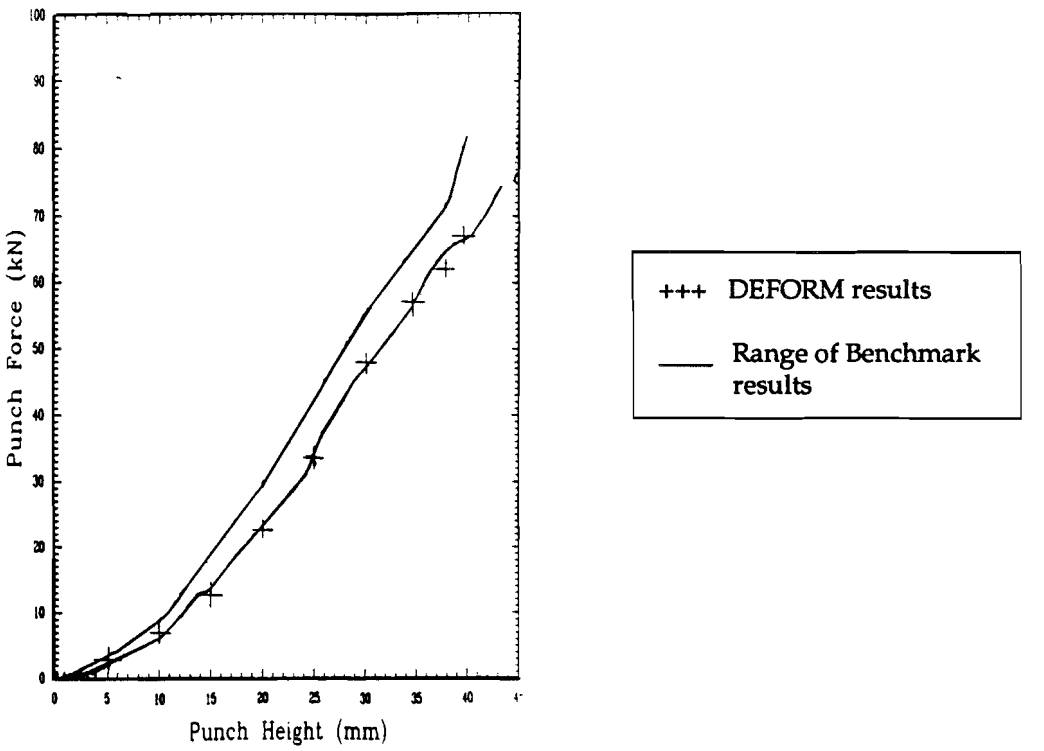

Fig 3.3 Load-stroke diagram for Benchmark test including DEFORM results, where the two solid lines represent the range of reasonable results from the Benchmark test (results as listed in Table 3.1 are within the range)

The strain distributions in radial direction for a punch height of 20 and 40 mm are shown in Fig 3.4 and Fig 3.5. Again, the two solid lines represent the reasonable range of results from the Benchmark test as listed in Table 3.1 and the crosses are the DEFORM results. From these strain distributions in Fig. 3.4 and 3.5 and the load-stroke diagram, one can conclude that DEFORM is able to generate results which are within a reasonable range. Disadvantage is the very high CPU time, due to the large number of elements which are required to model the blank properly.

3.2.2 Strain calculation in DEFORM and definition of radial strain

The radial strain is the strain along the meridian of the sheet as shown in Fig. 3.6. For some applications, the strain at the inner or outer surface is defined as being the radial strain, especially for experimental data. The length of the fiber after deep drawing is obtained by using the point tracking method in DEFORM. Then it is possible to obtain the coordinates of any specified points of the blank during the deep drawing at any specified step.

In this case, a simplified assumption is made that at radii, (punch corner and die corner) the arc length of the two nearby points (distance = 0.1 mm in initial undeformed geometry) equals the distance between these points. In DEFORM, these strains are obtained by calculating the elongation of two very nearby points. The strain is defined as :

$$\varepsilon_{radial} = \ln(l_e/l_o) \qquad (3.4)$$

Where:

l_e = distance between the two points after deformation

l_0 = initial distance between the two points (0.1 mm)

3.2.3 Comparison with ABAQUS

In this simulation an axisymmetric deep drawing operation is simulated. The tool geometry , material and process parameters of this simulation are shown in Table 3.2. This problem is both simulated in ABAQUS and DEFORM to obtain a comparison. There are no experimental data available, so the DEFORM results can not be compared with experiments.

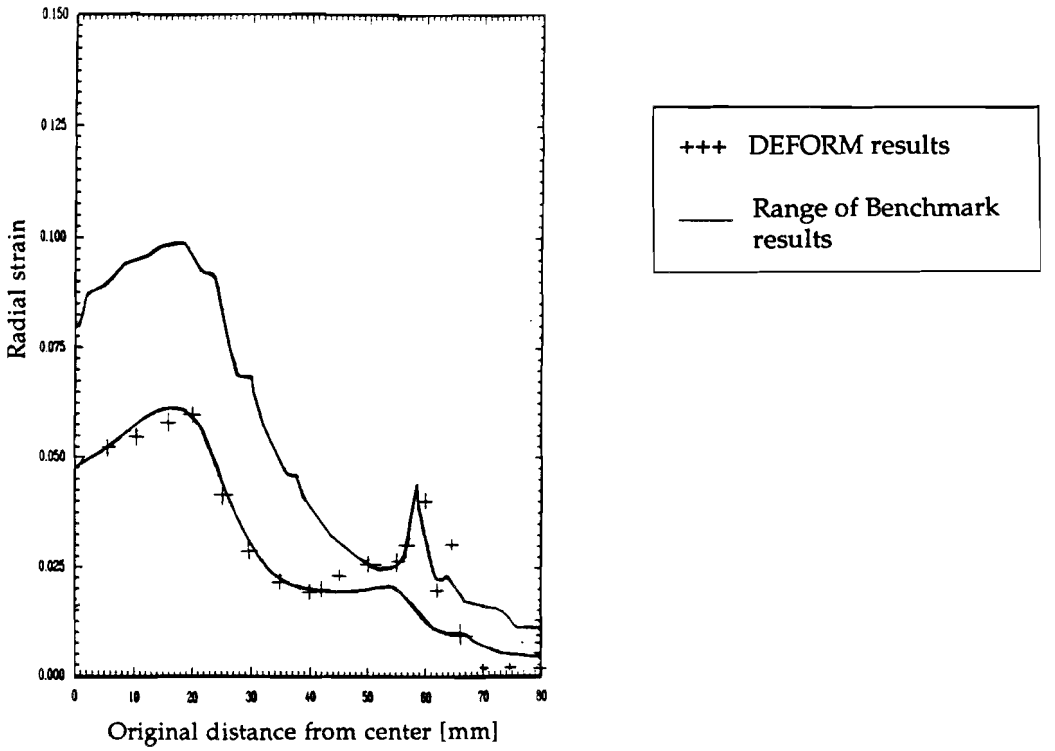

Fig 3.4 Radial strain distribution for both DEFORM and Benchmark test results at a punch stroke of 20 mm, where the two solid lines represent the range of Benchmark results from Table 3.1.

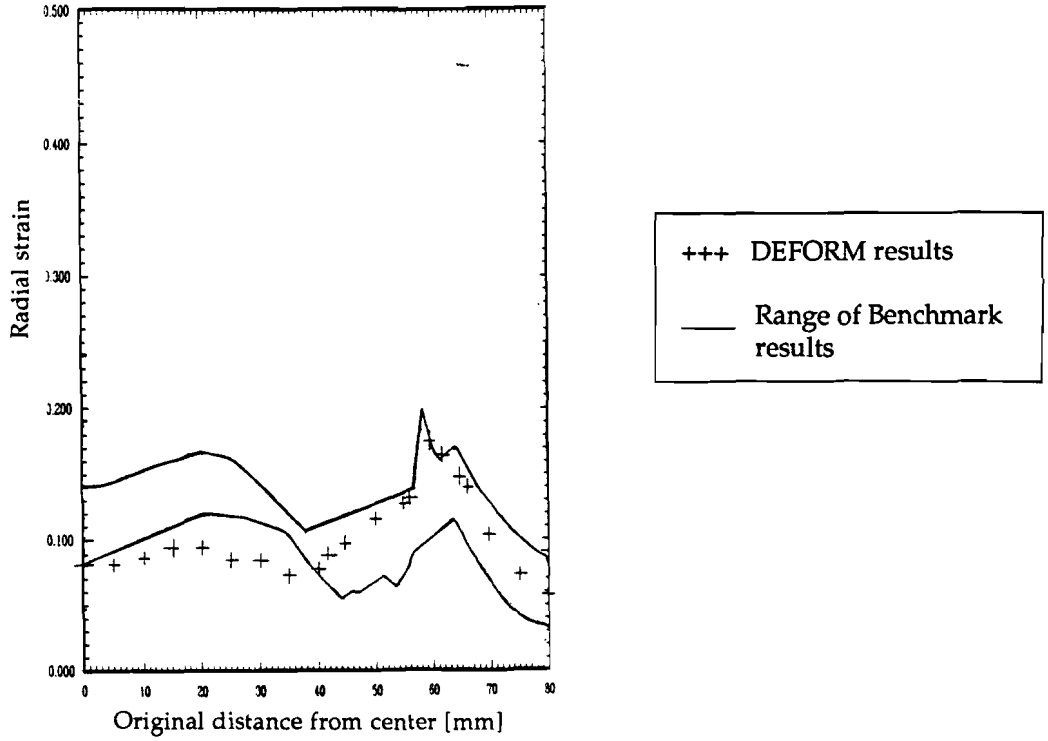

Fig 3.5 Radial strain distribution for both DEFORM and the Benchmark test at a punch stroke of 40 mm, where the two solid lines represent the range of Benchmark results from Table 3.1.

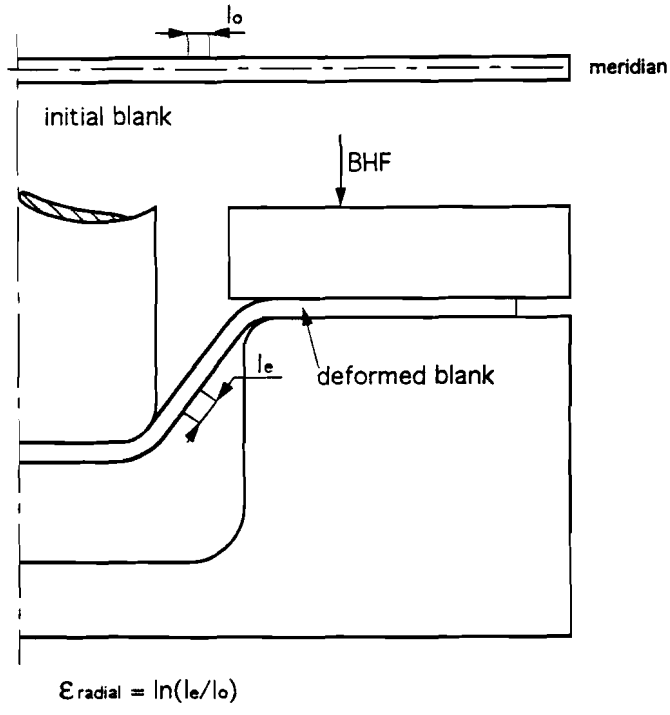

Fig. 3.6 Definition of the radial strain as used in comparison with the Benchmark test

The FEM code ABAQUS is widely used in all different kinds of applications and is accepted as being reliable and able to provide accurate results.

Table 3.2 Tool geometry and process parameters as used in comparison of DEFORM with ABAQUS, symbols as in Fig. 2.3

Strength coefficient K	=	589	[N/mm^2]
Strain hardening exponent n	=	0.225	[-]
Pre-strain ε_0	=	0.001	[-]
Young's modulus E	=	2.1 10^5	[N/mm^2]
Punch radius (R_p)	=	58.1	m m
Punch corner radius (r_p)	=	5.00	m m
Die radius (R_d)	=	59.6	m m
Die corner radius (r_d)	=	5.00	m m
Blank radius (R)	=	100	m m
Blank thickness (t)	=	1.00	m m
Blank holder force	=	11.9	kN
Friction coefficient μ (die and sheet)	=	0.05	[-]
Friction coefficient μ (punch and sheet)	=	0.05	[-]
Stroke s	=	62.5	m m

Mesh and simulation conditions

The simulation with ABAQUS was performed by Van de Koolwijk, [1992], using 240 rectangular solid elements to define the workpiece. Three layers of elements are used in thickness direction, 80 in radial direction. In DEFORM, two different simulations are performed on two different computers (a VAX and a HP series 700). The simulation on the VAX was using a non-uniform mesh with 1500 elements. In the region around the punch and die corner a very fine mesh (to define sufficient degrees of freedom) is used as shown in Fig. 3.7, because of the bending that occurs around the punch corner and die corner radius. The simulation on the HP was using a uniform mesh with 2500 elements. The large number of elements (2500 for uniform mesh and 1500 for non-uniform mesh) is due to the aspect ratio, which = 1 when using the DEFORM mesh generator.

To prevent separation of the sheet under the flat punch nose two different solutions are considered:

a) on the VAX a velocity field with the same direction and velocity of the punch (10 mm/s) was specified (named DEFORM-velocity in graphs)
b) on the HP a pressure of 2.76 MPa from the center of the blank to a radius of 27.59 mm was specified in opposite direction of the punch movement. The total force generated by this pressure is 2391 N, and this force is subtracted in the load-stroke curve to eliminate its influence as will be done in all other future cases when a pressure is applied. In graphs it is called DEFORM-pressure.

The second problem which occurs is the separation in the blank holder/blank interface and blank/die interface. In both DEFORM simulations a velocity field $v_y=0$ is specified from a radius of 80 mm until the outside of the blank (100 mm). As draw-in continues the velocity field reaches the die corner radius. At this point the blank holder pressure is high enough to prevent separation and the velocity field is removed. The CPU time for the VAX simulation is 129 hours and for the HP simulation it is 82 hours.

Results and comparison

The load-stroke diagram for the two DEFORM simulations and the ABAQUS simulation is shown in Fig 3.8. For both of the DEFORM simulations, the load is higher than the load predicted by ABAQUS. This is not necessarily wrong. According to Romanowski [1959], the maximum punch load is about 106,000 N when using Equation (3.5). One may conclude that both of the DEFORM simulations provide realistic values for the load-stroke diagram.

$$F_p = K_1\, 2\pi\, r_p\, t_0\, \sigma_b \qquad (3.5)$$

Where:

K_1 = constant, to be found in Fig. 3.9
r_p = punch radius [mm]
t_0 = initial sheet thickness [mm]
σ_b = flow stress, calculated as in Equation (3.6)

$$\sigma_b = C\, n^n\, e^{(\varepsilon_0 - n)} = 374.3 \quad [N/mm^2] \qquad (3.6)$$

Wall-thickness variation

The knowledge of the geometry, especially that of the wall thickness variation is important for the successful planning of forming operations like reverse

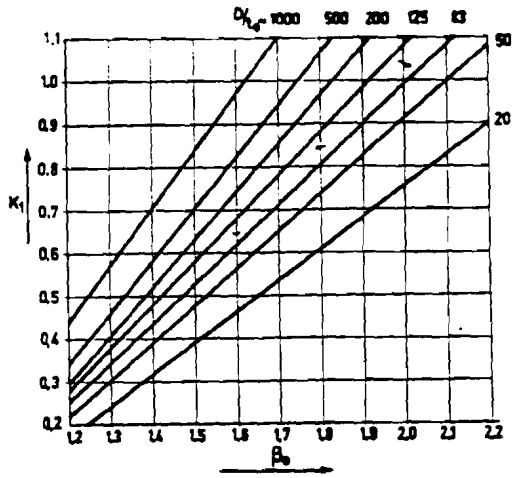

Fig. 3.9 Determination of K_1 (used in Equation 3.5) according to Johnson, [1986], where β_0 = drawing ratio, D is blank diameter and t_0 is initial thickness

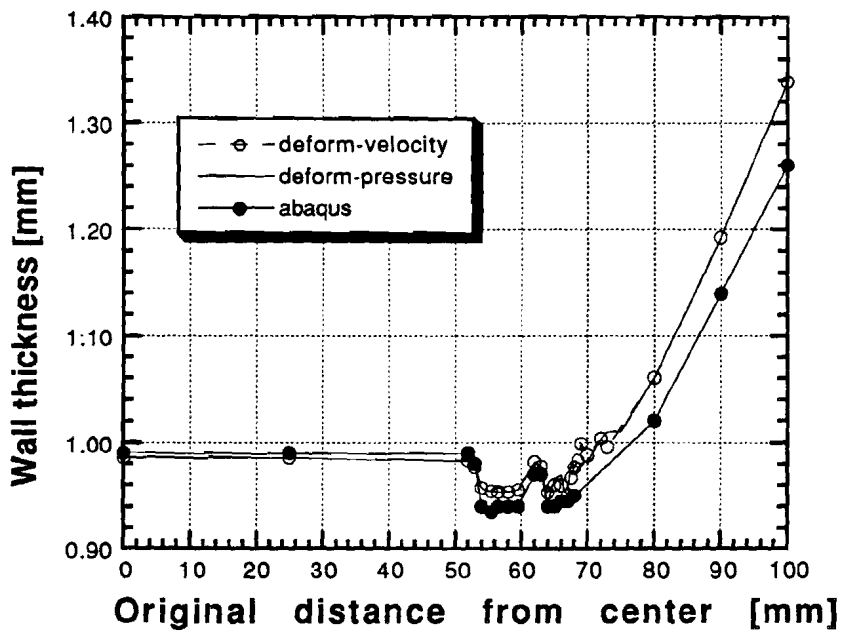

Fig 3.10 Wall thickness variation curve for DEFORM and ABAQUS simulations

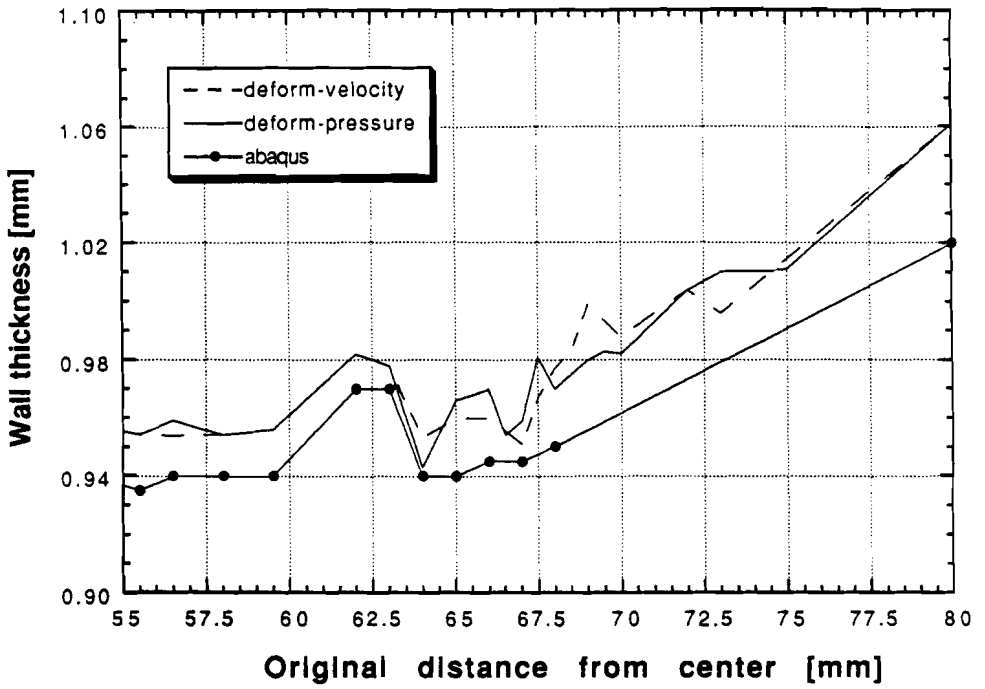

Fig 3.11 Magnified plot of the necking zone at punch nose

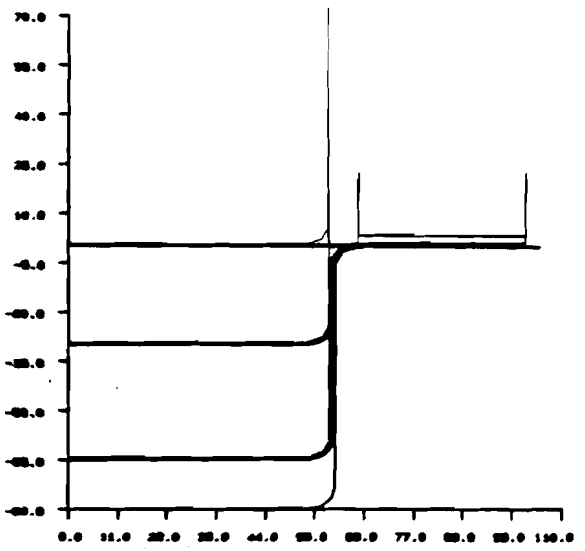

Fig. 3.12 Deformed sheet for deep drawing simulation using DEFORM at a punch stroke of 0, 20 and 40 mm.

Since the friction coefficient in the blank holder/blank interface and the blank/die interface was unknown, several values of μ were used in the SHEET_FORM simulations in order to determine the friction coefficient which gives the best agreement with the experiment. The best agreement was found for a Coulomb friction coefficient of 0.13. Therefore this value is also used in the DEFORM simulation. The tool geometry of the process is shown in Table 3.3 using the symbols as in Fig. 2.3. The material used is HSG steel, High Strength Galvanized steel. The material properties are (in the Ludwik-Hollomon equation ($\sigma = K(\varepsilon+\varepsilon_0)^n$)) specified in Table 3.3.

Table 3.3 Tool geometry and process parameters as used in comparison of DEFORM with experiment using HSG steel, symbols as in Fig. 2.3

Strength coefficient K	=	603.8	[N/mm^2]
Strain hardening exponent n	=	0.143	[-]
Pre-strain ε_0	=	0.000328	[-]
Normal anisotropy factor R	=	1.4	[-]
Punch radius (R_p)	=	76.2	m m
Punch corner radius (r_p)	=	20.07	m m
Die radius (R_d)	=	79.12	m m
Die corner radius (r_d)	=	16.00	m m
Blank radius (R)	=	127	m m
Blank thickness (t)	=	0.889	m m
Blank holder force	=	117	kN
Friction coefficient μ(die and sheet)	=	0.13	[-]
Friction coefficient μ (punch and sheet)	=	0.13	[-]
Stroke	=	60.0	m m

Mesh and simulation conditions in DEFORM

A uniform mesh of 2436 elements is generated in DEFORM, with four layers in thickness direction, and thus, 609 in radial direction for each layer. A pressure of 2.5 MPa (total force because of the pressure is 12566 N) is applied under the punch until a radius of 40 mm, to prevent separation from the punch. The force generated by this pressure will be subtracted in the load-stroke diagram, to eliminate its influence on the load-stroke diagram. At the die interface, a

velocity field with v_y = 0 mm/s is specified for the nodes from a radius of 105 mm until 127 mm to prevent separation. When the draw-in of the flange has proceeded so far that these nodes reach the die corner radius, the simulation is stopped and the velocity field is removed. Then the simulation is restarted. At this stage, the BHF generates a pressure which is high enough to prevent separation in this interface without having specified a velocity field under the blank holder interface.

Results and comparison

In Fig. 3.13 the radial strain is presented, for both the experiment and the DEFORM simulation at a punch stroke of 60 mm. Since the strain is measured with the circle grid method at the outer surface of the cup, in DEFORM the strain is also determined at the outer surface of the cup. Fig. 3.14 presents the load-stroke diagram for both the experiment and the DEFORM results. The agreement between DEFORM and the experiment is good. The peaks and drops in the experimental value are probably due to inaccurate strain measurements. The general trends match each other quite well, as do the load-stroke diagrams.

3.3 Plane - strain stretch forming (Benchmark test)

"Stretch forming is a method that combines controlled stretching and bending of sheet metal blanks, roll-formed sections, and extrusions around form blocks (dies) to produce accurately contoured parts without wrinkles", TMEH, [1984]. In stretch forming, the material in the flange does not move, it is clamped. So there is no sliding of this material around the die corner radius, but the material is stretched. The radial strain distribution in stretching is quite uniform, so each part of the original blank is stretched and thus strengthened and has an increased hardness because of the work-hardening.

Problem statement

In the Benchmark test (3.2.1) stretch forming was simulated, using plane-strain and axisymmetric geometries. Fig 3.1 shows the plane-strain geometry where the nodes from a radius of 59.18 mm until the edge of the sheet have zero displacement in radial direction.

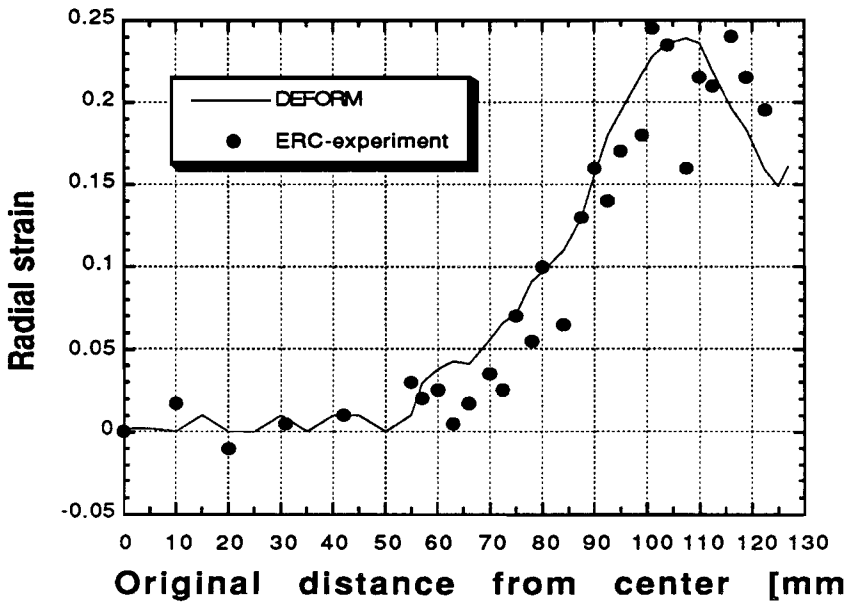

Fig. 3.13 Radial strain distribution for deep drawing of HSG steel for both experimental and DEFORM results at a stroke of 60 mm

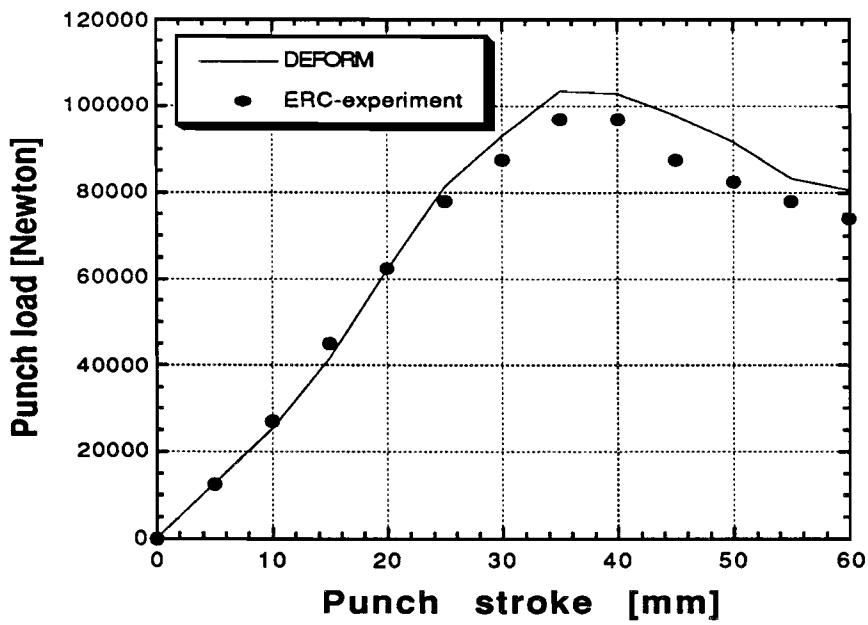

Fig 3.14 Load-stroke diagram both experiment and DEFORM

The material properties are given in section 3.2.1.

Simulation and mesh in DEFORM

The mesh consists of 1240 elements, four elements in thickness direction and thus 310 in radial direction. At the punch nose a pressure of 4.5 MPa is applied to prevent separation. At 35 mm punch travel necking occurred at the die corner radius. Some participants of the Benchmark test had the same problem, as shown in Table 3.4. This simulation converged faster, because of the boundary condition, which prohibits sliding and thus the contact changes are less frequent and the contact condition is more stable than in deep drawing.

Table 3.4 Researchers and their codes compared with DEFORM

Name/employee	FEM code	Stroke (max)	Computer	CPU (s)
Besdo/Uni Hannover	FEMSY, EP	30	CDC180	262
Lee/RPI	SUPER, EP	40 *	Micro VAX	1560
Doege/Univ. Hannover	ABAQUS 4.6 EP	30	CDC 180	534
Heimerdinger/DB	ABAQUS, EP,	30	CRAY	502
Nagtegaal/Hibbitt	ABAQUS 4.7 EP	40	VAX 8800	149
Logan/L. Livermore	SQUIRREL, RVP	40 *	IBM 386	45
KeumWang/ OSU	STRIP	40 *	CRAY	430
Wenner/GMRL	Lineform, EP	40 *	IBM 3090	9
Yang/Kaist	?, EP	32	SUN3/110	85
Lee,Choudry/OSU	Sheet-B, RVP	30	VAX 8550	200
Guerra/Los Alomos	NIKE2D, EP	?	?	?
Tang/VW Gedas	Tiefsim, EP	33	CRAY	13
FLower/L livermore	NIKE2D, EP	40 *	CRAY	21
ERC/NSM	DEFORM	35	HP700s	20 hr

RVP = Rigid Visco Plastic, EP = Elastic Plastic, RP = Rigid Plastic, Lee et al., [1990]
'*' indicates that the result is not within the specified range used to compare with DEFORM

Results and comparison

Obviously there are difficulties among several codes to reach the required punch stroke of 40 mm and within the specified range because necking starts. When necking starts, most of the deformation is concentrated in the necking area. The strain distribution is similar for a punch stroke of 32.5 and 35 mm (in DEFORM), except that the peak in the necking area (near the die corner radius) is higher for a stroke of 35 mm. Figures 3.15 and 3.16 show the radial strain distributions for a punch stroke of 20 mm and 35 mm respectively. The solid lines represent the range of reasonable results from the Benchmark test and the crosses are DEFORM results. This was the maximum stroke which DEFORM could reach because of the necking that occurred. Fig. 3.17 shows the load-stroke diagram for DEFORM and the Benchmark test results. As seen, the agreement is reasonable and the results regarding the radial strain distribution and load-stroke diagram, generated by DEFORM can be considered as being realistic and reliable. The deformed sheet is shown in Fig. 3.18 for punch travels of 0, 20 and 32.5 mm.

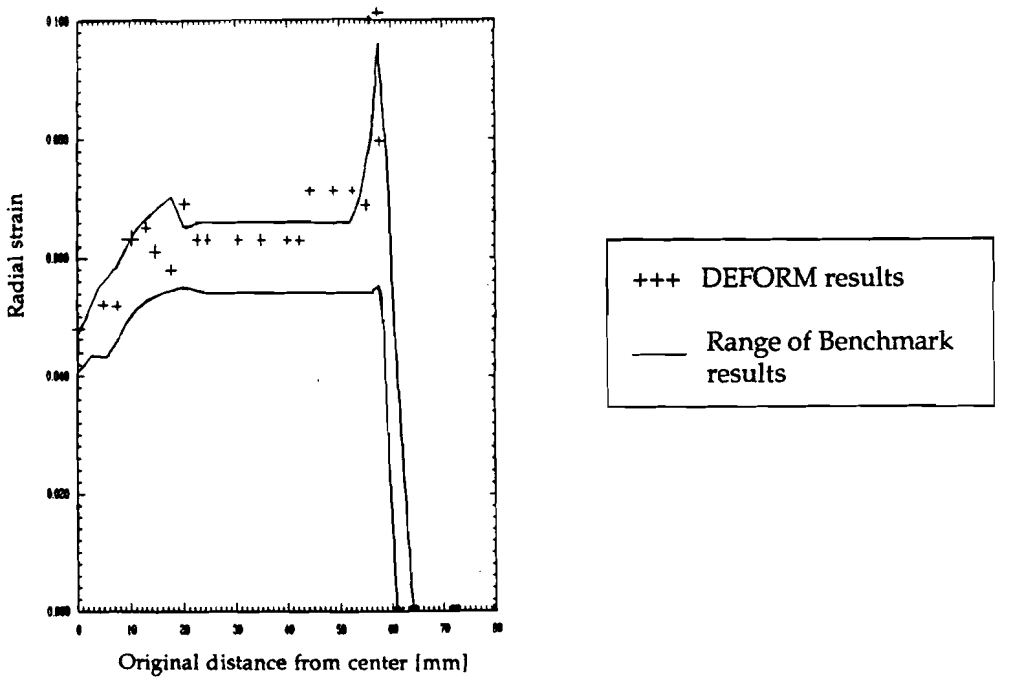

Fig. 3.15 Radial strain distribution for both DEFORM and Benchmark test results at a punch stroke of 20 mm

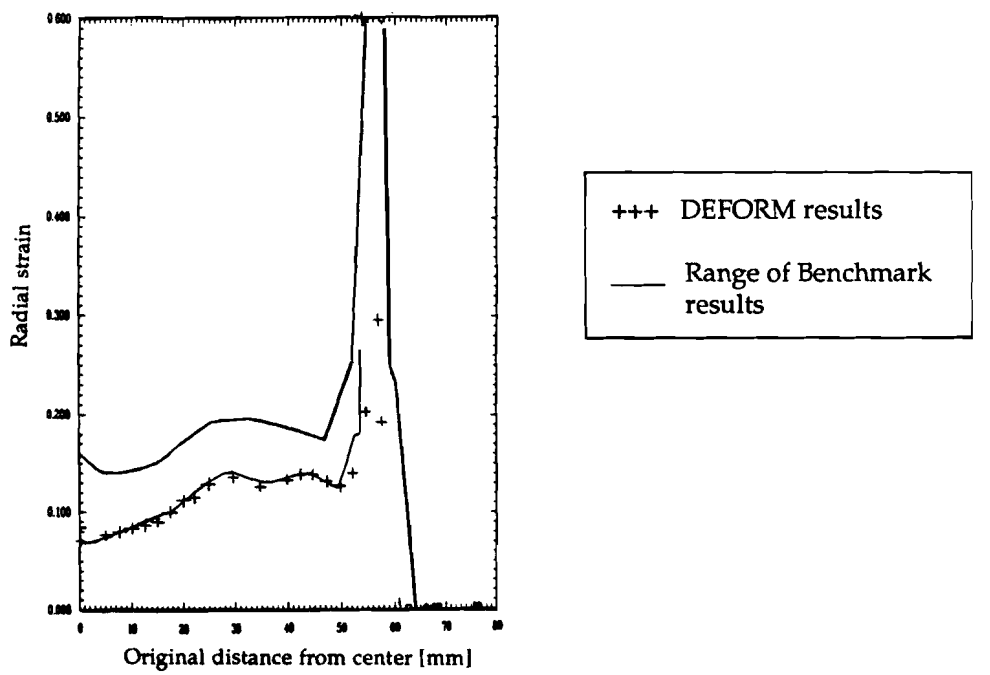

Fig. 3.16 Radial strain distribution for both DEFORM and Benchmark test results at a punch stroke of 35 mm

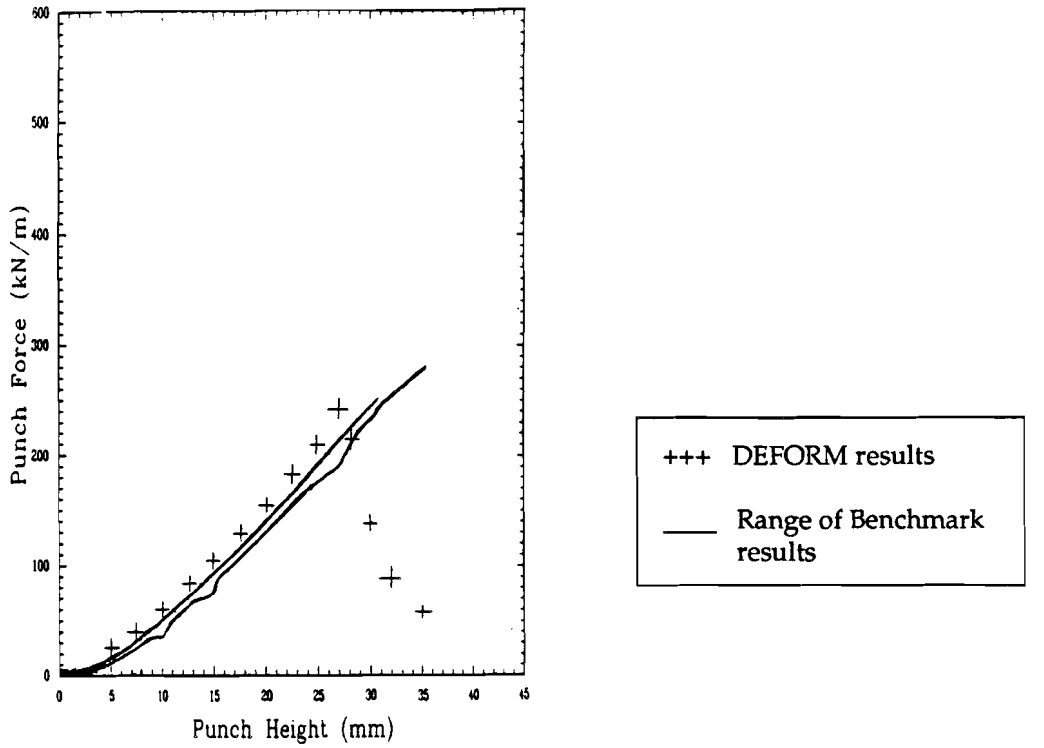

Fig. 3.17 Load-stroke diagram for DEFORM and Benchmark test results,

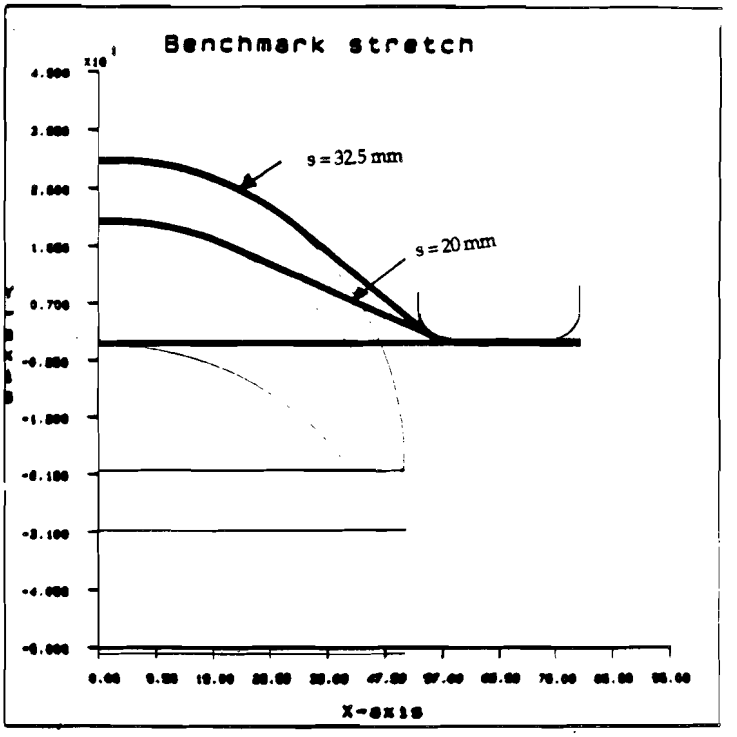

Fig. 3.18 Deformed sheet geometry obtained from DEFORM simulation at punch strokes of 0, 20, and 32.5 mm

CHAPTER IV

INFLUENCE OF GEOMETRY ON BENDING

The main objectives of this chapter are:

a) Investigate the influence of the ratio of the die corner radius, r_d, to the sheet thickness, t, (r_d/t) on the strain distribution.

b) Compare the results of the modified membrane code (including bending correction on strains) with DEFORM.

c) Determine a minimum value for the r_d/t ratio for which bending effects can be neglected and strain distributions can be predicted with reasonable accuracy using the membrane formulation.

4.1 Fundamentals of bending effects

The detailed analysis and discussions on bending effects and bending corrections for membrane model were given by Wang et al., [1992].

Two most important parameters affecting the importance and amount of bending effects are:

1) The r_d/t ratio
2) The BHF or draw bead force (DBF)

The effects of these parameters on the bending strains are briefly discussed below. The bending effects are different in three different areas of a formed cup. These three areas are shown in Fig. 4.1. In the following section, each area is discussed briefly.

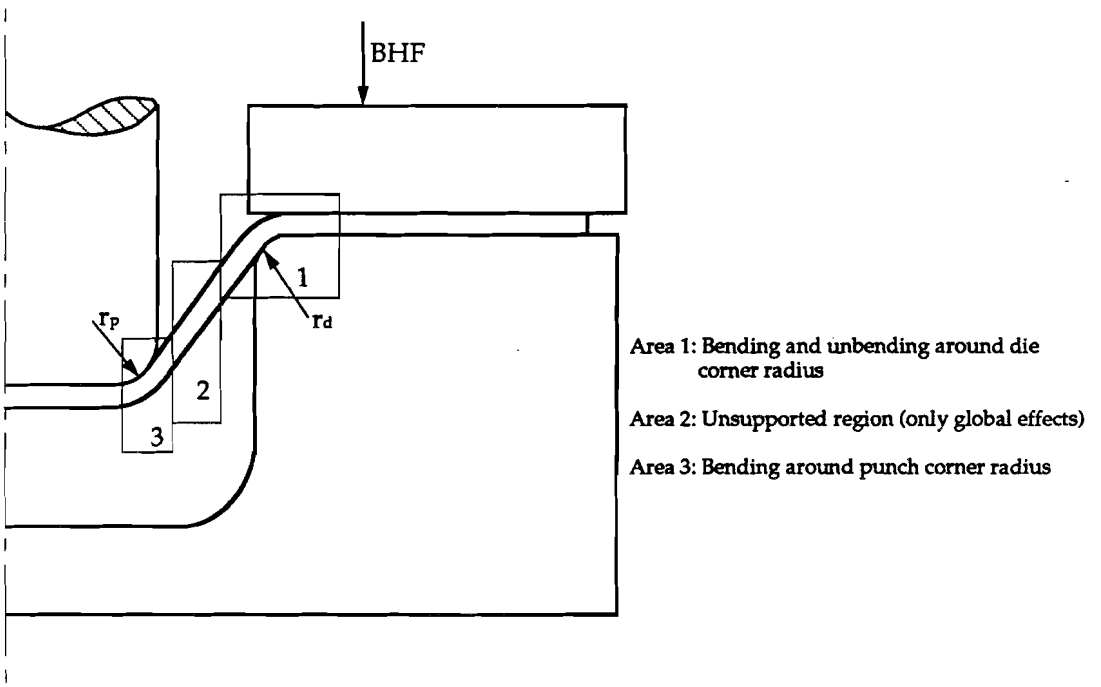

Fig. 4.1 Different areas in which local and global bending effects occur

Area 1: Bending around the die corner radius:

In a deep drawing operation, metal flows into the die cavity due to the punch travel and the part of the sheet which is originally located under the blank holder undergoes three different types of deformation as draw-in continues. These are:

1) bending around the die corner radius
2) sliding over the die corner radius in area 1 of Fig. 4.1
3) unbending when the sheet passes the die corner radius and enters area 2 of Fig. 4.1

Bending around the die corner radius results in two different contributions to the strain distribution. These are:

1) local variations due to the bending strain relative to the neutral plane.
2) global variations affecting the overall strain level due to additional stress and work that is required to stretch or compress the fibers to different curvatures if the sheet is pulled into or out of a bend. This additional stress is a function of the material properties, friction, current stress level and the r_d/t ratio. In the unsupported region, the strain is influenced by the global effects as sliding and unbending occurs. Due to the strain hardening, the in-plane tension force increases. When the r_d/t ratio drops below 5, this global effect increases rapidly.

Area 2: The unsupported region between the punch and the die

Due to the tension (restraining force) generated by the BHF or DBF, overall membrane strains are generated. In this area only global effects occur. The portion of the sheet that is bent over the die corner radius and slided into area 2 where it is unbent, shows an increased effective and radial strain.

Area 3: Bending around the punch corner radius

Draw-in continues along all directions if the punch is not symmetric. Then, the three deformation processes (bending, sliding and unbending) affect the portion of the sheet that initially is located under the punch. However, if the punch is symmetric the sheet located at the symmetric center will not have in-plane

motion and the sliding and unbending over the punch radius is relatively small. Then, only local bending around the punch radius is significant.

4.1.1 Analysis of pure bending strain

Under plane-strain conditions, the pure bending strain is easily calculated when the restraining force is not considered. The neutral plane is assumed to be the same as the mid-plane and the thickness, t, is assumed to be constant (no sheet thinning). The portion of the sheet subjected to bending is shown in Fig. 4.2. This local bending strain occurs both at the punch corner radius and the die corner radius.

The bending strain ε_b is calculated according to Equation 4.1, [Wang, 1992].

$$\varepsilon_b = \ln(\frac{l}{l_0}) = \ln\left(\frac{(r_d + y + t/2)\varphi}{(r_d + t/2)\varphi}\right) = \ln(1 + y/R_m) \tag{4.1}$$

Then the maximum bending strain at the outer side of the sheet is:

$$(\varepsilon_b)_{max} = \ln\left(1 \pm \frac{t}{2R_m}\right) \tag{4.2}$$

Where '+' is for convex surfaces and '-' is for concave surfaces. For a large corner radius, r_d, Equation (4.2) is rewritten as $\varepsilon_{b,max} = \pm t/2r_d$. This bending strain along the thickness direction for elastic bending is shown in Fig. 4.3. When the material starts yielding, the bending strains are not linear anymore in the sheet thickness direction due to strain hardening.

According to Equation 4.2, the bending strain increases asymptotically with a decrease in r_d and linearly with an increase in thickness t. For r_d/t ratios below 5 the strain will increase rapidly.

4.1.2 Shift of the neutral axis in plane strain

The BHF and drawbead force (DBF) determine the level of the overall membrane strain in the sheet. If there is no friction at the punch/die interface the membrane strain is uniform.

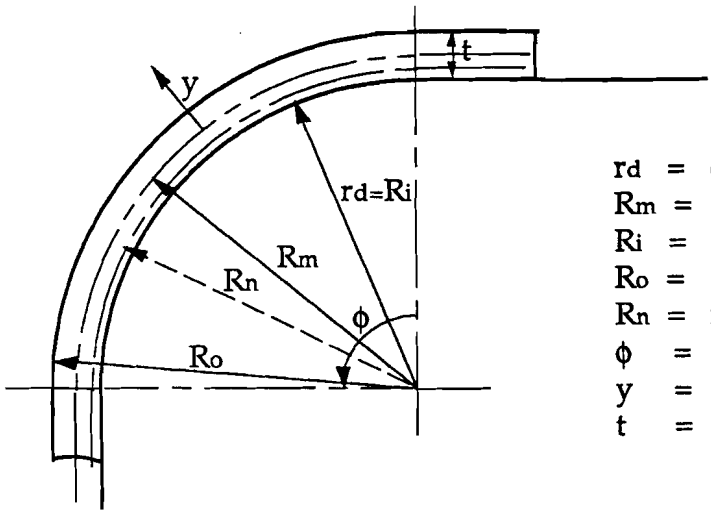

rd = die corner radius
Rm = radius to mid-plane
Ri = inner radius of sheet
Ro = outer radius of sheet
Rn = radius of neutral axis
ϕ = bending angle
y = distance in radial direction from Rm
t = current sheet thickness

Fig. 4.2 Symbols used in determination of the pure bending strain in a sheet

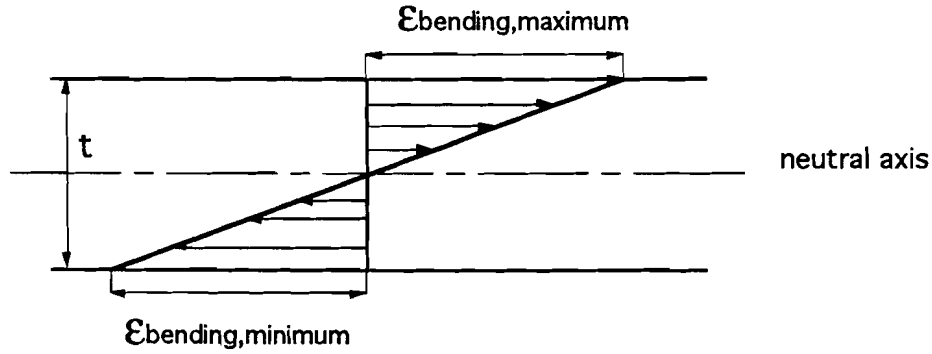

Fig 4.3 Elastic bending strain in sheet across the thickness (thickness t) if there is no shift of the neutral axis

The shift of the neutral axis when bending under tension is generated by the BHF and/or DBF is due to (a) local contact pressure built up when bending over a small radius and (b) the thinning of the sheet.

It is necessary to find the actual position of the axis to evaluate the bending effects on the strain distribution. For high restraining forces, stretching may dominate the deformation. In stretching or deep drawing with a high BHF, sheet thinning (thus shift of the neutral axis) is more significant than sliding and unbending, and it is the major cause of the shift in the neutral axis. As thinning starts, the neutral axis shifts towards the concave surface and it may be totally out of the sheet. The shift in the neutral axis causes higher bending strains at the convex surface of the sheet because of the decrease in the effective bending radius, i.e., the radius of the neutral axis. For deep drawing with a low BHF the influence of sliding and unbending increases while the effect of the sheet thinning decreases. On the basis of volume conservation, the shift of the neutral axis is calculated by Equation (4.3). The derivation of Equation (4.3) is shown in Appendix B.

Radius of the neutral axis R_n (symbols shown in Fig. 4.2):

$$R_n = \frac{R_i + R_0}{2}\frac{t}{t_0} = R_m \frac{t}{t_0} \tag{4.3}$$

Then the shift distance d of the neutral axis is as in Equation (4.4):

$$d = R_m - R_n = R_m(1-\frac{t}{t_0}) = (R_i + \frac{t_0}{2}e^{-\varepsilon_{membrane}})(1-e^{-\varepsilon_{membrane}}) \tag{4.4}$$

Where

d	=	shift distance of the neutral axis
t	=	current thickness (Equation (4.7))
R_i	=	inner radius of sheet, or die corner radius r_d
R_0	=	outer radius of sheet
R_m	=	radius of middle axis

Equation (4.4) shows that thinning causes the shift, if bending and tension coexists. The maximum bending strain occurs at the convex surface of the sheet and is calculated by Equation (4.5):

$$\varepsilon_{convex} = \ln[\frac{R_o}{R_n}] = \varepsilon_{membrane} + \varepsilon_{bending,maximum} = \varepsilon_{membrane} + \ln(1+\frac{t}{2R_m}) \tag{4.5}$$

And the minimum bending strain because of the shift at the concave surface is, [Wang, 1992]:

$$\varepsilon_{concave} = \ln[\frac{R_o}{R_n}] = \varepsilon_{membrane} + \varepsilon_{bending,minimum} = \varepsilon_{membrane} + \ln(1 - \frac{t}{2R_m}) \qquad (4.6)$$

By assuming volume constancy in the membrane approach, the thickness t, as in Equations (4.4), (4.5) and (4.6) is approximately determined. Equation (4.7) is derived in Appendix B.

$$t = t_0 e^{-\varepsilon_{membrane}} \qquad (4.7)$$

After the determination of the maximum and minimum strain according to Equations. (4.5), (4.6) and (4.7), the modified strain at the mid-axis is estimated as the average of the strains along the thickness:

$$\varepsilon_{average} = \xi_1 . \varepsilon_{maximum} + \xi_2 . \varepsilon_{minimum} \qquad (4.8)$$

ξ_1 and ξ_2 are weigh factors depending on the distance of the outer and inner surfaces from the neutral axis. In Equations. (4.9a) and (4.9b) they are expressed as a function of the shift distance:

$$\xi_1 = \frac{1}{2} + \frac{d}{R_m} \qquad (4.9a)$$

$$\xi_2 = \frac{1}{2} - \frac{d}{R_m} \qquad (4.9b)$$

Where d/R_m is defined as in Equation (4.4)

The purpose of calculating the average strain as in Equation (4.9a and b) is to take into account the shift of the neutral axis on the axial stress level. Now, the stress is as in Equation (4.10).

$$\bar{\sigma}_{average} = K(\bar{\varepsilon}_{average})^n \qquad (4.10)$$

Once the shift distance of the neutral axis is known, the maximum, average, and minimum bending strain can be calculated.

4.1.3 Global bending effects: Sliding and Unbending

Due to global effects, the stresses and draw force changes, and the strain hardening history must be taken into account for a proper model description. If a sheet is already bent over the die radius it is further subjected to successively sliding and unbending when draw-in continues. The differential equation for moment equilibrium about the center of the bent is as in Equation (4.11) , the active forces and moments are shown in Fig. 4.4:

$$(T + dT)R_m + (M + dM) - M - T.R_m - F.r_d = 0 \qquad (4.11)$$

Where:

T	=	tensile force
M	=	moment
F	=	friction force
R_m	=	radius of middle axis
r_d	=	die corner radius

The solution of this differential equation is derived in Appendix C, and shown in Equation 4.12, [Wang, 1992]:

$$T_s = T_b.e^{\mu\phi_0\frac{r_d}{R_m}} - \frac{2}{1+e^{-\mu(\phi_0-\phi)\frac{r_d}{R_m}}}\frac{M_s - M_b}{R_m} \qquad (4.12)$$

Where T_b and M_b are the force and bending moment respectively at the beginning (inlet) of bending, and T_s and M_s are force and the moment respectively at the end (outlet) of bending. T_b is calculated by: $T_b = 2\mu.BHF$. Note that in plane-strain cases the BHF is mostly defined as force per unit in width direction. This must be taken into account when applying global bending correction.

The wrapping angle varies from $\phi = 0$ (at the inlet of the bend) to $\phi = \phi_0$(at outlet of the bend, the total sliding angle). The value of ϕ_0 depends on the clearance between the die and the punch radius (R_d-R_p) and the punch travel. For ideal lubrication ($\mu = 0$), the force increase is as in Equation (4.13):

$$T_s = T_b - \frac{M_s - M_b}{R_m} \qquad (4.13)$$

The sheet is unbent to a straight line (unsupported region) by the reverse bending moment. Then, the sign of the unbending moment M_s is opposite, but the magnitude equals M_b. Thus, Equation (4.12) and (4.13) are rewritten as in Equation (4.14) and (4.15), and M_b is shown in Equation (4.16), [Wang, 1992]:

$$T_s = T_b.e^{\mu\phi_0\frac{r_d}{R_m}} + \frac{4}{1+e^{-\mu(\phi_0-\phi)\frac{r_d}{R_m}}}\frac{M_b}{R_m} \qquad (4.14)$$

$$T_s = T_b + \frac{2M_b}{R_m} = T_b + \frac{4M_b}{(2r_d/t+1)t} \qquad (4.15)$$

$$M_b = \frac{2}{3}R_n^2E'\varepsilon_o^3 + KF^{n+1}R_n^2\left\{\frac{1}{n+2}\left[\varepsilon_{max}^{n+2} - 2\varepsilon_0^{n+2} + \varepsilon_i^{n+2}\right] + \frac{3}{2(n+3)}\left[\varepsilon_{max}^{n+3} + \varepsilon_i^{n+3}\right]\right\} \qquad (4.16)$$

Where M_b is bending moment, derived in Appendix C , and shown in eqn (4.16)

$R_m = r_d + t/2$,

$t = t_0e^{-\varepsilon_{mem}}$ (as in Equation (4.7))

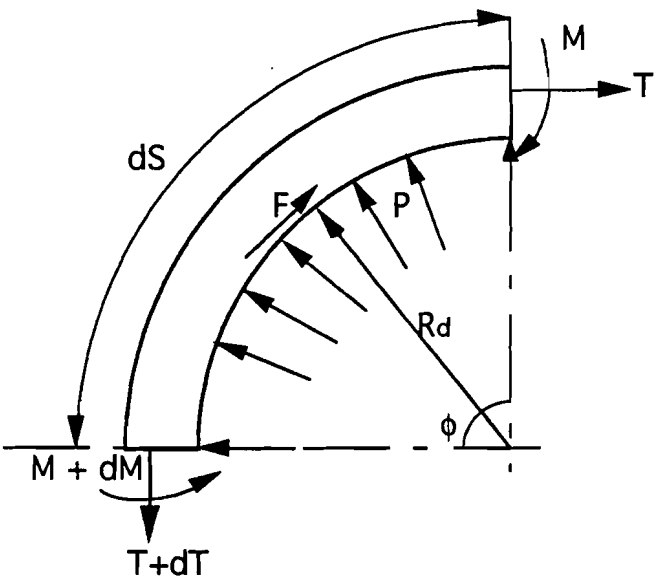

Fig. 4.4 Forces and moments acting on a sheet which is bent around the die corner radius r_d

From Equation (4.14), it is concluded that:

a) T_s increases exponentially with a decrease of r_d/t ratio
b) Draw force increases linearly with bending/unbending moment
c) Draw force increases linearly with restraining force T_b
d) Draw force increases exponentially with friction coefficient and bending/sliding angle

4.2 Simulations with different r_d/t ratios

Simulations are performed using DEFORM with different r_d/t ratios to investigate the bending effects more thoroughly. The geometry parameters are shown in Table 4.1.

Table 4.1 Process parameters as used in axisymmetric simulations

Name in graphs	r_d [mm]	r_d/t [-]	t [mm]	R_d [mm]	R_p [mm]	r_p [mm]	R [mm]	μ	BHF [kN]
AX 18	16	18	0.889	79.12	76.2	20	127	0.13	117
AX 9	8	9	0.889	79.12	76.2	20	127	0.13	117
AX 5	4.45	5	0.889	79.12	76.2	20	127	0.13	117

High strength steel (HSG) is used in the simulations (the same as in the ERC experiments). The parameters of the steel as well as the tool geometry for AX18 are given in section 3.2.3, in Table 3.3. In the other two simulations, (AX9 and AX5) only the die corner radius is decreased to show its influence on the strain distribution and the amount of bending. A velocity field of $v_y = 0$ is specified, as in Chapter 3, in the blank/die interface to reduce separation problems. A pressure of 2.5 MPa is applied under the punch nose to reduce separation and to stabilize the contact condition. The force generated by the pressure is 12,500 N and is subtracted in all the load-stroke diagrams to eliminate its influence. The influence of the specified pressure on the strain distribution is very small, since there is no sliding of the material at the punch nose when using a symmetric punch. Four elements are defined in thickness direction, and the total number of elements is 2500.

4.3 Results for axisymmetric deep drawing

The results from these three simulations such as radial, thickness, and effective strains are shown. The local bending effects (pure bending strain), the shift of the neutral axis, and the global effects (overall strains increase due to sliding and unbending) are examined to observe the influence of the r_d/t ratio on them.

4.3.1 Local bending effects

The local bending effects occur only in the areas 1 and 3 (from Fig. 4.1) where the sheet is bent over the die and punch corner radius. Figures 4.5, 4.6, and 4.7 show the radial strain distributions at a punch travel of 45 mm for AX18, AX9, and AX5 respectively.

Fig. 4.5 shows that for a ratio of $r_d/t = 18$ (AX18), the peaks in the inner and outer layers are close to the strains in the middle layer, the difference is about 2 to 3%. Due to the large ratio, the strain due to bending is negligible. When the ratio decreases to 9, the peaks increase as shown in Fig. 4.6 and the difference increases between 4 to 7%. In Fig 4.7 the ratio is 5, and the peaks at the outer and inner layers are significantly different (8 to 11%) than the middle layer strains due to the high bending strain.

For all the three simulations, the radial strain at the edge of the blank is the same for the three layers, because this part of the sheet is not bent yet and is still part of the flange at the punch travel of 45 mm. As the punch travel increases, the strain distribution will not be the same anymore at the three layers. However there were difficulties to reach larger punch travels with DEFORM, especially for AX5. Therefore the results are shown only at a punch travel of 45 mm.

For decreasing ratios the amount of local bending strain increases fast. The differences between the strains at the inner and middle layers ($\varepsilon_{inner} - \varepsilon_{middle}$) and between the strains at the outer and middle layers ($\varepsilon_{outer} - \varepsilon_{middle}$) over the die corner radius give a indication of the local bending strain and the shift of the neutral axis. The bending strain in the outer layer is: ($\varepsilon_{outer} - \varepsilon_{middle}$), if it is assumed that the middle layer strain (from DEFORM) equals the membrane strain.

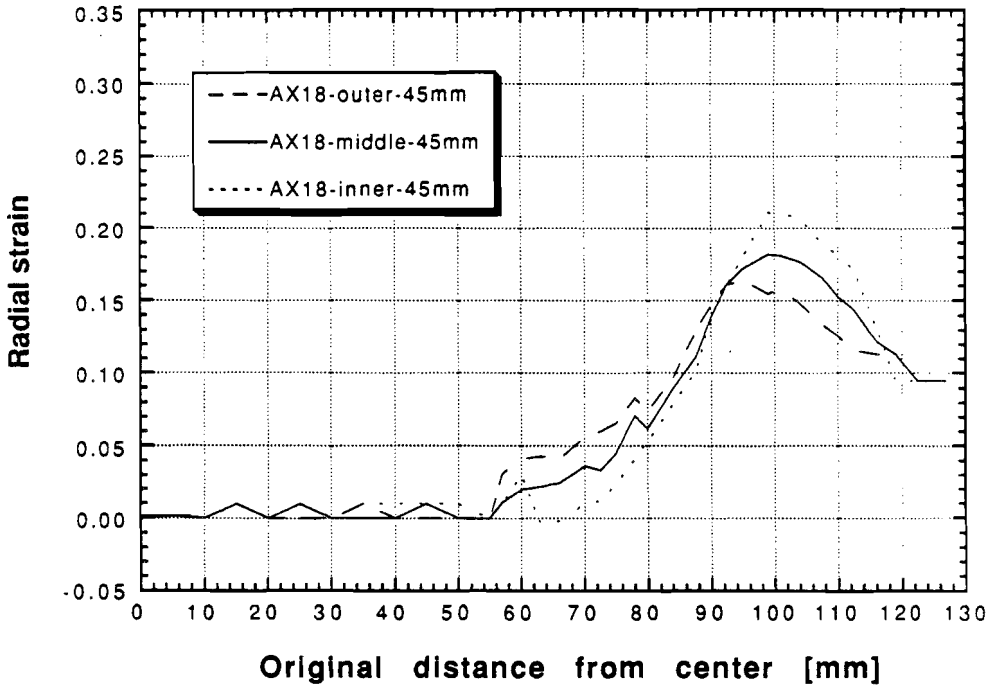

Fig. 4.5 Radial strain distribution for AX18 at a punch travel of 45 mm

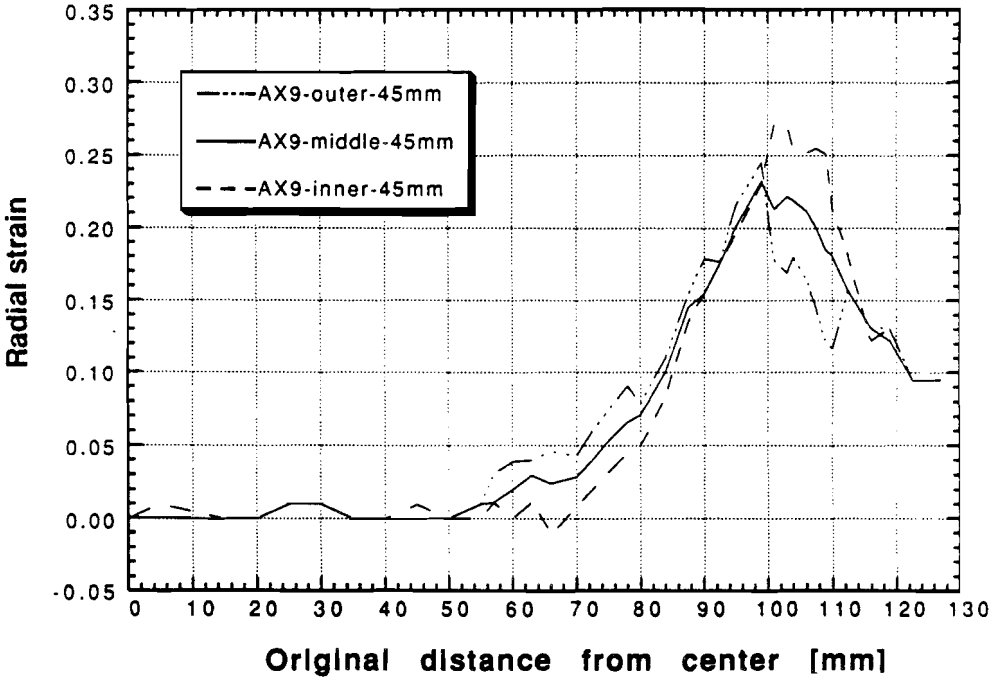

Fig. 4.6 Radial strain distribution for AX9 at a punch travel of 45 mm

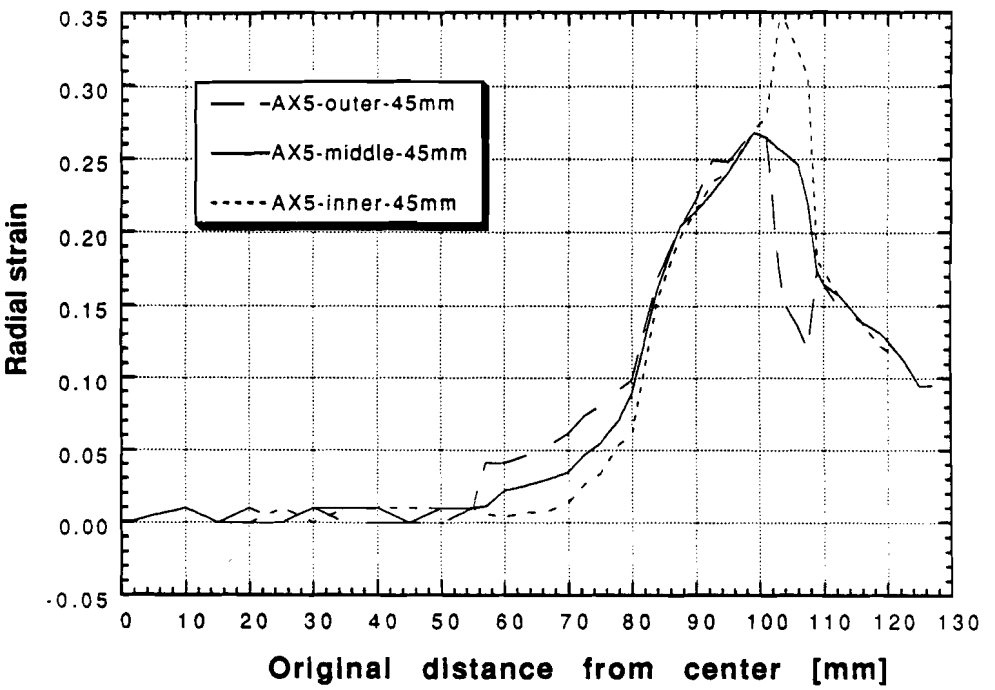

Fig. 4.7 Radial strain distribution for AX5 at a punch travel of 45 mm

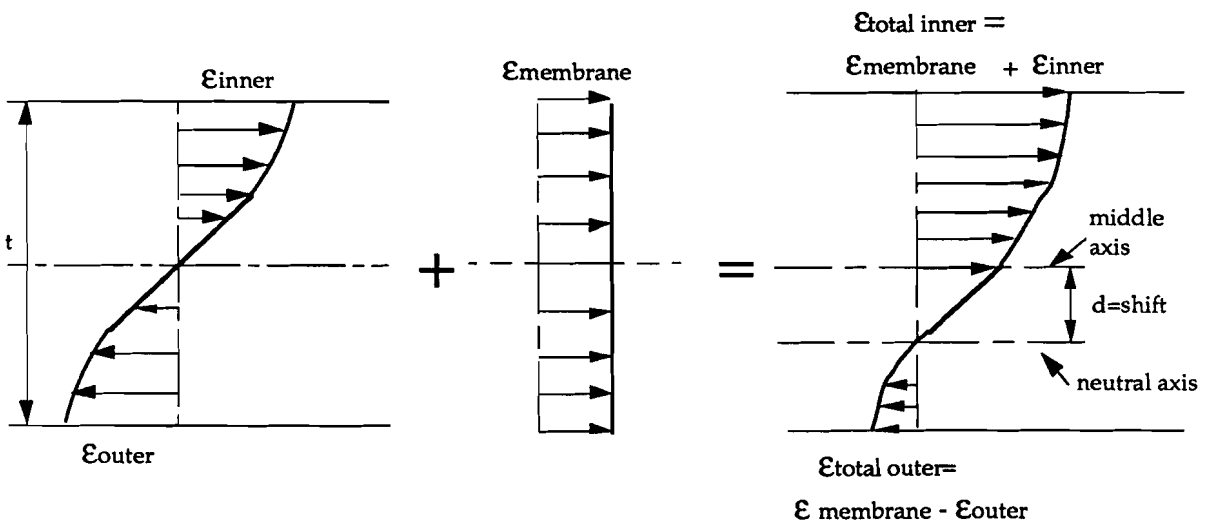

bending strain + membrane strain = total strain

Fig 4.8a Influence of the shift of neutral axis on the strain distribution

The bending strain in the inner layer is similarly calculated: (ε_{inner} - ε_{middle}). Note that the theoretical value from Equation (4.2) is valid for plane-strain bending instead of axisymmetric. In order to give an approximation of the bending strain, Equation (4.2) is used. Figure 4.8a shows the superposition of elastic-plastic bending strain and membrane strain (due to tension) for bending under tension over a radius. Then the two strains at the convex and concave surfaces are not equal, since the membrane strain is added to the pure bending strain. If parts of the sheet deform plastically they are subjected to non-linear strain hardening. Table 4.2 and Fig. 4.8b show the local bending strains from DEFORM together with the theoretically calculated bending strain (using Equation 4.2).

Table 4.2 Maximum local bending strain ε_b at die corner radius from DEFORM compared with plane-strain theory (Equation 4.2)

	$\varepsilon_{outer,DEFORM}$	$\varepsilon_{outer,theory}$	$\varepsilon_{inner,DEFORM}$	$\varepsilon_{inner,theory}$
AX18	-2.5	-2.74	1.8	2.67
AX9	-5.7	-5.37	7	5.1
AX5	-8	-10.5	10.5	9.5

The trend of the bending strain distributions along the material points subjected to bending over the die corner radius agrees well with the theoretical values from Table 4.2. However, for AX9 and AX5 there are some points that are considerably out of the range. Note that the theoretical strain does not consider a shift of the neutral axis towards the convex curvature. As written in section 3.2, the point tracking method is used in DEFORM for the calculation of the radial strain. Using the point tracking method, the shift due to sheet thinning is included in the strain calculation by defining two nearby points, which are originally located at the middle axis. These points will remain in the middle axis as sheet thinning occurs. However, the shift due to the applied tension and contact pressure is not considered. In the next part the shift of the neutral axis is further investigated. Figure 4.8b shows that the local bending strain increases rapidly when the ratio drops from 9 to 5. The bending strain increases from about 5% for AX0 to 10% for AX5. Relatively these increases are much higher, 20% to 30%. Figure 4.8b also shows that when the die corner radius decreases,

the portion of the sheet subjected to bending decreases, since the contact area is linear dependent on the radius ($r_d \phi$ is arc length of contact area).

4.3.2 The shift of the neutral axis:

A shift of the neutral axis occurs, because of (a) the axial tension generated by the BHF and/or DBF builds up the local contact pressure when the sheet is bent over the die corner radius, and (b) thinning of the sheet. The shift of the neutral axis affects the strains in the whole sheet as shown in Fig. 4.8a. For high membrane strains, the neutral axis can even be out of the sheet, and the radial strains at the outer surface are positive. This effect is shown in Fig. 4.5, 4.6, and 4.7. For all of the three r_d/t ratios, the radial outer and inner surface strains are positive, due to the tensile force. For stretch forming, the shift of the neutral axis is expected to be even higher, (due to higher restraining force) while the amount of sliding and unbending decreases (due to higher BHF and/or DBF).

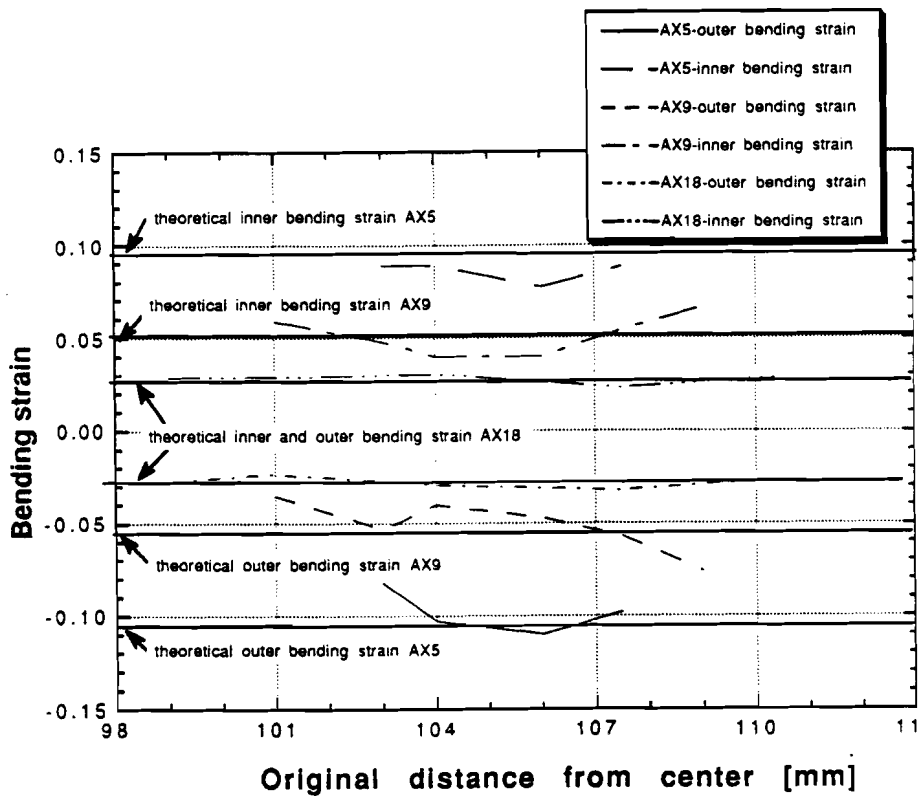

Fig. 4.8b Local bending strain from simulations and theory at a stroke of 45 mm

Comparison of DEFORM with Plane-Strain Theory

According to Equation (4.4), the shift depends on the amount of membrane strain. For the three axisymmetric simulations, the shift is calculated and the assumption is made that Equation (4.4) is also valid for axisymmetric cases, since there is no theoretical model for axisymmetric cases. Equations 4.5 and 4.6 are used to calculate the minimum and maximum surface strains. The middle layer strain at the peaks is taken as membrane strain to calculate the current thickness (Eqn. 4.7). In Table 4.3 the maximum and minimum strains are listed for both DEFORM and the theory, as well as the theoretical relative shift distance d/R_m. The maximum strains for the theory (using middle layer strain of DEFORM) and DEFORM agree well. However, the minimum strains calculated with the theory are higher than predicted by DEFORM.

Table 4.3 Shift of the neutral axis, maximum and minimum strains for 3 r_d/t ratios, both theoretical and DEFORM predictions

	$\varepsilon_{mid,max}$	t(eqn. 4.7)	$\varepsilon_{max,theory}$	$\varepsilon_{max,DEFORM}$	$\varepsilon_{min,theory}$	$\varepsilon_{min,DEFORM}$	d/R_m
AX18	0.218	0.71	0.245	0.243	0.196	0.194	0.20
AX9	0.255	0.69	0.334	0.312	0.156	0.141	0.22
AX5	0.276	0.67	0.401	0.346	0.153	0.121	0.25

According to the plane strain theory, the increase of strain in the inner layer due to the shift is increasing for decreasing r_d/t ratios. For all the simulations, the neutral axis is out of the sheet, because of the high membrane strain.

4.3.3 Global effects due to sliding and unbending

As the draw-in continues, the bent portion of the sheet as in Fig. 4.4 is subjected to sliding and unbending when entering the unsupported region. The total radial strain due to successively bending, sliding, and unbending increases, because of the increase in the restraining force T_s as described in Equation (4.15). The increased force affects not only the strain in the area around the die corner radius but also in the unsupported region and in the area under the punch. The effect on radial strain is shown in Fig. 4.5, 4.6, and 4.7. These figures show that

the strain increases in the whole sheet for small r_d/t ratios. Figure 4.9 shows the radial strains at the middle layer for the three r_d/t ratios at a punch travel of 45 mm. For AX5 the overall strain increase is significant. The difference in middle layer strain is about 3% to 9% when the r_d/t ratio drops from 9 to 5. Figure 4.10 represents the average effective strain as defined in Equation (4.16) at 45 mm punch travel. The effective strain is averaged over the middle, inner, and outer layers to take both local effects (occurring in outer and inner surfaces) and global bending effects into account.

$$\bar{\varepsilon}_{average} = \frac{\bar{\varepsilon}_{inner} + 2\bar{\varepsilon}_{middle} + \bar{\varepsilon}_{outer}}{4} \tag{4.16}$$

Fig. 4.10 shows again that the effective strain increases not only around the die corner radius but also at the unsupported region. For r_d/t ratios from 18 to 9 the difference in effective strains is not very significant. However when the ratio drops from 9 to 5, the overall increase in average effective strain is significant.

From these observations the following conclusions are drawn:

(a) Membrane codes do not provide accurate results for small r_d/t ratio ($r_d/t<9$). The error due to neglecting the global effects reaches 7% to 8% for AX5, relatively speaking this is a 30% increase in the radial strain,
(b) Global effects must be taken into account when using bending correction models in order to obtain a more accurate prediction of the strains. Because of the increase in effective strain, also the effective stress increases. Thus, when including global bending correction in a membrane code, the correction has to be made after each increment in order to correct the stresses too. However, for axisymmetric deep drawing no global bending correction model exists.

Load-stroke diagrams for three simulations

Figure 4.11 shows the load-stroke diagrams for the three simulations. The maximum load is the highest for AX5, as expected, due to the strain hardening in the overall sheet, which causes higher tensile stresses. Thus, the punch load increases for decreasing ratios. However this increase is not very high.

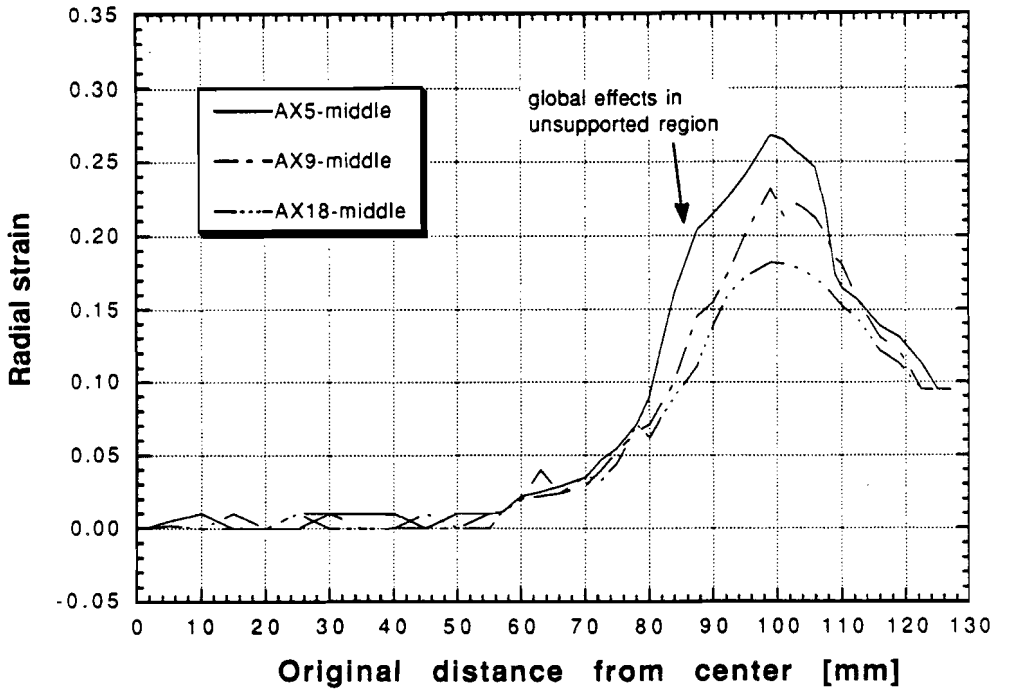

Fig. 4.9 Middle layer strain at a stroke of 45 mm to show global effects due to unbending and sliding for three simulations AX18, AX9 and AX5

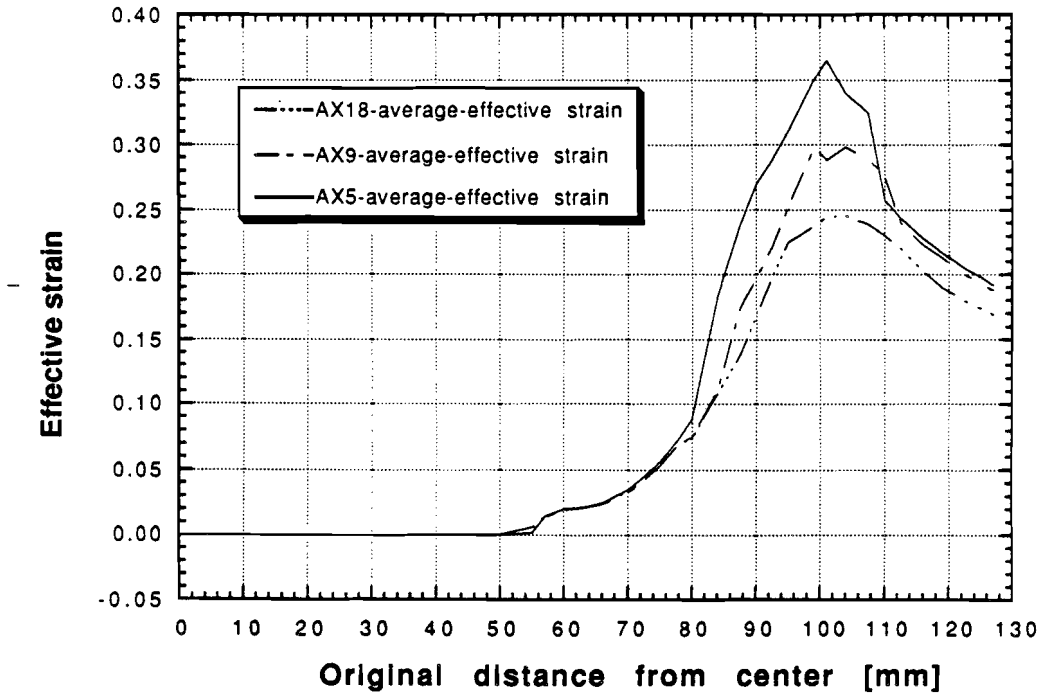

Fig. 4.10 Average effective strain to show influence of r_d/t ratio on global and local bending effects for AX18, AX9, AX5 at a punch travel of 45 mm.

Wall thickness variation for different ratios

In order to investigate the influence of the die corner radius on the thickness of the wall, the thickness strain distributions at a stroke of 45 mm are shown for AX18, AX9, and AX5 in Fig. 4.12. For AX18 and AX9, the distributions are quite similar. For AX5, however, there is a significant strain increase, due to the higher punch force. The force increase causes more stretching in the unsupported region. Thus, the material originally located at the punch nose starts thinning, since it is not as much strain hardened as the material in the unsupported region. This causes negative thickness strains. The thickening of the flange increases for decreasing r_d/t ratios due to higher compressive stresses. The influence of the die corner radius on both thinning at the punch nose and thickening at the flange are confirmed by experiments in deep drawing of a square box by El-Wakil et al., [1980].

4.4 DEFORM compared with SHEET_FORM (axisymmetric)

If the membrane results from SHEET_FORM agree with the DEFORM middle layer strains for the simulations using three r_d/t ratios, it is possible to add bending correction to SHEET_FORM to include the bending strains in the results. In this section, SHEET_FORM membrane strains are compared with DEFORM middle layer strains and SHEET_FORM results with local bending correction are compared with DEFORM, by comparing the outer, inner and middle layer strains as calculated by both the codes.

4.4.1 Bending correction models

The membrane approach neglects bending effects and the strain distribution through the thickness is assumed to be constant. Only for large r_d/t ratios ($r_d/t>18$) this approach provides reasonable results. Solid or shell elements do include bending effects. However, the computational efficiency is worse because these elements have increased degrees of freedom (6 vs. 3) and therefore, require longer computation time. Bending correction models can be added to the membrane codes to take advantage of both the computational efficiency of the membrane codes and at the same time, to take the bending effects into account.

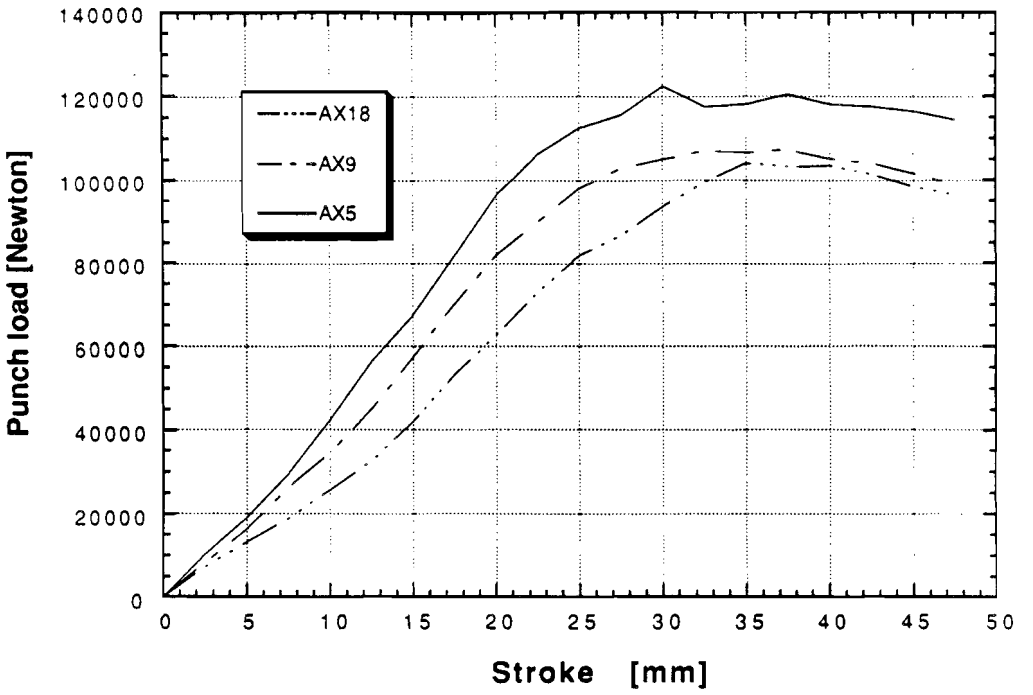

Fig. 4.11 Load-stroke diagrams for AX18, AX9 and AX5 to show influence of r_d/t on the load-stroke diagram

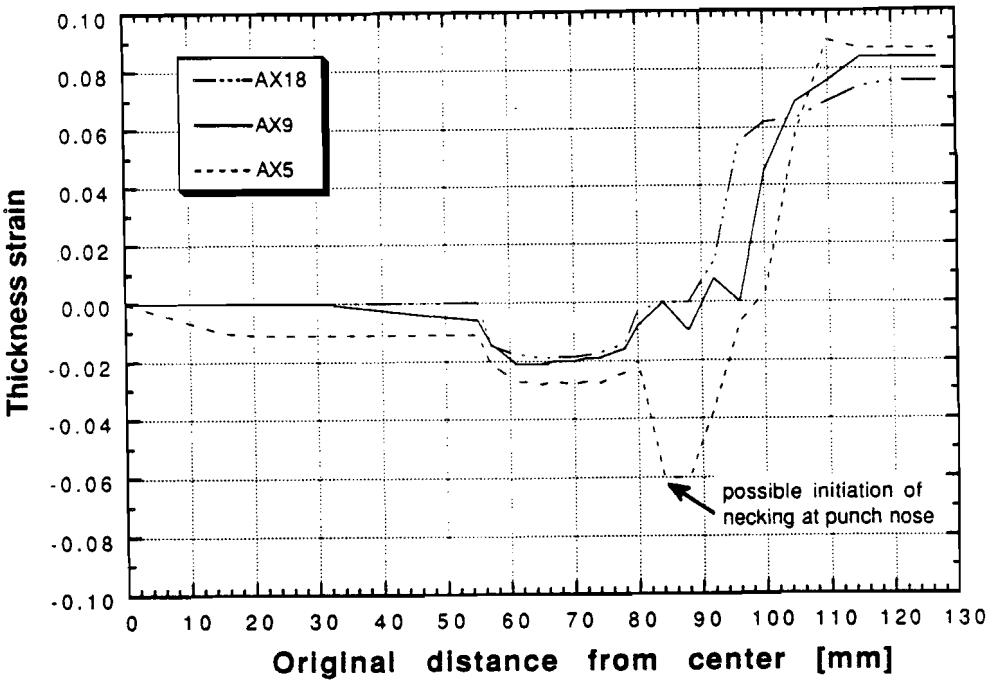

Fig. 4.12 Thickness strain for AX18, AX9 and AX5 at a punch travel of 45 mm

There are several bending correction models, from simple (only local) to advanced (both local and global). These bending corrections are significant for small ratios r_d/t (<9).

For local effects, the simple bending strain calculated from the plane strain theory (as in Equation (4.2)) is added to the membrane strain at the nodes contacting the tool curvatures. The bending strains at the concave and the convex surfaces are calculated according to Equation (4.2), using the curvature of the neutral axis and the current thickness (as in equation (4.7)) from the membrane analysis. For membrane finite elements, the curvature of the neutral axis is calculated as the average value of the radii at each node of an element contacting the die or punch corner radius, since there is only one element in thickness direction, [Stoughton, 1985]. The average of the inner and outer bending strains is zero, since the neutral axis is assumed to be the middle axis. Therefore the local bending correction does not affect the flow stress and effective strain. Hence bending correction is only necessary at the final punch depth.

The global bending correction is not possible for axisymmetric deep drawing, since there is no valid model.

4.4.2 SHEET_FORM

SHEET_FORM is a membrane code based on the Finite Difference Method (FDM) which can analyze axisymmetric and plane-strain deep drawing processes. The deep drawing analysis used in SHEET_FORM is based on Woo's approach, [Woo, 1964; Woo, 1968]. The cup drawing process is divided into two stages:

(a) the embossing stage
(b) the drawing stage

In the beginning of the drawing process, the punch bottom shape is merely impressed on the undeformed blank, so the required punch load is small. This is called the embossing stage. When the punch travel increases, the flange is compressed and the material is bent over the die corner radius. As draw-in proceeds, the material is subjected to sliding and unbending. Then, it enters the unsupported region. This is called the drawing stage. In this stage, the cup can

be divided into six distinct zones as shown in Fig. 4.13 and for each of these zones several equations for volume constancy and equilibrium have to be satisfied. A detailed description of the formulation and the equations for these zones can be found in Ahmetoglu [1990], and Sitamaran, [1989]. The stresses and strains are related by Hollomon's power law equation and the material is assumed to be rigid-plastic. The modified Coulomb friction law is used to describe the interface between the tools and the workpiece.

A local bending correction model is implemented in SHEET_FORM, similarly to the correction as described in section 4.4.1. Three simulations are performed using the same process parameters and tool geometry as in DEFORM for AX18, AX9, and AX5 to investigate the agreement of SHEET_FORM with DEFORM (solid elements). Instead of comparing SHEET_FORM (with local bending correction) with DEFORM, it is more preferable to compare it with experimental data. However, it is very hard to obtain accurate strain measurements on the inner side of the cup. The strain in the middle layer can not be measured at all. In this case DEFORM results are taken as reference instead of experimental data. If the membrane code SHEET_FORM provides an accurate strain distribution for the middle layer, then, the influence of the local effects can be added by using a local bending correction model.

It is expected that for r_d/t ratios larger than 9, the results from SHEET_FORM agree well with DEFORM results. For smaller ratios, however, the global bending effects are too important to neglect and the agreement will be worse. The sheet is modeled by 120 elements, one element in thickness direction. The computational efficiency for SHEET_FORM is good, the average CPU time is about 5 to 10 minutes on a VAX.

4.4.3 Local bending effects and local bending correction

Figure 4.14, Fig. 4.15, and Fig. 4.16 show the radial strain distributions from DEFORM and SHEET_FORM for AX18, AX9, and AX5 respectively at a punch travel of 45 mm. The agreement of SHEET_FORM with a local bending correction is not perfect but it is partly due to the influence of the global effects. For AX9 and AX18 the influence of global effects is not very significant and local bending correction of the membrane solution provides a good agreement with

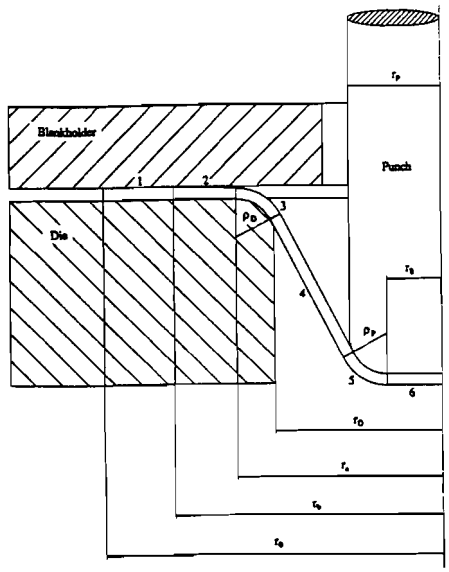

Fig. 4.13 The six different zones of the cup as used in SHEET_FORM formulation

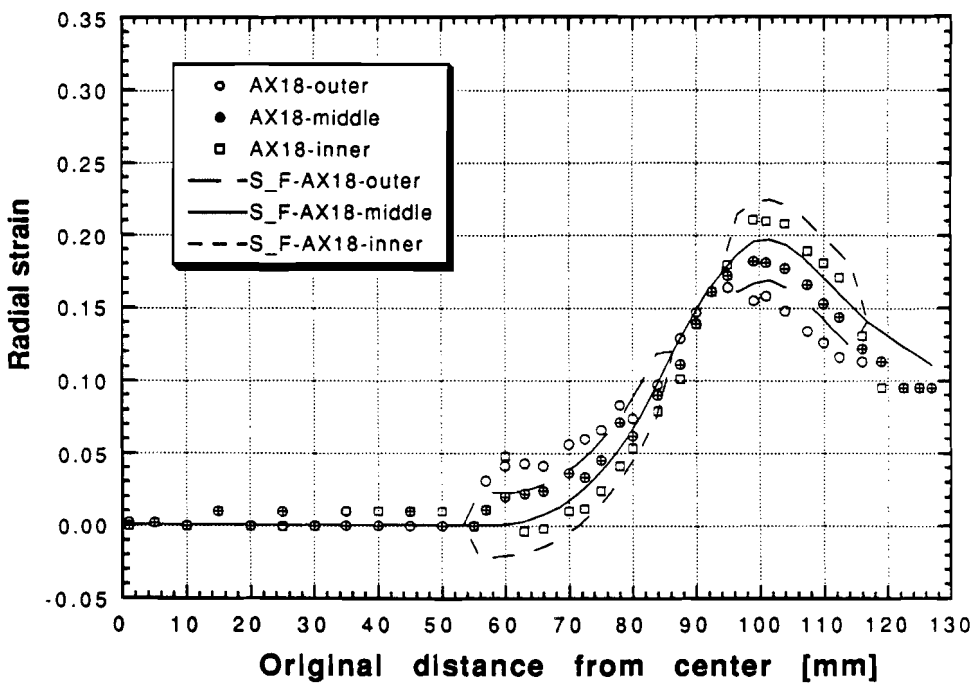

Fig 4.14 Radial strains for AX18 at 45 mm punch travel. The lines represent the SHEET_FORM results and the symbols represent the DEFORM results

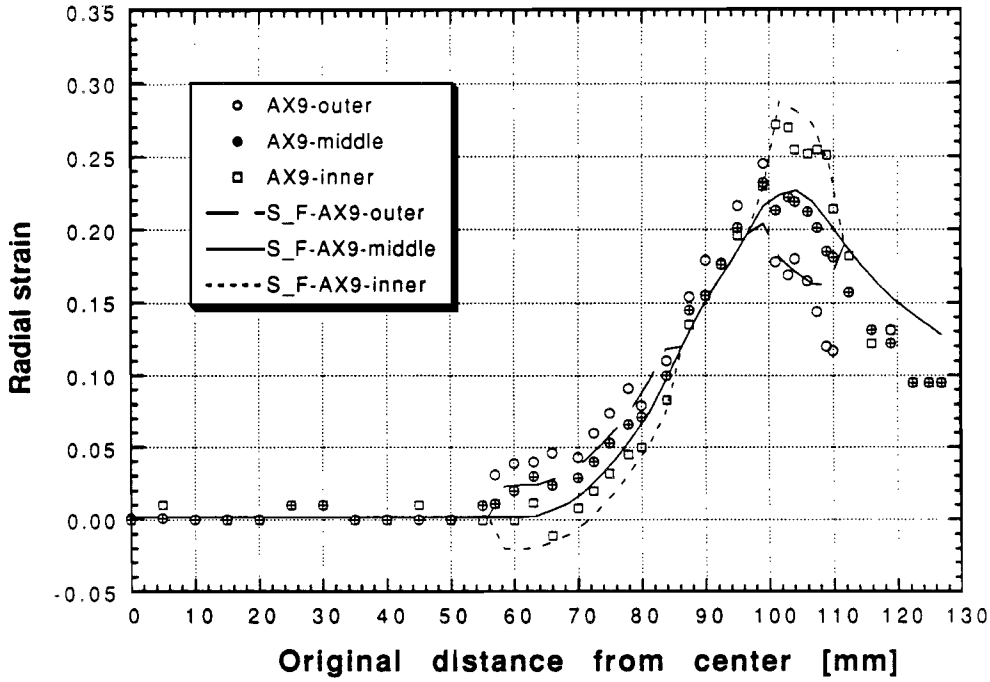

Fig 4.15 Radial strains for AX9 at 45 mm punch travel. The lines represent the SHEET_FORM results and the symbols represent the DEFORM results

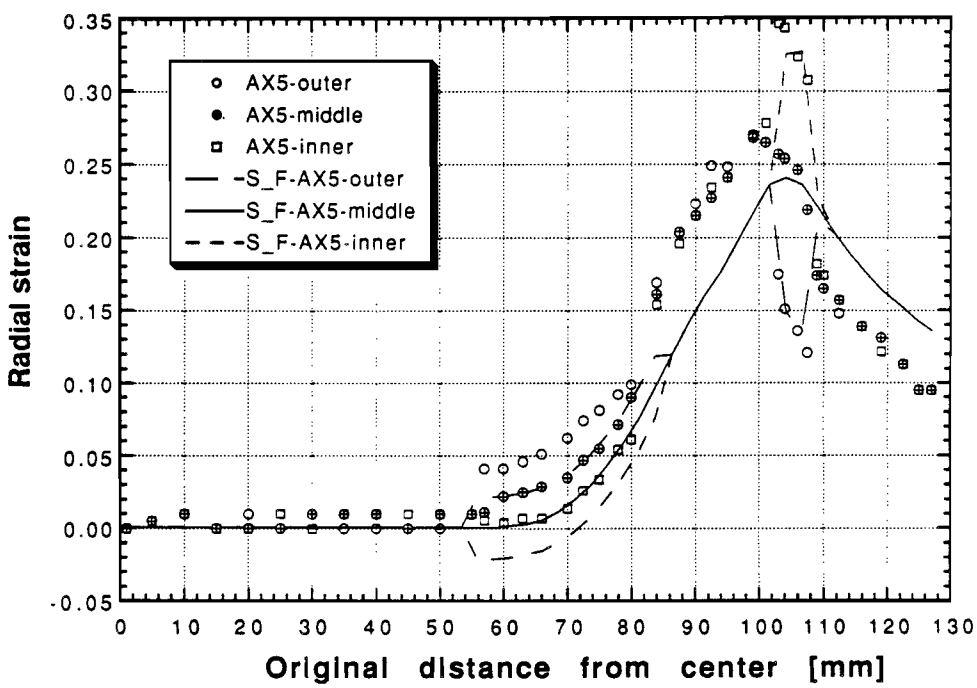

Fig 4.16 Radial strains for AX5 at 45 mm punch travel. The lines represent the SHEET_FORM results and the symbols represent the DEFORM results

DEFORM. However, if the ratio decreases to 5, the global effects increases too much and may not be neglected anymore.

4.4.4 Influence of global effects

In Fig. 4.14, 4.15 and 4.16, the outer, inner, and middle layer strain distributions for AX18, AX9 and AX5 are shown, respectively, for both DEFORM and SHEET_FORM. For AX18 and AX9, the middle layers match well, which means that (a) SHEET_FORM provides an accurate membrane strain solution for large ratios and (b) until the ratio of $r_d/t = 9$, global bending effects can be neglected. However, for AX5, the difference between the middle layers from DEFORM and SHEET_FORM is significant, due to the increasing influence of global bending effects. The only way to simulate this process properly is by using a solid or shell FEM code, since there is no valid global bending correction model for axisymmetric cases.

4.5 Simulations of plane-strain deep drawing process

In order to investigate the influence of the r_d/t ratio on bending strains and to compare the results from DEFORM with the plane-strain membrane code SHEET_FORM, two plane strain cases were simulated. The theory as described in section 4.1 is valid for plane-strain cases. If this theory to calculate the local and global bending effects matches with the DEFORM results, the bending correction can be added to the SHEET_FORM membrane solution for plane strain cases. The two simulated plane-strain cases have a r_d/t ratio of 9 and 5 respectively and will be mentioned as PS9 and PS5 in this report. The geometry and process parameters are shown in Table 4.4. Note that the punch corner and die corner radii, thickness, and blank diameter are the same as the ones used in AX9 and AX5.

Table 4.4 Name of simulation and geometry for plane-strain deep drawing

Name in graphs	r_d [mm]	r_d/t [-]	t [mm]	R_d [mm]	R_p [mm]	r_p [mm]	R [mm]	μ [−]	BHF [N/mm]
PS9	8	9	0.889	79.12	76.2	20	127	0.13	1500
PS5	4.45	5	0.889	79.12	76.2	20	127	0.13	1500

The material parameters for high strength steel (HSG) are used in the simulations, as described in section (3.2.4). DEFORM was not able to converge for a BHP of about 3 to 6 N/mm^2, probably because the elements under the blank holder are frequently changing from rigid to plastic and, from plastic to rigid. The simulations converged better when a higher BHF (1500 N/mm in width direction) was specified but still there were many iterations needed to converge and the contacting nodes were very frequently separating and contacting before one step was finished. This results in a very high CPU time, about 150 hours on a HP700s workstation. A velocity field is specified with $v_y = 0$ under the blank/die interface (from a radius of 90 mm to 127 mm) and a pressure was defined under the punch, to reduce the contact changes at this location.

4.5.1 Results for plane-strain deep drawing

The most important results such as major, thickness, and effective strain distributions are shown to obtain a better insight of the bending occurring in plane-strain deep drawing. The local bending, the shift of the neutral axis and the global effects are compared with the theory as described in Section 4.1.

4.5.2 Local bending effects

In Fig. 4.17 and Fig. 4.18 show the major strain distributions for PS9 and PS5 are shown, respectively, at a punch travel of 45 mm. At this punch travel, there is still a flange under the blank holder. Therefore the strains at the edge of the sheet are all similar. In the flange area, no bending has occurred yet. The local bending strains are significant for both PS9 and PS5. However, the bending strains are higher for PS5.

Compared to the axisymmetric simulations, the overall major strains are significantly lower in the plane-strain case, due to the absence of compressive stresses. Thus, the required punch load and the amount of stretching are smaller. The maximum difference between the middle layer strain and outer and inner surface strains is about 10% (for PS5).

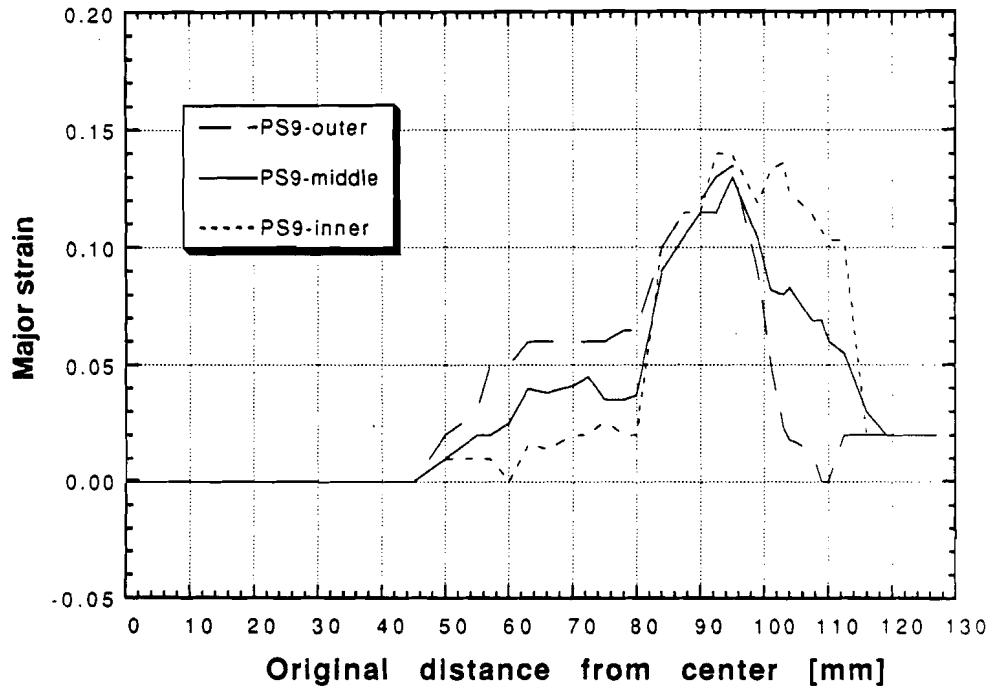

Fig. 4.17 Major strain distribution for PS9 ($r_d/t = 9$) at a punch travel of 45 mm

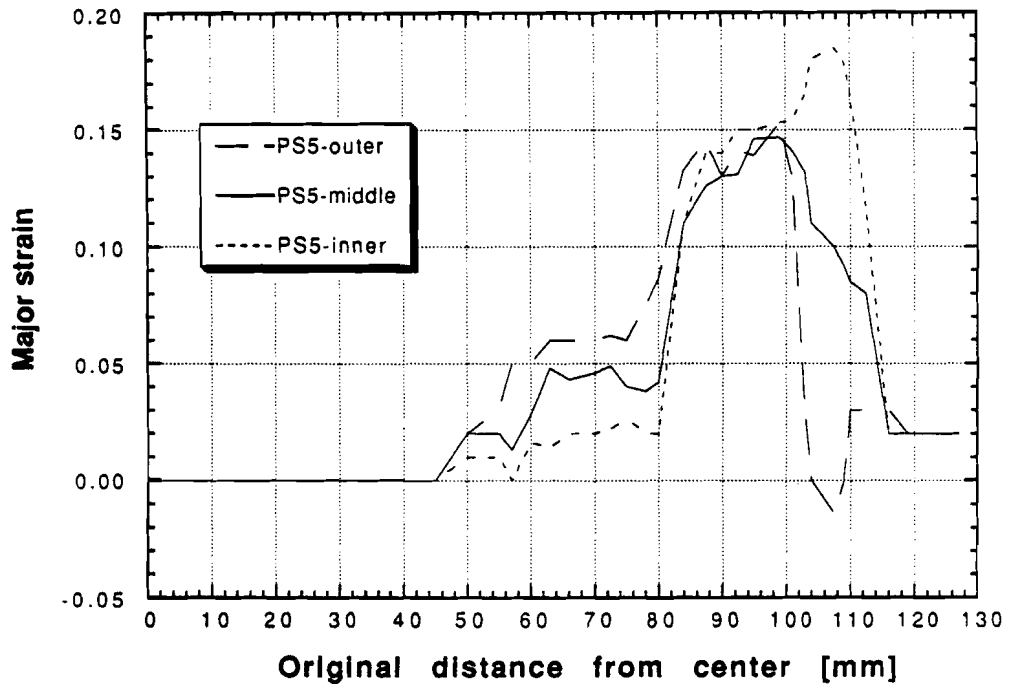

Fig. 4.18 Major strain distribution for PS5 ($r_d/t = 5$) at a punch travel of 45 mm

This means, just as in the axisymmetric cases, that local bending effects are significant for small r_d/t ratios (<9) and may not be neglected to obtain an accurate and realistic prediction of the strain distribution.

Comparison of DEFORM with theory

Figure 4.19 shows the local bending strains from the DEFORM simulations compared with the theoretical bending strain (as as calculated from Equation (4.2)). The differences between the strains at the inner and middle layers (ε_{inner} - ε_{middle}) and between the strains at the outer and middle layers (ε_{outer} - ε_{middle}) over the die corner radius give an indication of the local bending strain. In Fig. 4.18 and Table 4.5, these local bending strains are shown together with the theoretically calculated bending strains (using Equation 4.2).

Table 4.5 Maximum local bending strain ε_b at die corner radius from DEFORM simulations compared with plane-strain theory

	$\varepsilon_{outer,DEFORM}$	$\varepsilon_{outer,theory}$	$\varepsilon_{inner,DEFORM}$	$\varepsilon_{inner,theory}$
PS9	-5.7	-5.37	6.5	5.1
PS5	-10.5	-10.5	11	9.5

If there is no shift in the neutral axis, then the strains at the outer and inner surfaces are the same. The trend of the bending strain distributions along the material points subjected to bending over the die corner radius agrees well with the theoretical values from Table 4.5. However, there are some points that are considerably out of the range. Note that the theoretical strain calculation does not consider a shift of the neutral axis towards the concave curvature. The local bending strain increases rapidly when the ratio drops from 9 to 5. Then, the bending strain increases from about 5% for PS9 to 10% for PS5 as shown in Fig, 4.19.

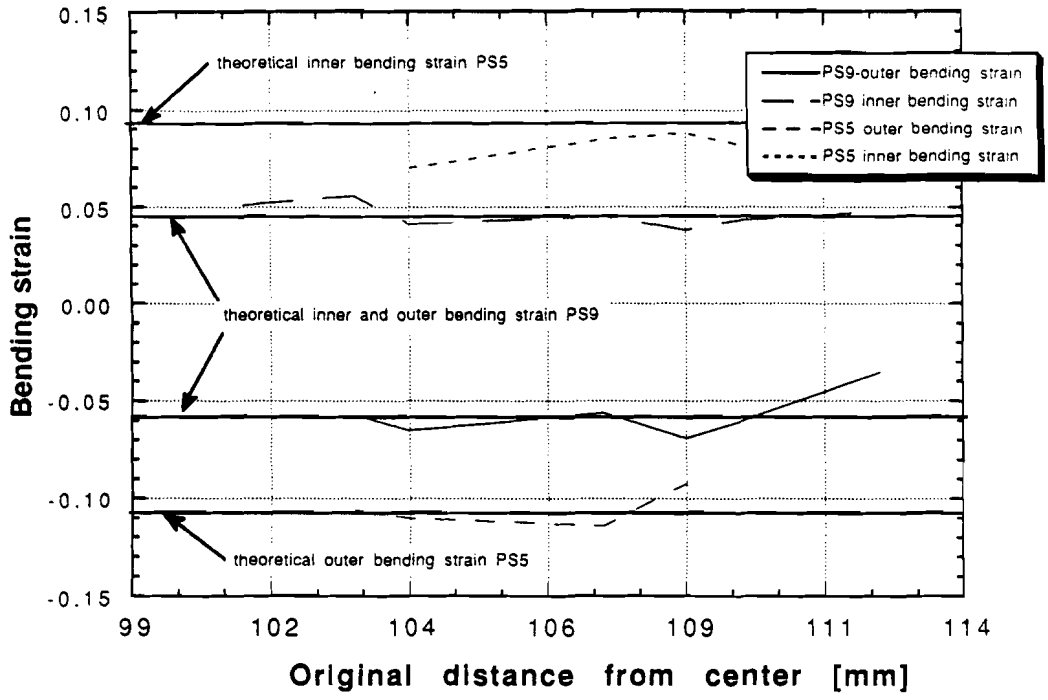

Fig. 4.19 Local bending strains at inner and outer surfaces for PS5 and PS9 compared with theoretical bending strain at 45 mm punch travel

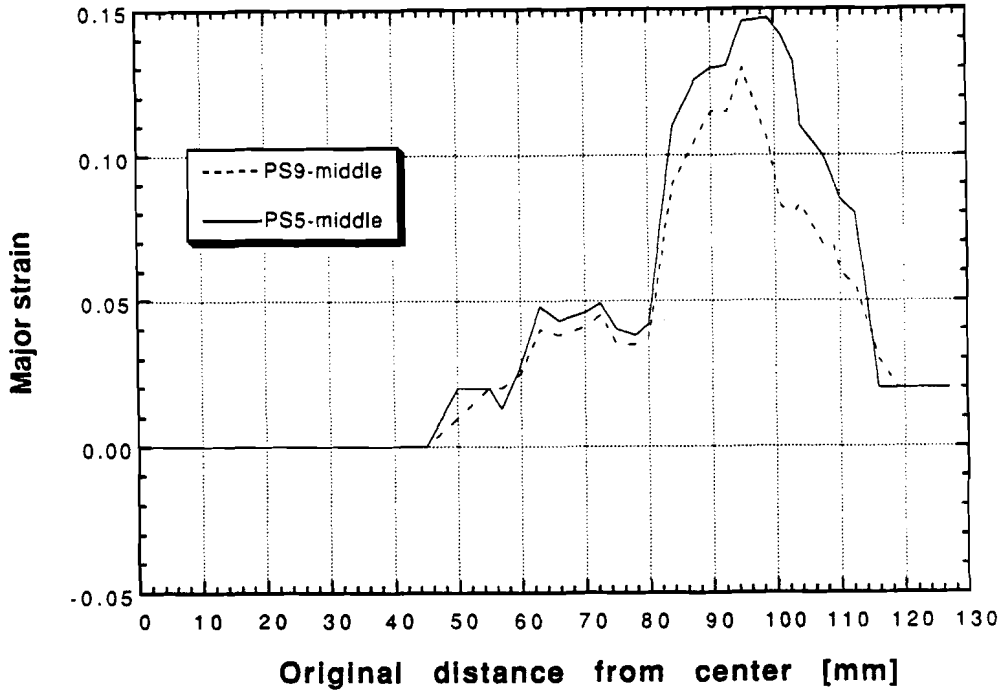

Fig. 4.20 Major strain at middle layer for PS5 and PS9 at a punch travel of 45 m m

4.5.3 The shift of the neutral axis:

The shift of the neutral axis affects the strains at the middle, inner and outer layers as shown in Fig. 4.8a. A very high restraining force results in a high membrane strain. This membrane strain is added to the bending strain, and once the membrane strain is high enough, all the strains in the convex surface are positive. The absence of compressive stresses in plane strain drawing requires a lower punch force compared to axisymmetric deep drawing, thus also the membrane strain decreases. Then, the strains in the outer surface are not necessarily positive as shown in Fig. 4.17, even though a high BHF is used.

4.5.4 Global bending effects due to sliding and unbending

The global bending effects are described in Section 4.3.4. The global bending effects on major strain can be seen in Fig. 4.17 and Fig. 4.18. Observing these figures shows that the strain increases in the whole sheet for decreasing r_d/t ratios. Figure 4.20 shows the major strains at the middle layer for PS5 and PS9 at a punch travel of 45 mm. For PS5, the strain increases in the whole sheet significantly. The differences in middle layer strain are about 3% to 6% when the r_d/t ratio drops from 9 to 5.

Fig. 4.21 represents the average effective strain as defined in Equation (4.16) at a punch travel of 45 mm, showing again that the effective strain increases for decreasing r_d/t ratios not only in the area around the die corner radius but also in the unsupported region. When the ratio drops from 9 to 5 the overall increase in average effective strain is significant.

From these observations the conclusion is drawn that for small ratios ($r_d/t<9$):

(a) Membrane codes do not provide accurate results for a small r_d/t ratio. The error due to neglecting the global effects reaches 3% to 6% for PS5, relatively speaking this is a 30% increase of the major strain.

(b) Thus, global effects must be taken into account to obtain an accurate prediction of the strains. When the effective strain increases, the effective stress also increases. Thus, the global correction has to be made to correct the stresses.

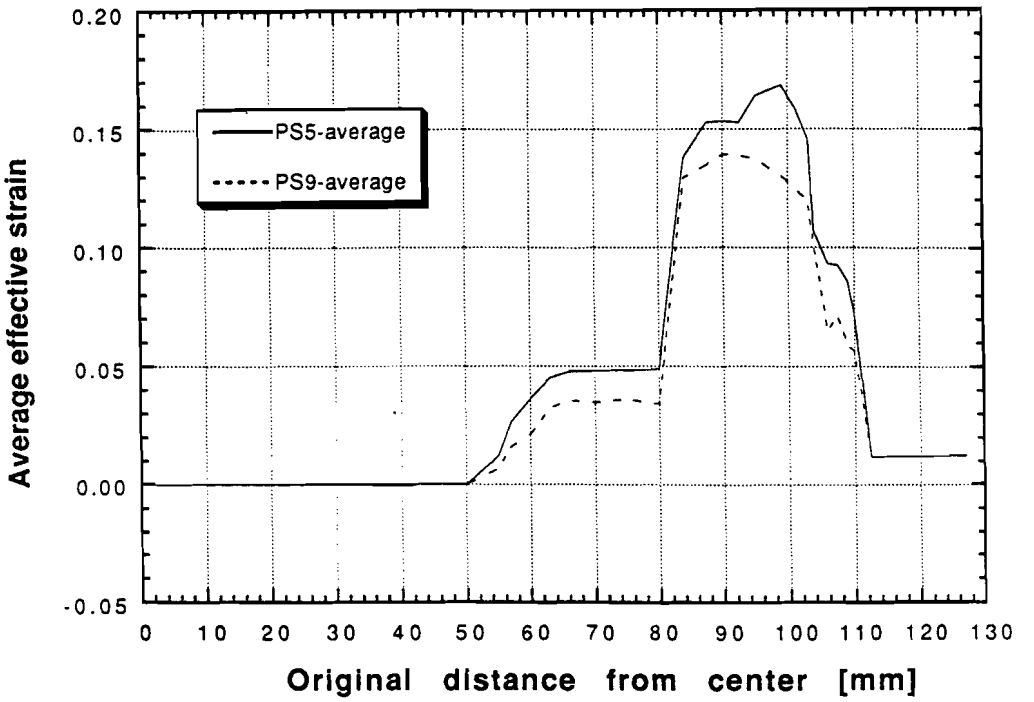

Fig. 4.21 Average effective strain for PS5 and PS9 at a punch travel of 45 mm to show influence of different die corner radii on global effects

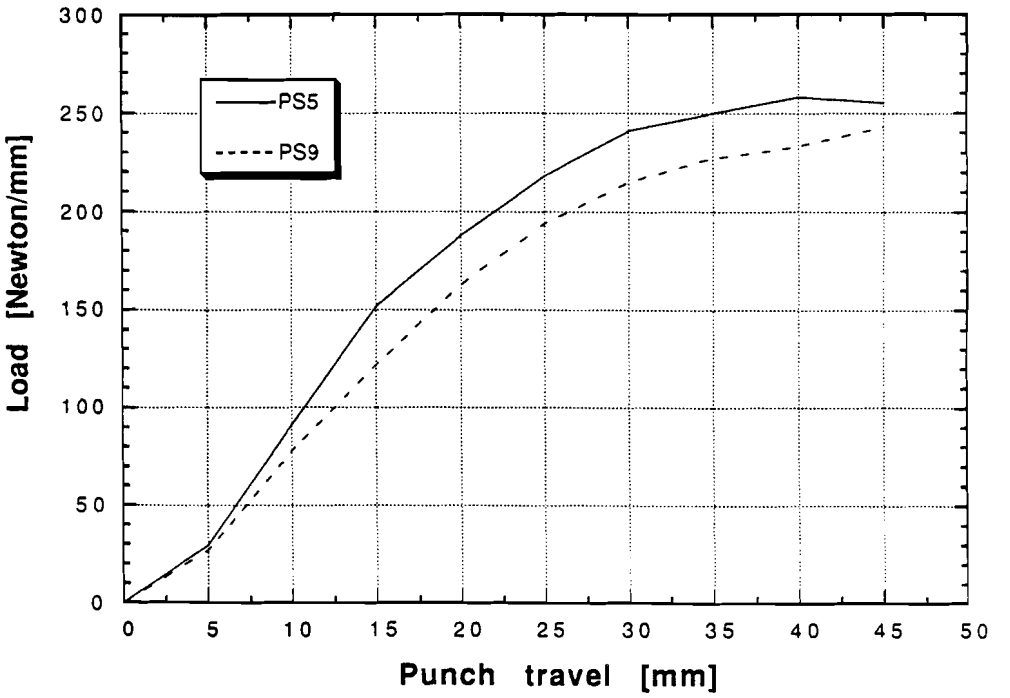

Fig. 4.22 Load-stroke diagram for PS9 and PS5 to show influence of global effects on the required punch load

Load-stroke diagrams for plane-strain simulations

The load-stroke diagrams for the two plane-strain simulations are shown in Fig. 4.21 to show the influence of a decreasing r_d/t ratio. The maximum load is the highest for PS5, as expected, due to the higher strain hardening in the overall sheet, which causes higher tensile stresses. This increases the required punch load to complete the drawing.

Wall thickness variation

In Fig. 4.23 the thickness strain is shown at a stroke of 45 mm for PS9 and PS5 to investigate the influence of the die corner radius on the thickness strain. Due to the increase in the tensile force for PS5 the maximum negative thickness strain at the unsupported region is higher than that of PS9. The thickening of the flange is far less than that in the axisymmetric case, since there are no compressive stresses in plane strain drawing.

4.6 DEFORM compared with SHEET_FORM (plane-strain)

DEFORM results are compared with a membrane code. If the membrane results from SHEET_FORM simulations agree with the DEFORM middle layer strains it is possible to add bending correction to SHEET_FORM to include bending effects. SHEET_FORM with local bending correction is compared with DEFORM by showing the outer, inner and middle layer strains for both the codes.

4.6.1 Local bending effects and local bending correction

In Fig. 4.24 and Fig. 4.25, the major strain distributions from DEFORM and SHEET_FORM for PS9, and PS5 respectively are shown at a punch travel of 45 mm. These figures show the influence of local bending effects. The agreement of SHEET_FORM with DEFORM is reasonable. The discrepancies may be due to the influence of the global effects for PS5. For PS9, the influence of global effects is not very significant. When the ratio decreases to 5, the influence of the global effects increases too much and therefore, necessary corrections have to be made.

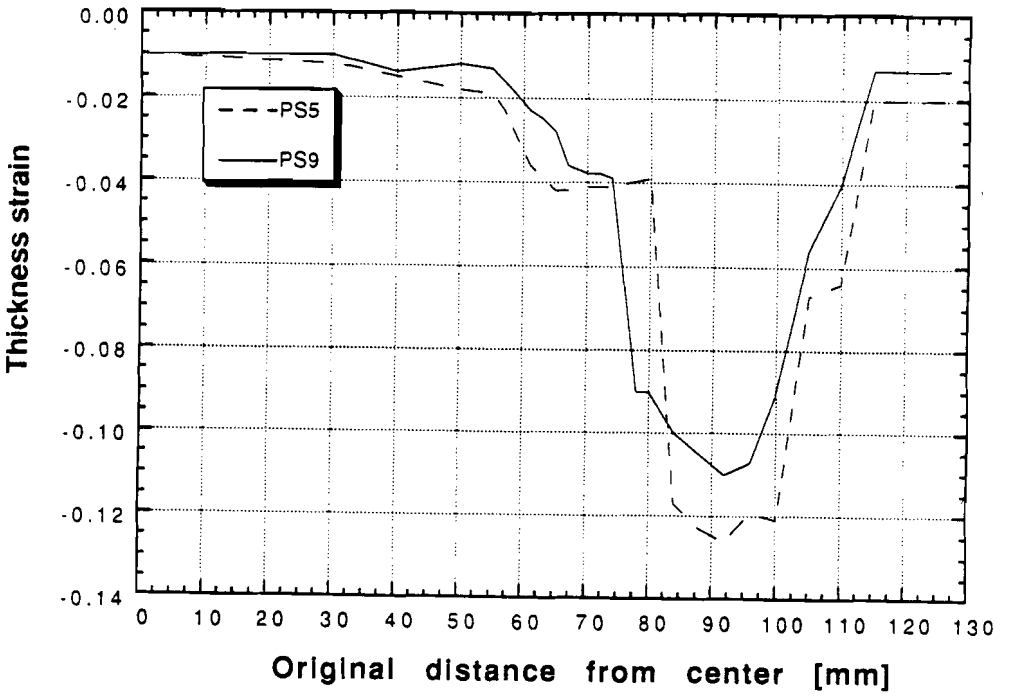

Fig. 4.23 Thickness strain distribution for PS9 and PS5 at a punch travel of 45 mm

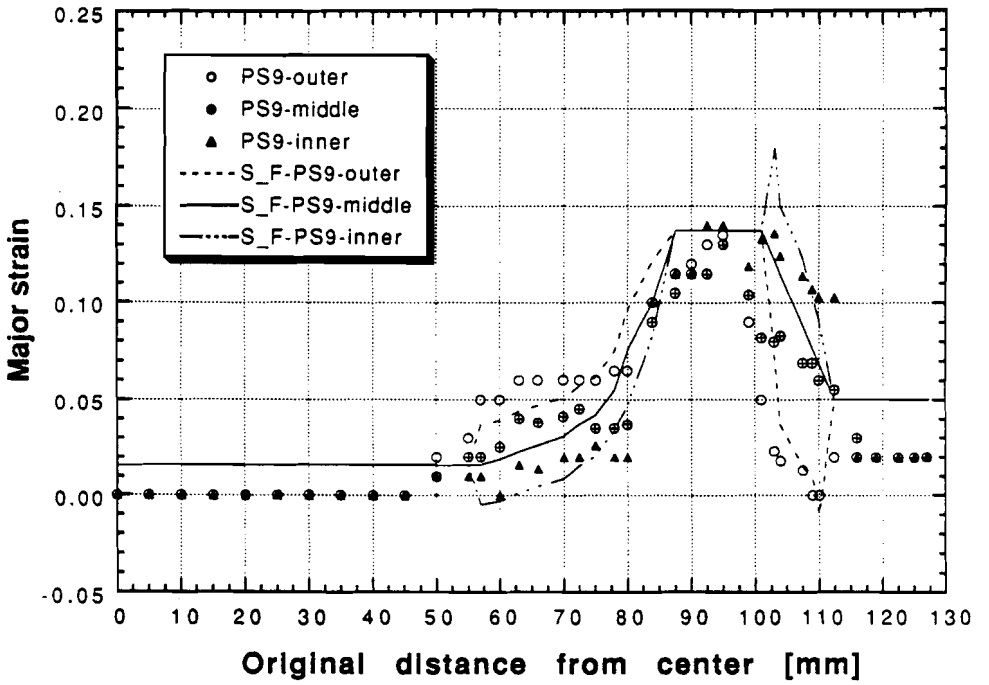

Fig. 4.24 Major strains in three layers for PS9, at a punch travel of 45 mm, where the lines represent SHEET_FORM and the symbols DEFORM

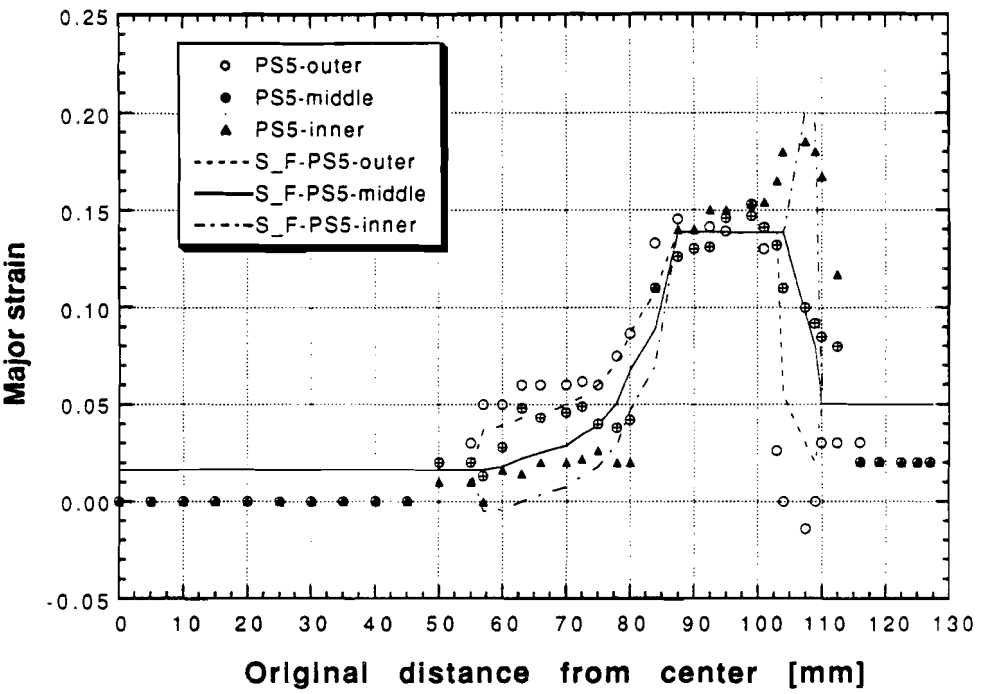

Fig. 4.25 Major strain in three layers for PS5, at a punch travel of 45 mm, where the lines represent SHEET_FORM and the symbols DEFORM

4.6.2 Influence of global effects

In Fig. 4.24 and 4.25 the outer, inner, and middle layer strain distributions for PS9 and PS5 are shown, respectively, for both DEFORM and SHEET_FORM. For PS9 these lines match well, which means that (a) SHEET_FORM provides an accurate membrane strain solution for large r_d/t ratios and (b) until this r_d/t ratio reaches the value of (9) global bending effects can be neglected.

4.6.3 Global bending correction in plane-strain deep drawing

In order to correct for global effects, first of all the membrane solution has to be calculated. Then, the membrane strain can be approximated in the area where the sheet is bent over the die corner radius. This membrane strain is used to calculate the shift of the neutral axis, according to Equation (4.4). The shift, d, of the neutral axis is necessary to calculate the bending surface strains, as defined in Equation (C.10) and (C.11a, b). Once these inner and outer surface strains are known, the bending moment is calculated, using Equation (C.13). This bending moment M_b is used to calculate the increase in tensile force, due to sliding and unbending. The tensile force increase is calculated using Equation (4.14). If this increase is significant, global bending correction has to be applied.

To take into account the increased tensile force, the assumption is made that by increasing the friction coefficient between die/blank and blank/blank holder interface, the tensile force in the unsupported region is increased. Once the new friction coefficients are determined, the simulation has to be rerun, using the new friction coefficient. Then, global bending effects are included, and since SHEET_FORM already has a local bending correction, the prediction of the strain distribution should be more accurate than that found using a conventional membrane code. In order to verify the accuracy of the theory, SHEET_FORM simulations including global bending correction are performed and compared with DEFORM results. The subsequent steps and equations which are required to take the global bending effects into account are mentioned below.

STEP 1 : Calculate membrane stress without correction

STEP 2 : Determine shift of the neutral axis, using eqn (4.4)

$$d = (r_d + t_0/2.e^{-\varepsilon_{membrane}})(1 - e^{-\varepsilon_{membrane}})$$

STEP 3 : From the shift, d , the characteristic strains are calculated as in equation (C.10) and (C.11a, b) :

$$\varepsilon_0 = \frac{\sigma_0}{E'} \quad , \quad \varepsilon_i = \ln(1 - \frac{t/2 - d}{R_n}) \text{ and } \varepsilon_{max} = \ln(1 + \frac{t/2 + d}{R_n})$$

STEP4 : Once the characteristic strains are known, the bending moment is calculated, using eqn (C.13) :

$$M = \frac{2}{3}R_n^2 E' \varepsilon_o^3 + KF^{n+1}R_n^2\left\{\frac{1}{n+2}\left[\varepsilon_{max}^{n+2} - 2\varepsilon_0^{n+2} + \varepsilon_i^{n+2}\right] + \frac{3}{2(n+3)}\left[\varepsilon_{max}^{n+3} + \varepsilon_i^{n+3}\right]\right\}$$

STEP 5 : The increase in tensile force, T_s , is calculated, using eqation (4.4) :

$$T_s = T_b.e^{\mu\phi_0 . r_d / R_m} - \frac{2}{1 + e^{-\mu(\phi_0 - \phi).r_d / R_m}} \frac{M_s - M_b}{R_m}$$

Where : $T_b = 2.\mu.(BHF)$

STEP 6 : The simulation has to be rerun, using the corrected friction coefficient. The new friction coefficient is calculated as :

$$\mu_{new} = \frac{T_s}{2(BHF)}$$

Calculation of the new friction coefficient for PS5

STEP 1: Shown in Fig. 4.24	$\varepsilon_{mem,max}$=		0.138
STEP 2: Shift of neutral axis (for $\varepsilon_{membrane,max}$=0.138)	d	=	0.63 mm
STEP 3: Characteristic surface strains:	ε_0	≈	0
	ε_i	=	0.05
	ε_{max}	=	0.257
STEP 4: with F=1.23 (R=1.4) the bending moment	M_b	=	571 Nmm
STEP 5: T_b=390N/mm, thus $T_s = 1.21T_b + 0.46M_b$	T_s	=	734 N/mm
STEP 6: The new friction coefficient:	μ	=	0.25

Rerunning the simulation with the increased friction coefficient should provide a more realistic result and a better agreement of SHEET_FORM with DEFORM. Fig. 4.26 shows the strain distributions for PS5, using three different friction coefficients, μ = 0.13 (initial coefficient), μ = 0.15 and μ = 0.25 (corrected friction coefficient) together with the DEFORM middle layer strain for μ = 0.13. There is only a slight difference in the maximum strain obtained in the unsupported region, even though the friction coefficient increases significantly. Another suggestion to include global bending correction is to define a tensile force directly, instead of increasing the friction coefficient or the BHF. This is not investigated in this report.

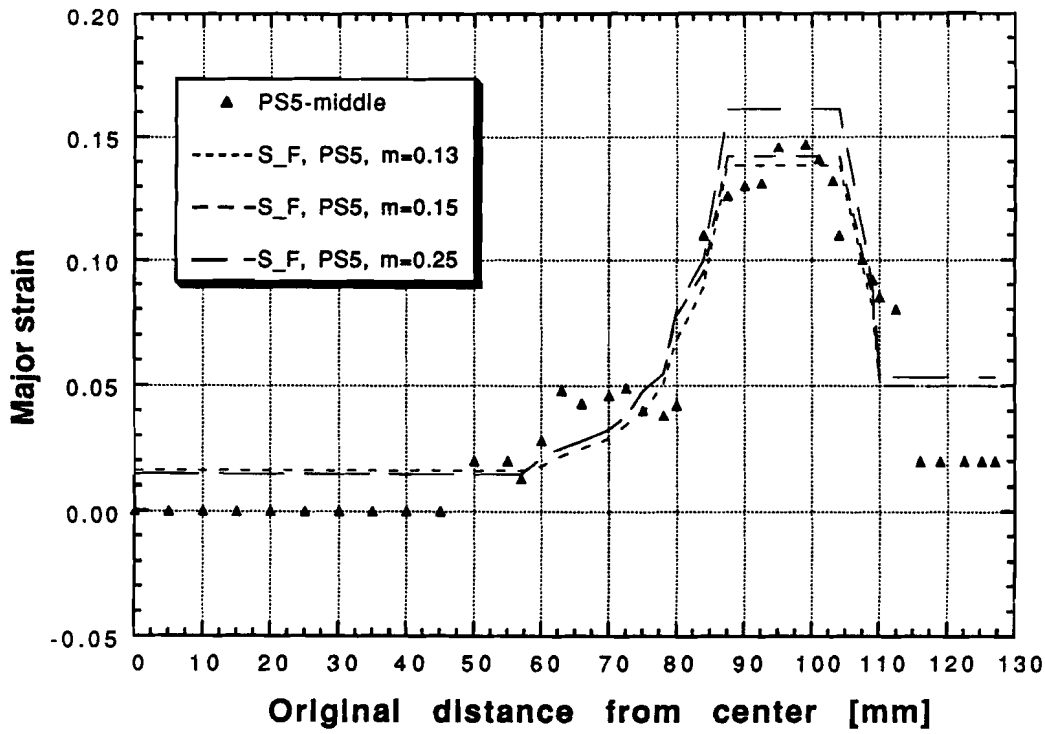

Fig. 4.26 Membrane strain from SHEET_FORM for μ=0.13, 0.15, and 0.25 and middle layer strain from DEFORM (μ=0.13)

CHAPTER V

3 - D SIMULATIONS OF DEEP DRAWING A SQUARE BOX

In this chapter, the effect of BHF on thickness strain distribution is investigated by performing 3D-simulations of deep drawing square boxes, using the code SHEETFORM-3D, [Darendeliler, 1991]. In these simulations, both constant and variable BHF, as a function of location is used.

5.1 Background on deep drawing a square box

The analysis of deep drawing square and rectangular boxes is far more complicated than axisymmetric deep drawing, because deformation states and the metal flow vary along the periphery of the box. The fracture initiation takes usually place in the corner regions. The metal in the flange region flows from the corner to the straight sides, so that the compressive circumferential stress decreases compared to axisymmetric deep drawing. This is called the strain relief effect. Figure 5.1 shows a quarter of the square cup and the typical zones with their specific deformation state, [Kawai et al., 1987]. In region B, the drawing deformation occurs consuming a considerable amount of the work load. However, the material located in region A translates rigidly, without significant deformation. The shear region C divides the corner region and the straight sections D and E. The metal flows from region B to D and E, causing the thickness increase in region D. Since these regions have different thickness strains, it is necessary to evaluate at least two different cross-sections of the cup when performing simulations or experiments. In Fig. 5.1 these two sections are represented by the a) line y-x and b) either the y or the x- axis. The thickness profiles of the corner section and the side wall sections are shown in Fig. 5.2, [Karima et al., 1989].

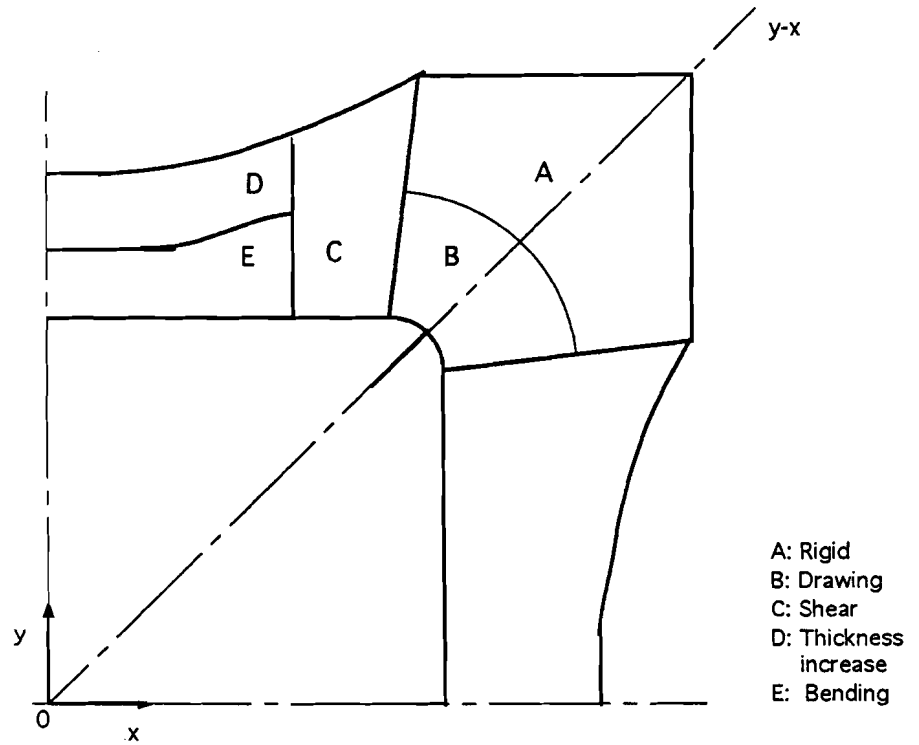

Fig. 5.1 Quarter of a square cup showing the different areas in the flange based on deformation behavior, [Kawai et. al., 1987]

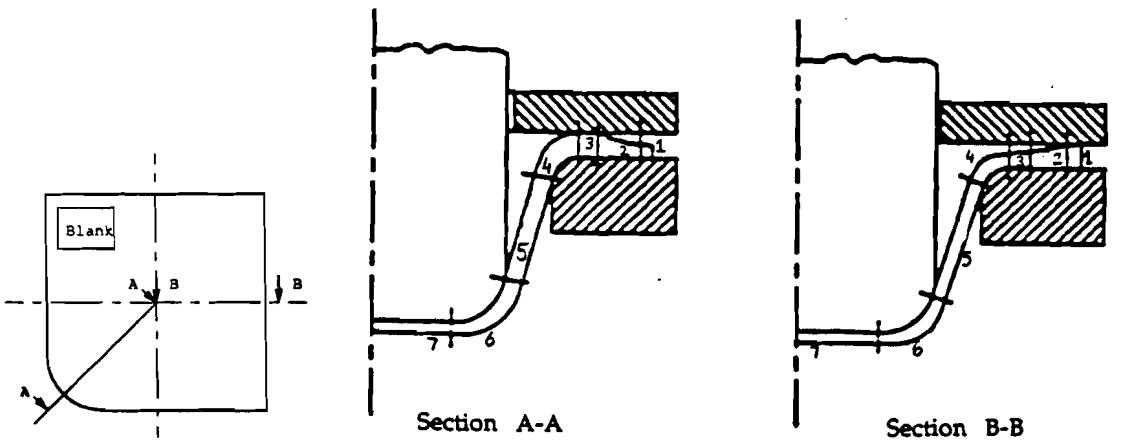

Fig. 5.2 Material thickness variation in two different sections in deep drawing a non-axisymmetric part, [Karima and Donatelli, 1989]

As it is shown in Fig. 5.2 (Section A-A) in a corner section, the maximum thickening occurs at zone 3, and zone 1 is rigid. However, in the side wall section, maximum thickening occurs in zone 1 and zone 3 is rigid. There are several parameters affecting the final quality of a deep drawn square box. The initial blank shape and blank size influence thickness strain and the amount of wrinkling, especially when using square blanks, wrinkling may occur in the corner sections, since the compressive stresses are maximum in these sections. In the side walls wrinkling can also occur, depending on the geometry. Figure 5.3 shows the sheet thickness patterns for different initial blank shapes. The die profile radius i.e., the radius over which the sheet is bent, affects the amount of thinning as proven earlier in Chapter 4 of this report. Experiments conducted by El-Wakil et al., [1980] confirm that if the bending radius decreases, the sheet thinning in the vertical wall and the punch force increases due to the increase of the tensile force.

5.1.1 Background on the effects of BHF in deep drawing of square cups

In deep drawing the metal flow is mainly controlled by the blank holder. The most important reason to use a blank holder is to prevent the occurrence of wrinkling. A square box tends to wrinkle in the corner section due to the high compressive stresses. However, in the straight part wrinkle may also occur. Therefore, the influence of the BHF is again significant as in axisymmetric deep drawing.

In deep drawing rectangular or square parts, draw beads are used to restrain the straight sides, and thus, to obtain a uniform metal flow throughout the periphery of the part. The bending and unbending of the sheet over the draw beads creates a thickness reduction in the side walls. A locally increased BHF in the straight sides might give the similar result as when using a drawbead. Fracturing usually occurs at the bottom of the box, at the corners, which is similar to axisymmetric deep drawing. Since there is thickening in the side wall section, the BHF acts mainly on this region and secondarily on the corner section. Thus the BHF inhibits the flow of metal from the flanges to the vertical wall and the metal in those walls is therefore strained and exhausted when applying a high BHF.

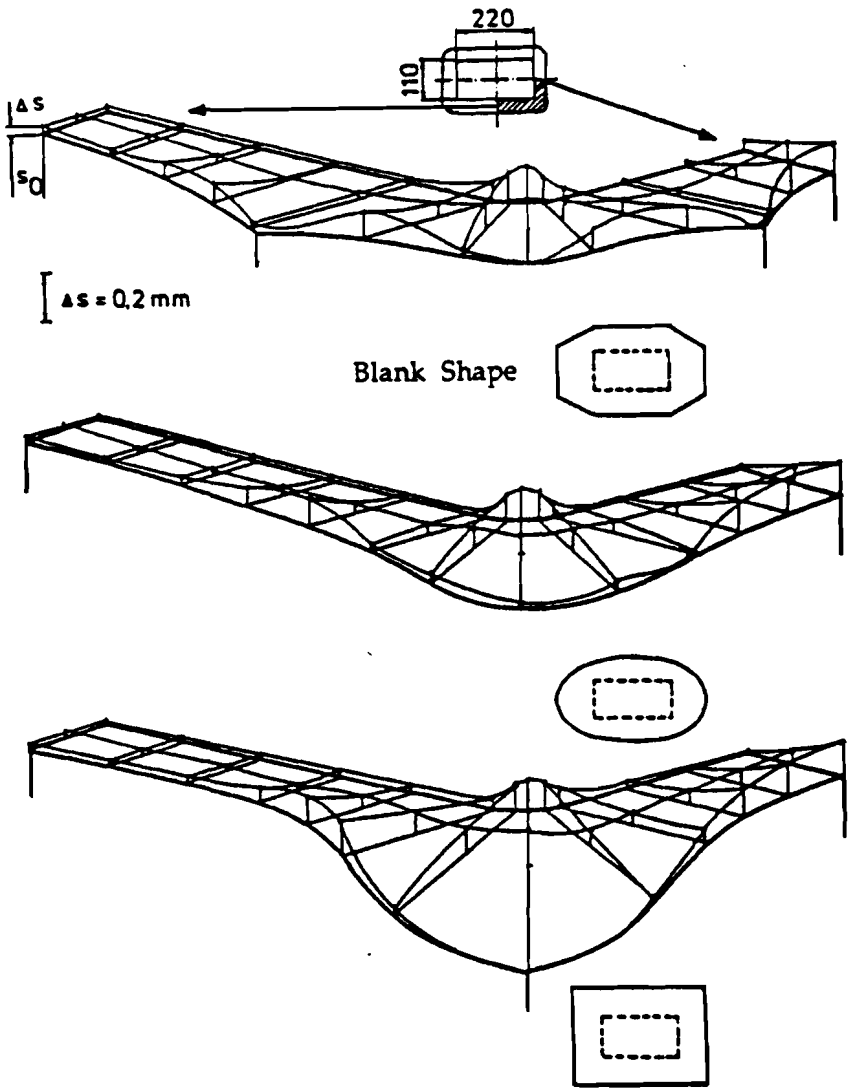

Fig. 5.3 Increase in sheet thickness in deep drawing of rectangular parts for several initial blank shapes, [Doege and Sommer, 1987]

Since wrinkling occurs at locations of maximum thickness in drawing rectangular or square parts, a BHP is mostly required near the inner corner radii and the outer periphery of the side wall.

If a constant BHF is used, the BHF should be kept within a certain range, the 'drawability window', to obtain the required depth, as shown in Fig. 5.4. For each combination of tool geometry, material, sheet thickness, friction, BHF, there is a different drawability window, its size and shape depending on these factors. The adjustment window is between (A) and (C), Fig. 5.4. The higher the drawability, the larger is the draw depth. The thinner the sheet, the more critical is the severity of drawing and the narrower is the drawability window. For a low BHF, the cup height is limited by a tendency for wrinkling (A), while at a high BHF the cup height is limited by fracture (C) at the unsupported region, close to the punch nose. Figure 5.4 shows the drawability window between (A) and (C) for a certain draw depth (Y). With a BHP of (X), the blank will neither fracture nor wrinkle with safety factors of (A-B) for wrinkling and (B-C) for fracture. Material properties and strength affect the wrinkling and fracture limits , as shown in Fig. 5.5, thus the BHF should be changed for different grades of steel. To reduce wrinkling for higher yield strength steels, a higher BHF must be applied.

The effects of the blank size and die corner radius on the wrinkling and fracture limits are shown in Fig. 5.6, [Patrishkoff, 1991]. The safety zone represented by the triangular area between wrinkling and fracture limits moves to the right or left, depending on blank size or die corner radius. By varying the BHF as a function of the punch travel, it is possible to increase the limiting drawing ratio (i.e. the ratio of blank diameter to punch diameter) or to increase the cup height. Mostly, it is not desirable to keep the BHF constant throughout the deformation, since different modes of failure become important at different punch travels. Flange wrinkling is important at the beginning of deformation due to the high compressive stresses which are building up in the flange. As the draw-in continues, radial stresses increase in the cup wall, and fracture may occur due to stretching. The flange area on the other hand decreases, and thus wrinkles at flange become less severe. Then, the BHF has to be decreased in order to prevent fracture.

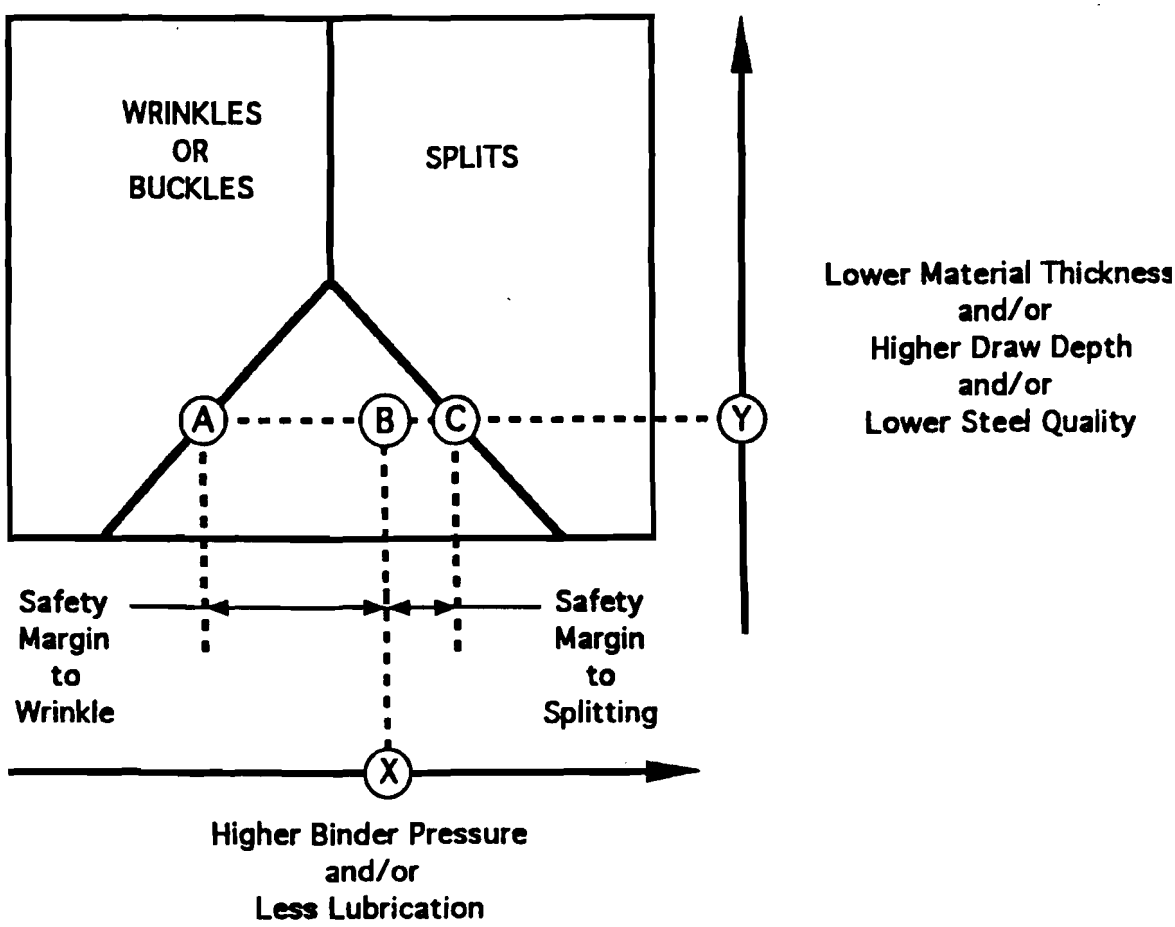

Fig. 5.4 The sketch of wrinkling and formability limits and the "drawability window" in deep drawing, [Patrishkoff, 1991]

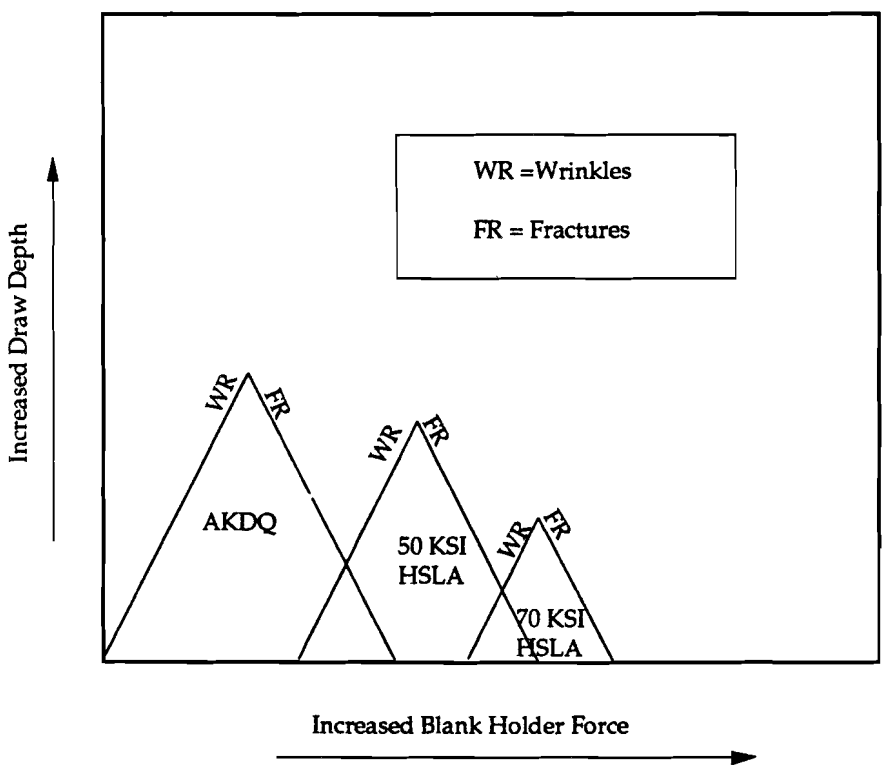

Fig. 5.5 The effect of steel strength on wrinkling and fracture limits, [Patrishkoff, 1991]

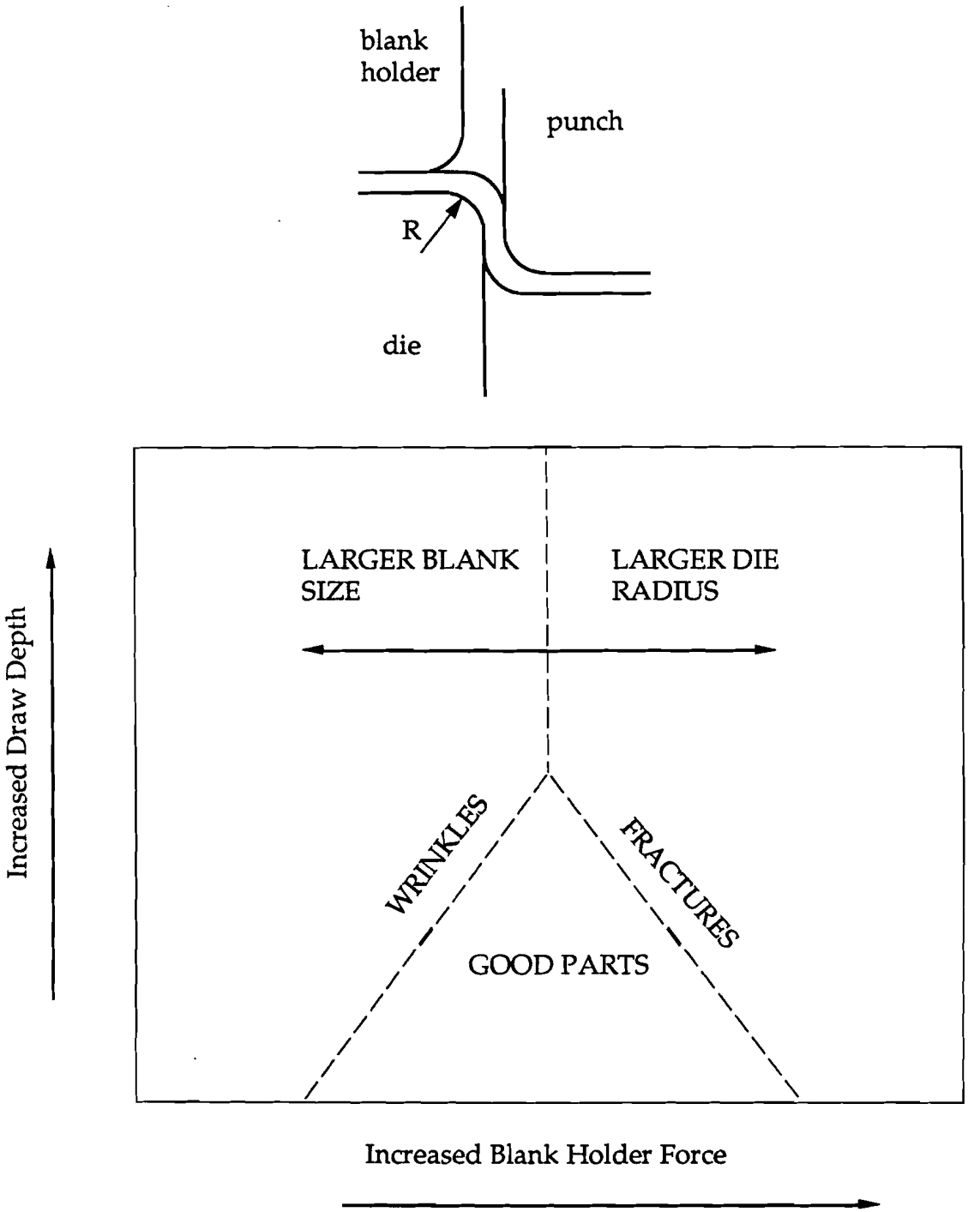

Fig. 5.6 The effect of blank size and die corner radius on wrinkling and fracture limits, [Patrishkoff, 1991]

Ohwue and Nakamachi, [1991] performed several 3D FEM simulations and experiments of the deep drawing of a square cup and found that the BHF significantly affects the thickness strain distribution. The explicit membrane-shell code "ROBUST" was used, [Ohwue and Nakamichi, 1991]. As expected, a higher BHF results in more thinning (or fracture), and less draw-in of the straight side wall. On the other hand, reducing the BHF may lead to wrinkling. Haug et al., [1991] simulated the deep drawing of a rectangular box, and the influence of the BHF was investigated. In this full 3-D simulation, wrinkling initiated in a simulation where the BHF was reduced to 80% of the initial value. As the BHF was further decreased to only 30% of the initial value, severe wrinkling occurred. The deformed cups for these three simulations (100%, 80% and 30% BHF) are shown in Fig. 5.7. One of the advantages of 3-D codes is that they are able to predict wrinkling while this is not possible when using two dimensional codes.

5.1.2 BHF Control

Ahmetoglu et al., [1992b] investigated the influence of BHF variations in drawing of round cups by performing both experiments as well as FDM simulations using SHEET_FORM. They found a significant influence of the BHF variation on the punch force distribution and strain distributions. To predict an optimum BHF variation as a function of the punch travel, it is necessary to predict the occurrence of wrinkling and fracture as accurate as possible. The criteria that are most commonly used to optimize BHF variations are punch force control, thickness strain and strain gradient control, radial stress control. A more detailed description of these studies can be found elsewhere, [Asthana, 1991]. When using the failure evaluation module, at each incremental punch travel the failure evaluation module is called after the stresses and strains are predicted. The simulation continues if failure is not predicted. If failure is predicted, a message is displayed on the screen and the user can stop the simulation and change the process and geometry data to continue.

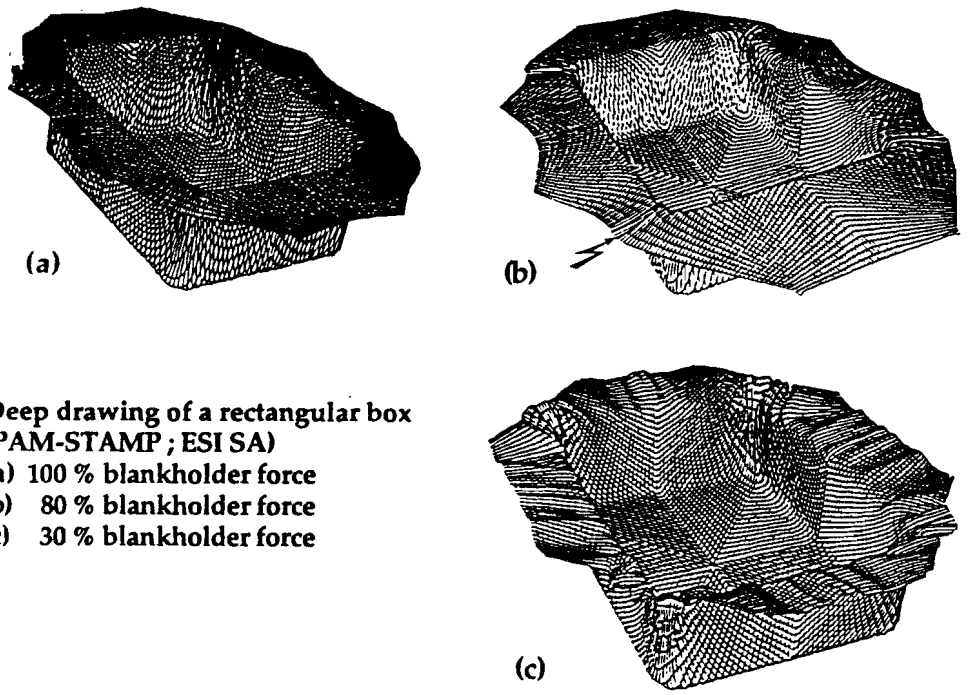

Deep drawing of a rectangular box
(PAM-STAMP ; ESI SA)
(a) 100 % blankholder force
(b) 80 % blankholder force
(c) 30 % blankholder force

Fig. 5.7 The influence of BHF on wrinkling and the ability of 3-D codes to predict the occurrence of wrinkling, [Haug et al., 1991]

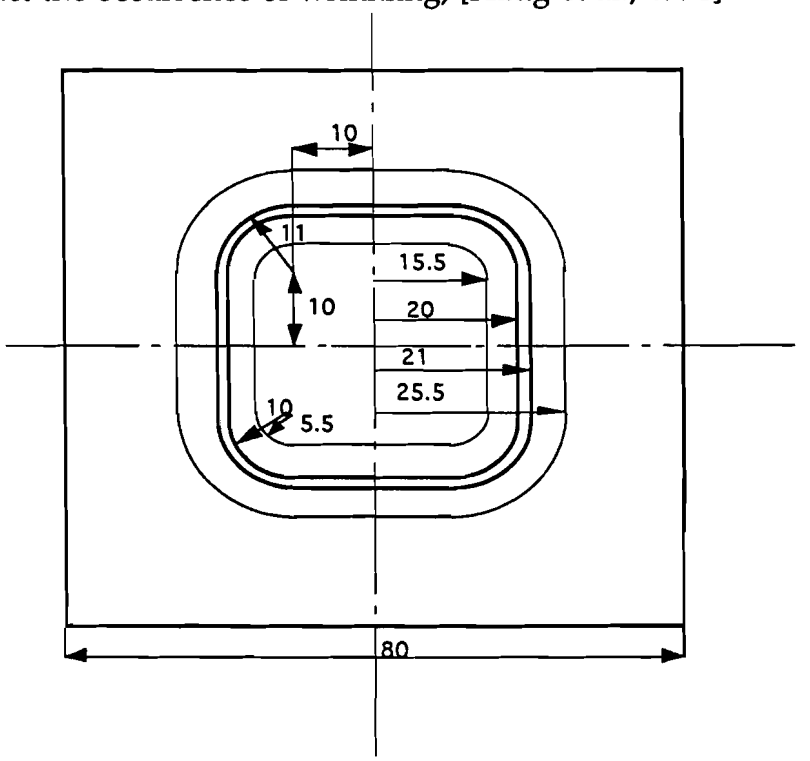

Fig. 5.8 Geometry of blank and tools as used in the experiments and simulations of square box drawing , [Darendeliler, 1991]

5.2 Three dimensional FEM simulation of square box drawing

In order to investigate the influence of the BHF more thoroughly, simulations were conducted using a 3-D FEM code SHEET_FORM-3D. The implicit code SHEETFORM-3D is based on the non-linear membrane shell approach, using the updated Lagrangian method, and is developed by Darendeliler, [1991]. The sheet is assumed to be isotropic and rate insensitive. Triangular constant strain elements are used in the mesh. It is necessary to define the elements, nodes, and the connectivity array manually which is a time-consuming process. Since the degrees of freedom increase when using the 3D formulation, the number of elements should not be very high, in order to keep the CPU within an acceptable limit. Part of the simulations are performed on the CRAY supercomputer, where the average CPU time is about one hour.

5.2.1 Comparison 3-D prediction with experiment

A simulation with a constant BHF (5 kN) and the geometry as shown in Fig. 5.8 is performed and compared with experiments performed by Darendeliler, [1991]. The material properties of the Deep Drawing (DDS) steel as used in the experiments are shown below:

K	=	560	[N/mm^2]
n	=	0.27	[-]
E	=	210,000	[N/mm^2]
ε_0	=	0.0135	[-]
t	=	0.75	[mm]
$\mu_{punch} = \mu_{d\ ie}$	=	0.04	[-]

A quarter of the blank is simulated because of symmetry using the mesh shown in Fig. 5.9. In the experiments, the strain measurements were done at a punch travel of 20 mm. Therefore the comparison with the 3-D simulations is made at this punch travel . Since the BHF is 5 kN for the whole box, the applied BHF for the quarter model is 1.25 kN. The specified friction coefficients from the experiments seem to be low. However this value is also used in the simulation.

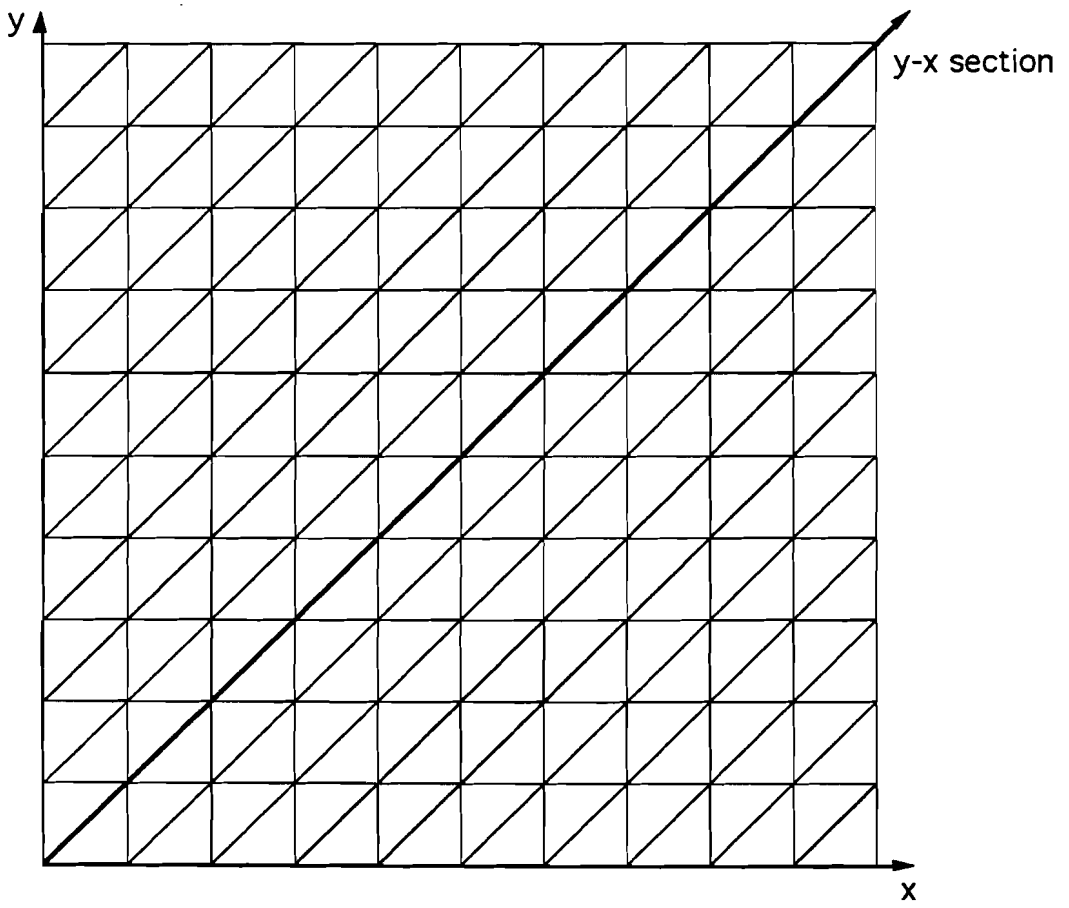

Fig. 5.9 The mesh for the quarter of the blank used in the simulation

The thickness strain distribution in the diagonal (section y-x) and at the center of the straight side walls (section y-y) from the experiments and the simulations are shown in Fig. 5.10 and Fig. 5.11 respectively. As predicted by Doege and Sommer, [1987] maximum thickness occurs in the side wall and maximum thinning occurs at the punch corner radius. The trend matches with the experiments. However, there are differences. These differences between experiment and numerical prediction are due to a) the small r_d/t ratio, which causes high bending strains as discussed before in Chapter IV, b) the friction conditions, and c) the large elements (used to reduce CPU time as much as possible).

Beginning from the center of the blank in horizontal side wall direction, thickness is nearly constant and small thinning occurs below the flat surface of the punch. Then, a sudden decrease in the sheet thickness occurs over the punch profile and maximum thinning is reached. Thickness increases between punch and die. After the die profile, thickening begins in the flange region and maximum thickness is reached at the edge. In diagonal direction, similar thinning occurs under the punch, and there is a further decrease in the thickness strain towards the punch profile. Maximum thinning occurs close to the punch corner. Thickness strain increases between punch and die. In the middle of the flange region, maximum thickness is reached, and towards the corner of the blank, the thickening gradually vanishes due to the rigid motion of the corner of the blank.

5.2.2 Influence of BHF on thickness strain and draw-in

The next step after the validation of the FEM code is to investigate the BHF effect on the thickness strain, draw-in, and load-stroke diagram. The constant blank holder force which is required to form this square cup is estimated as 1.64 kN based on Equation 5.1, [Doege and Sommer, 1986]. Then, in order to study the BHF effects, three different simulations using 0.82 kN, 1.64 kN and 5 kN BHF are performed. The BHF of 1.64 kN is calculated using a empirical relation determined by Sommer [1986]. The equation for the required blank holder pressure is given below:

$$P_{NA} = km\left(\frac{A_0}{A} - 1\right)\sigma_m \qquad (5.1)$$

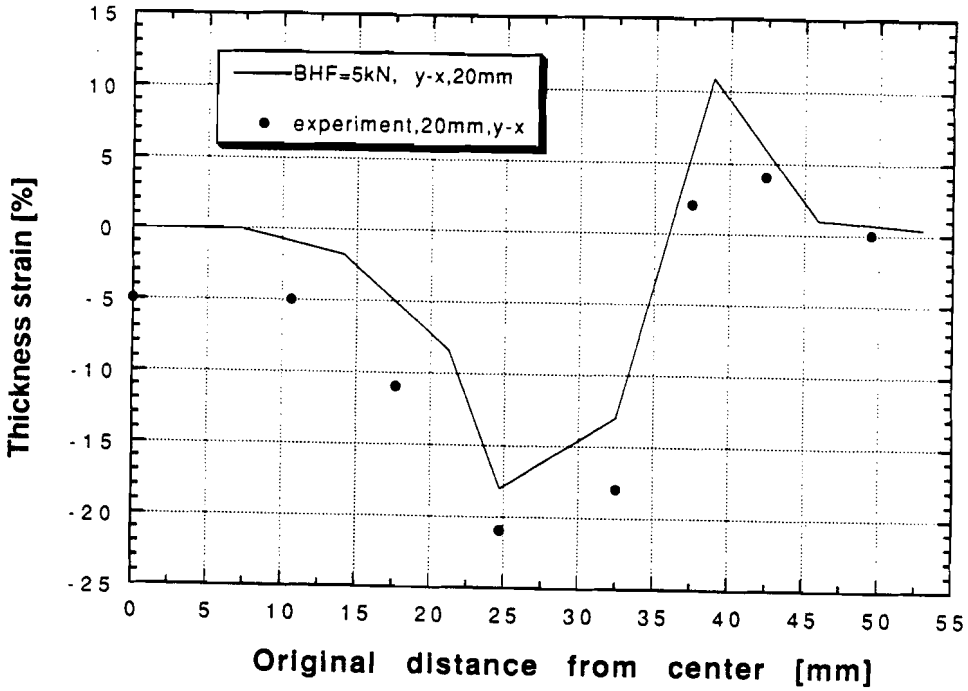

Fig. 5.10 Thickness strain distribution at a punch travel of 20 mm for both experiment and 3 - D simulation in diagonal direction (line y-x)

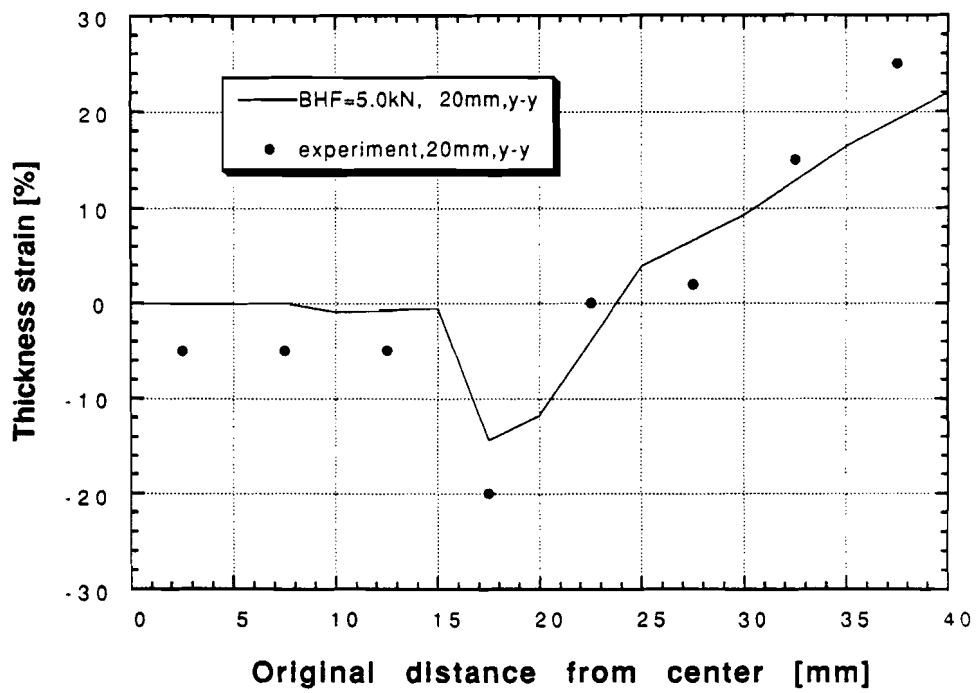

Fig. 5.11 Thickness strain distribution at a punch travel of 20 mm for both experiment and 3 - D simulation in side wall direction (line y-y)

Where:

$$k = \frac{1 + (r_{max} - r_{min})}{r_m n_m} 0.49 * 10^{-3}$$

and

$$m = 1 + \left(\frac{d_{f0}}{t_0} - 175 \right) \frac{0.17}{100}$$

Where:

A_0	= Initial surface area of blank	[mm^2]
A	= Surface area of punch	[mm^2]
σ_m	= Tensile strength	[mm^2]
r_{max}	= Maximum anisotropy	[-]
r_{min}	= Minimum anisotropy	[-]
r_m	= Average of anisotropy ($0.5*(r_{max} + r_{min})$)	[-]
d_{fo}	= Fictious diameter of square punch	[mm]
t_0	= Initial thickness	[mm]

Once the pressure P_{NA} is known, the BHF is easily calculated by multiplying it with the area of the blank located under the blank holder. Using Equation (5.1) results in a pressure of 1.68 MPa (BHF = 1.64 kN for total blank).

The thickness strains in diagonal (y-x) direction and in side wall (y-y) direction at a punch travel of 20 mm are shown in Figures 5.12. and Fig. 5.13 respectively. A higher BHF results in more thinning in both diagonal and side wall direction, while the thickening of the flange decreases. For a BHF of 5 kN, the thickness strain reaches 18%, this may start necking of the material at the punch nose, depending on the material properties and formability.

As expected the draw-in of the edge decreases for increasing BHF, however, that is not significant. In Fig. 5.14, the total draw-in at the y-y and y-x sections are shown for the three BHF as a function of the punch travel. As expected, the draw-in of the side wall (y-y direction) is higher than the corner section. The influence of the BHF is not as high as expected, probably, due to the small blank size and the relatively large corner radius and the small friction coefficient. At this moment, the FEM code has limitations in the number of elements and nodes, and it is being modified. At the time of the simulations, it was not possible to simulate a bigger blank.

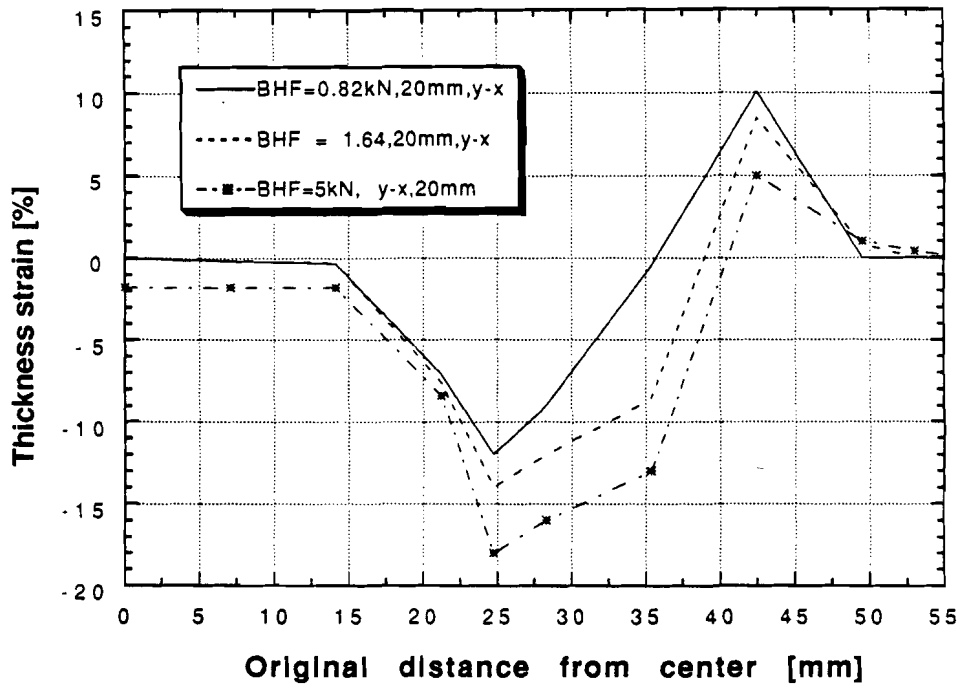

Fig. 5.12 Thickness strains at 20 mm punch travel for BHF of 0.82 kN, 1.64 kN, and 5 kN in diagonal section

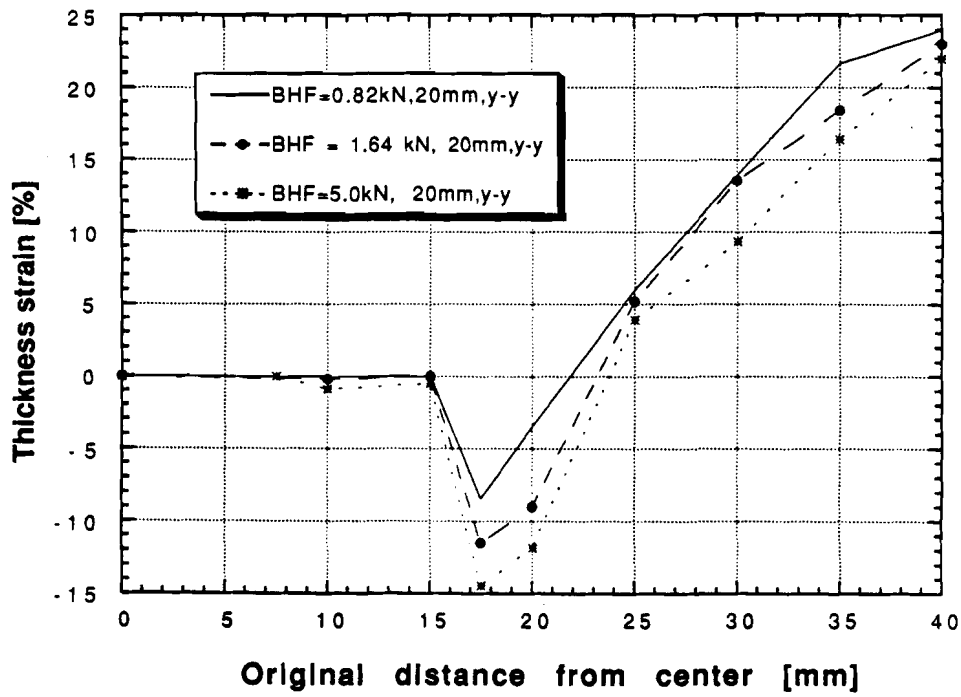

Fig. 5.13 Thickness strains at 20 mm punch travel for BHF of 0.82 kN, 1.64 kN, and 5 kN in side wall section

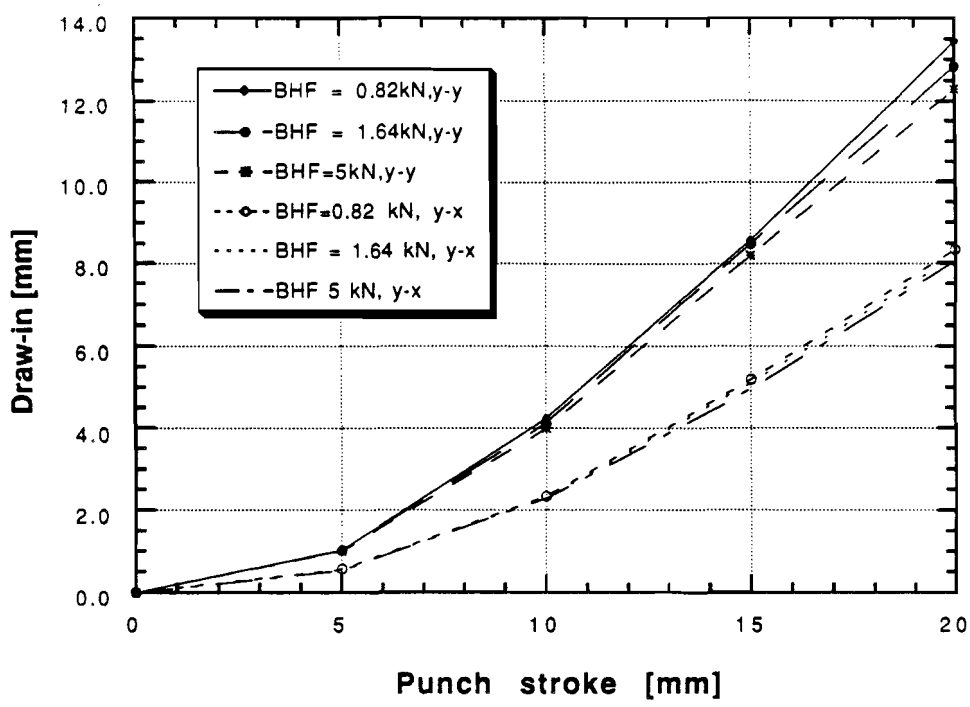

Fig. 5.14 Influence of BHF on draw-in of the side wall and the corner section

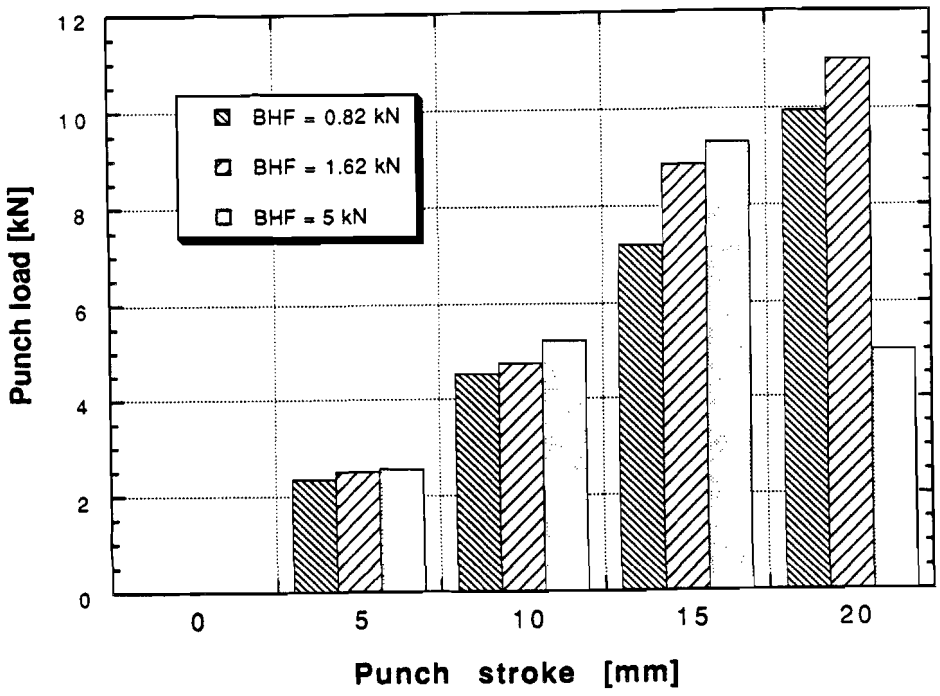

Fig. 5.15 Influence of BHF on the load-stroke diagrams (BHF are 0.82 kN, 1.64 kN and 5 kN)

The load-stroke diagram is shown in Fig. 5.15, for the three different BHF. For a BHF of 5 kN, a drop in the load occurs at 20 mm punch stroke. Since there is thinning (thickness strain ≈ 18%) at 20 mm, necking may start. Thus, the punch load decreases, due to less resistance of the material against deformation. As expected, a higher BHF results in a higher punch load.

Fig. 5.16 a, b and c show the top views of the deformed sheet for (a) BHF = 0.82 kN, (b) 1.64 kN and (c) 5 kN at a punch travel of 20 mm. From these figures, it can be seen that the outer part of the corner section hardly deforms, due to the absence of compressive stresses. The straight wall section draws in but there is only a slight difference in draw-in for different BHF.

5.2.3 Influence of locally increased BHF

To investigate the influence of a locally increased BHF in the side wall section on the draw-in and thickness strain distribution, another simulation is performed. At the straight side wall section, the original total BHF of 0.82 kN is increased 10 times for the three nodes next to the symmetry axis y-x (Fig. 5.9). Since the largest thickening occurs at the edge of the side wall this is more realistic than specifying a constant BHF on each node located on the rim. It can also be interpreted as a draw bead force. In deep drawing of large rectangular parts, draw beads are used to restrain the straight section and to prevent too much draw-in of the straight section. Since in this geometry the straight side wall is relatively small compared to the round corner section and the blank size is limited, the influence of the locally increased BHF is not expected to be significant. However, it is interesting to see the influence. The draw-in is defined as the displacement of the edge of the sheet in the die cavity direction. Fig. 5.17 shows the draw-in of both the diagonal and straight sections as a function of the punch travel for a constant BHF of 0.82 kN and the locally increased BHF (total BHF = 3.13 kN). The thickness strain distribution for two sections are shown in Fig. 5.18 and 5.19. For the locally increased BHF, the maximum thinning is higher in both the sections, while the thickening decreases, due to less draw-in.

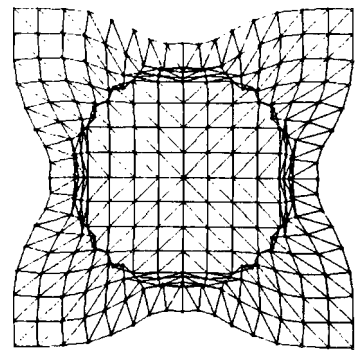

5.16 (a) BHF = 0.82 kN

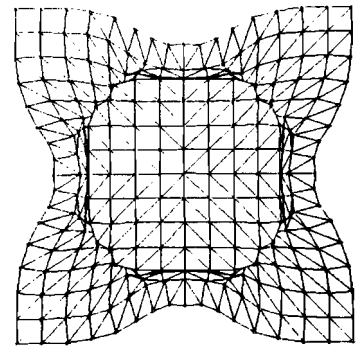

5.16 (b) BHF = 1.64 kN

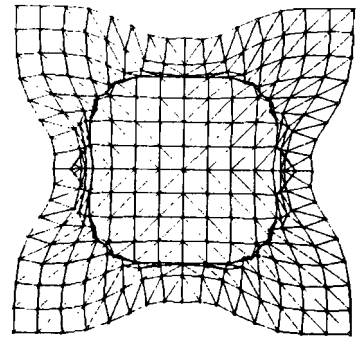

5.16 (c) BHF = 5.0 kN

Fig. 5.16 Top views of square cup at 20 mm punch travel for (a) 0.82 kN, (b) 1.64 kN and (c) 5 kN

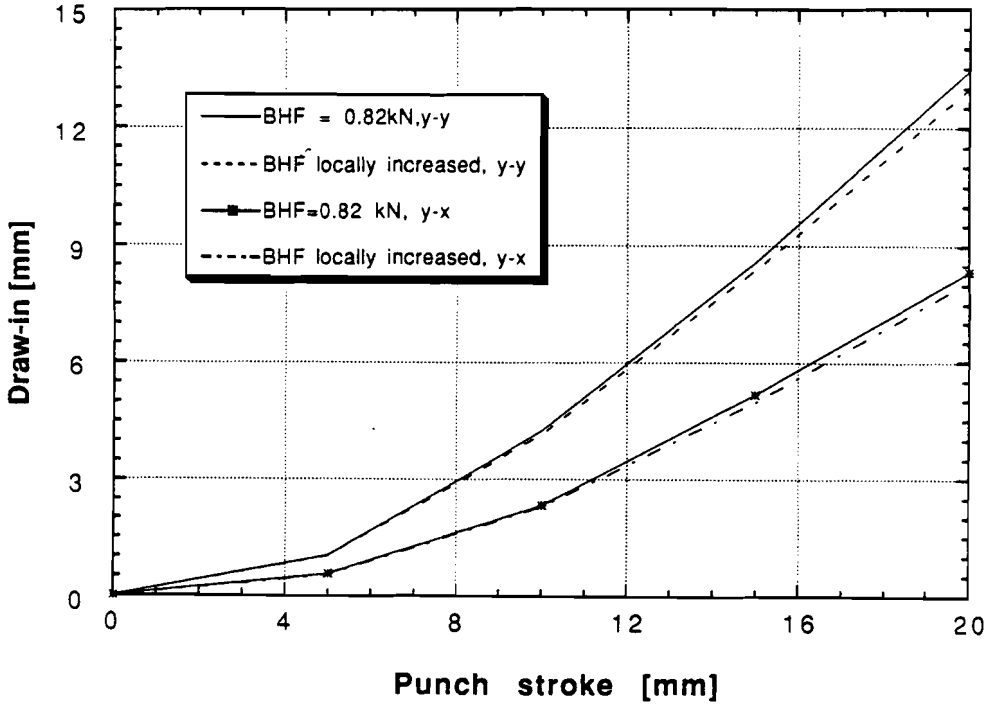

Fig. 5.17 Draw-in for constant BHF (0.82 kN) and locally increased BHF (3.13 kN)

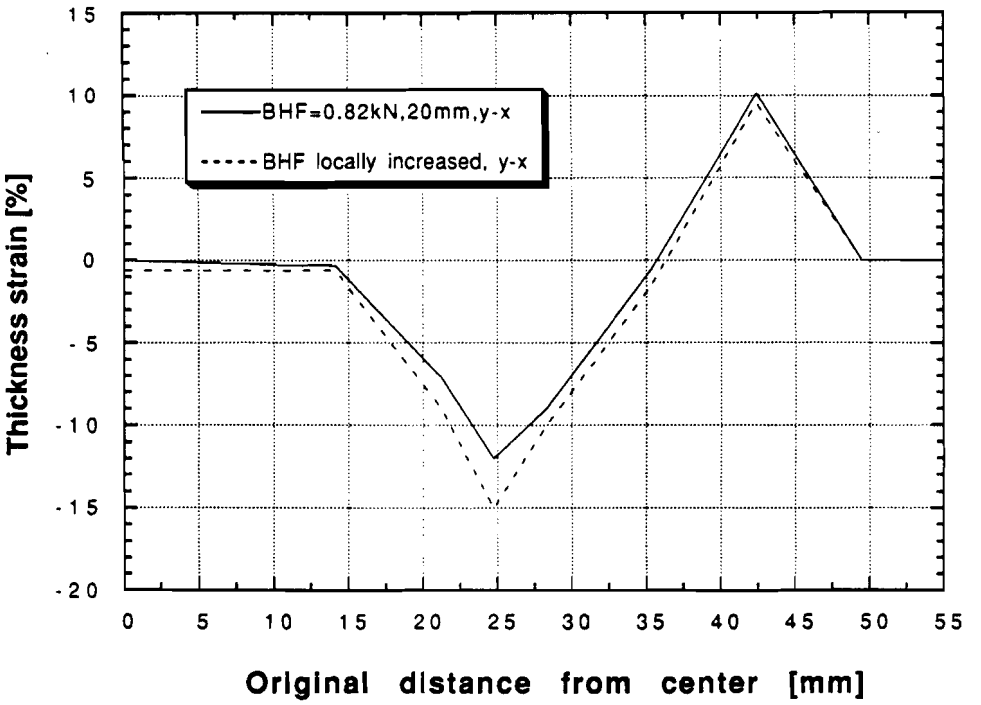

Fig. 5.18 Thickness strain in diagonal section (y-x) for constant and locally increased BHF

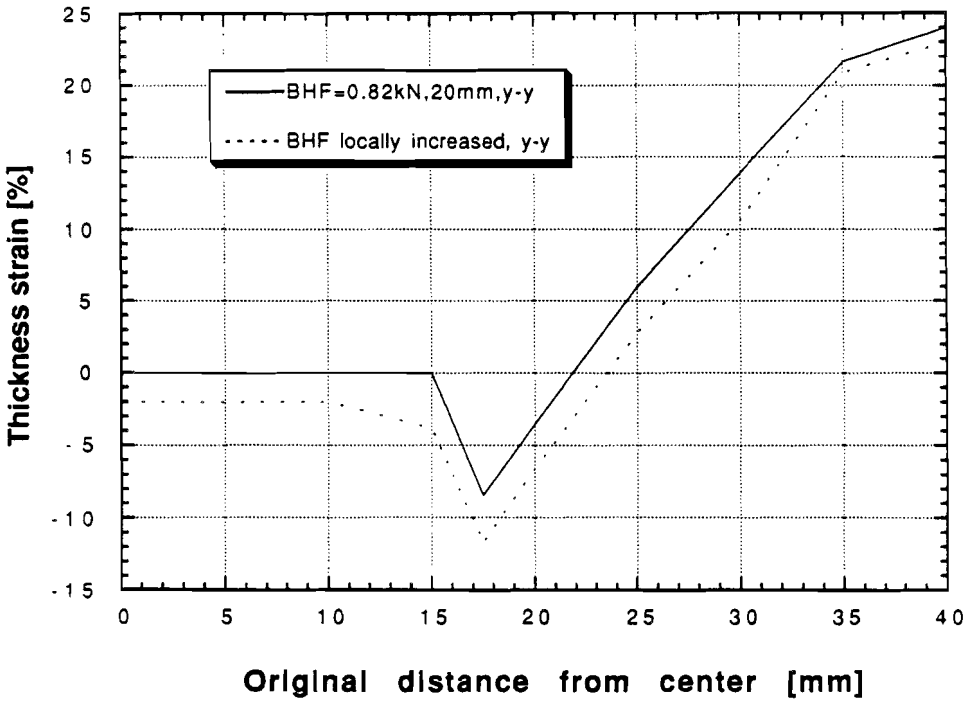

Fig. 5.19 Thickness strain in side wall section (y-y) for constant and locally increased BHF

CHAPTER VI

CONCLUSIONS AND RECOMMENDATIONS

In this report, the deep drawing of plane-strain and axisymmetric sections have been analyzed using both FEM and FDM codes. The applicability of DEFORM was investigated by comparing results from DEFORM with both experimental and other FEM codes.

The influence of the r_d/t ratio on the strain distribution was investigated using DEFORM and SHEET_FORM. A solution to include bending effects in a membrane code was investigated. In this method, inner and outer surface strains are corrected locally. This local correction means that only the radial strain values associated with the nodes of the blank contacting the tool curvatures are corrected. This improves the results considerably, depending on the value of the r_d/t ratio.

Simulations using a 3-D FEM code, SHEETFORM-3D, were performed for deep drawing of a square cup to investigate the effect of BHF on the thickness strain distribution, draw-in.

Conclusions

- The results obtained with DEFORM, such as strain distributions and load-stroke diagrams, were found to be satisfactory. The difference between predicted and measured values of radial strain are within a range of ± 0.07 (logarithmic strain), as seen in Fig. 3.13, when using a friction coefficient of $\mu = 0.13$.

- The CPU time when using DEFORM was very high (> 70 hours on a HP700s workstation) due to (a) the large number of elements required to model the blank, and (b) the contact conditions that have to be satisfied in DEFORM

(contact condition must be stabilized before another iteration is made). By modifying the automatic mesh generator (i.e. using rectangular elements instead of square elements) and modifying the contact formulation a significant decrease in CPU time can be achieved.

- For r_d/t ratios larger than 9, membrane codes provide good results, but as the r_d/t ratio is equal to or less than 9, the bending effects can not be neglected anymore. The disagreement of the results of the membrane codes with those of the solid codes can reach up to about 30% of the calculated value as seen in Fig. 4.16. Adding local bending correction improves the predictions for the surface strains. However, for small r_d/t ratios there are still discrepancies due to the global bending effects which are not corrected yet. Since there is no model to include global bending effects in axisymmetric deep drawing, one should use a solid or shell based code for small r_d/t ratios (<9) to obtain realistic strain distributions. For plane-strain deep drawing, a simple increase in either the BHF or friction coefficient may improve the results. However, the increase in the friction coefficient and/or BHF has to be determined accurately.

- In simulating deep drawing of a square cup, it is found that the BHF significantly affects the thickness strain. If the BHF is doubled, the maximum thickness strain increases up to 35% of the calculated value (Fig. 5.12 and 5.13), for the specific geometry investigated here.

- In order to improve the drawability and to prevent failure, BHF should be varied both as a function of the stroke as well as locally (variations of BHF on the blank periphery).

- The 3-D code SHEETFORM-3D, used in this study, should be equipped either with an automatic mesh generator or in conjunction with I-DEAS or another pre-processor, to reduce the required pre-processing time. In the present version of SHEETFORM-3D, the pre-processing is not flexible yet, this has to be improved. The CPU time can be decreased by minimizing the bandwith of the stiffness matrix automatically in the mesh generation. The code has to be modified to be able to define a larger number of elements. Then it is possible to simulate larger parts while using a finer mesh to investigate the BHF effects

more thoroughly and obtain more accurate strain predictions. The mesh as used in the simulations is too coarse to obtain realistic predictions.

- In the long range , it should be considered to reformulate the solver of the SHEETFORM-3D by neglecting the elastic portion of the material behavior. Instead of being elastic-plastic, the code would be rigid-plastic or rigid-viscoplastic, and the accuracy would somewhat decrease. However, the CPU time necessary to complete a deep drawing simulation would also decrease, making the code more practical for industrial use.

REFERENCES

Ahmetoglu, M.A., 1990, Kinzel, G. L. and Altan, T., "Sheet Metal Forming Processes, State of the Technology and Analysis", Report No. ERC/NSM-S-90-46, Ohio State University, Columbus, OH

Ahmetoglu, M.A., 1992a, Kinzel, G. L. and Altan, T., "Improvement of Part Quality in Stamping by Controlling Blank Holder Force and Pressure (A State of The Art review)", Report No. ERC/NSM-S-92-12, Ohio State University, Columbus, OH

Ahmetoglu, M.A, 1992b, Coremans, A.L.P., Kinzel, G. L. and Altan, T., "Deep Drawing of Round cups using Variable Blank Holder Force (BHF)", Report No. ERC/NSM-S-92-50, Ohio State University, Columbus, OH

Asthana, A., 1991, Ahmetoglu, M. A., Kinzel, G. L., and Altan, T., "Evaluation of Failure estimation and Prediction Techniques in Sheet Metal Forming", Report No. ERC/NSM-S-91-27, The Ohio State University, Columbus, OH

Batoz, J.L., 1989, Roelandt, J.M., and Pol, P.,"A membrane bending finite element model for sheet forming ", Proc. Numiform '89, ed. E.G. Thompson et al., Fort Collins, pp. 389-394

Belingardi, G., 1989, Amodio, D., Pietrosanti, C. and Goglio, L., " Improving computational and experimental results matching in sheet metal forming", Proc. Numiform'89, ed. E.G. Thompson et al., Fort Collins, pp. 395-400

Belingardi, G. , 1990, and Goglio, L., "Computer Aided Simulation of a Complete Axisymmetric Deep Drawing", 23rd FISITA Congress, The promise of new technology in the automotive industry, pp. 855-861

Besdo, D., 1991, "Constitutive laws for metal forming purposes in stress and in strain-space representation", FE simulation of 3-D sheet metal forming processes in automotive industry, VDI berichte Nr. 894, pp. 1-15

Choudry, S., 1990, and Lee, J., "Two dimensional finite element analysis of sheet forming processes including bending effects", Report No. ERC/NSM-S-90-04, Ohio State University, Columbus, OH

Darendeliler, H., 1991, Ph.D dissertation, Computer Aided Deformation Analysis of Deep Drawing, Middle-East Technical University, Ankara, Turkey

Deits, S.H, 1990, Van Tyne, C.J., and Matlock, D.K. "Finite Element Modeling of an Experimental Deep Drawing System", NAMRI/SME transactions, pp. 22-25

Doege, E., 1987, and Sommer, N., "Blank Holder Pressure and Blank holder Lay-out in Deep Drawing of Thin Sheet Metal", Advanced Technology of Plasticity, v.2, pp. 1305-1314

El-Wakil, S.D., 1980, Kamal, M.N.E.M., and Darwish, A.H., "Mechanics of the square box drawing operation of aluminum blanks", Sheet Metal Industries, Aug. 1980, pp. 679-689

Hambrecht, J., 1989, Choudry, S. Lee, J.K. and Wagoner, R.H. "Numerical study of two-dimensional sheet forming processes using bending, membrane, and solid finite element models", Proc. Numiform '89, ed. E.G. Thompson et al., Fort Collins, pp. 451-456

Haug, E., 1991, di Pasquale, E., Pickett, E., and Ulrich, D., "Industrial sheet metal forming simulations using explicit finite element methods", FE simulation of 3-D sheet metal forming process in automotive industry, ` VDI berichte Nr. 894, pp. 259-291

Hermann, M., 1988, and Lange, K., "Process modeling of sheet metal forming by the finite element method - using solid elements", Proc. 16th NAMRC , pp. 125-131

Honecker, A., 1989, and Mattiasson, K. "Finite element procedures for 3-D sheet forming simulation", Proc. Numiform '89, ed. E.G. Thompson et al., Fort Collins, pp. 457-463

Johnson, 1986, Eshel and Barash, Journal of Mechanical Work, Vol. 14, pp. 1-115

Karima, M. 1989, and Donatelli, V., "Understanding Blank Holder Effect on Formability of Sheet Metal Stamping", SAE Annual Congress and Expo., pp. 1-10

Kawai, N., 1987, Mori, T., Hayashi, H., and Kondoh, F. "Effects of Punch Cross-Section on Deep Drawability of Square Shell of Aluminum Sheet", Journal of Engineering for Industry, Nov. 1987, Vol. 309, pp. 355-361

Kobayashi, S., 1977, and Kim, J.H., "Deformation Analysis of Axisymmetric Sheet Metal Forming Processes by Rigid-Plastic Finite Element Method", Mechanics of Sheet Metal Forming, Michigan, pp. 341-365

Kobayashi, S, 1989, Oh, S.I. and Altan, T., "Metal Forming and the Finite Element Method", Oxford University Press,

Lange, K. , 1990, "Umformtechnik, Handbuch fur Industrie und Wissenschaft, Band 3: Blechbearbeitung" , Springer-Verlag, pp. 311-347, (in German)

Lee, J.K., 1990, Wagoner, R.H. and Nakamichi, E. "A Benchmark Test for Sheet Forming Analysis", Report No. ERC/NSM-90-22-2, Ohio State University, Columbus, OH

Levaillant, C., 1992, and Chenot, J.L. "Physical Modelling and Numerical Prediction of Defects in Sheet Metal Forming" Journal of Materials Processing Technology, vol. 32, pp. 383-397

Nagtegaal, J.C., 1992, and Taylor, L.M. "Comparison of Implicit and Explicit Finite Element Methods for Analysis of Sheet Forming Problems - Some Applications", Blech rohre Profile, vol. 39, pp. 298-305

Nagtegaal, J.C., 1992, and Taylor, L.M. "Comparison of Implicit and Explicit Finite Element Methods for Analysis of Sheet Forming Problems - Fundaments of calculation", Blech rohre Profile, vol. 39, pp. 389-392

Ni, C.M., 1990, and Jhita, R. "A numerical technique for predicting wrinkling in practical sheet metal forming processes", Computer modeling and simulation of manufacturing processes, ASME, MD-vol. 20, pp. 139-153

Oh, S.I., 1991, Wu, W.T. and Tang, J.P. and Vedhanayagan, K. "Capabilities and applications of FEM code DEFORM; The perspective of the developer ", Jounal of Materials Processing Technology, Elseviers Science Publishers B.V., pp. 25-41

Ohwue, T. 1991 and Nakamachi, E., "Finite element analyses of box-shaped cup drawing and comparison with experiments, VDI berichte 894, "FE-Simulation of 3-D Sheet Metal Forming processes in automotive industry, VDI Verlag, pp. 153-166

Patrishkoff. D., 1991, "Design for Manufacturability", SME Seminar on "Practical Sheet Metal Part Design", Dearborn, Michigan, April 1991

Patwardhan, A.S., 1991, "Feature extraction in Sheet Forming Process Design", Masters Thesis, the Ohio State University, pp. 128 - 144

Rebelo, N., 1989, Nagtegaal, J.C. and Hibbit, H.D. "Practical aspects of modelling sheet forming processes", Proc. Numiform '89, ed. E.G. Thompson et al., Fort Collins, pp. 31-43

Redekop, D., 1986, and Nguyen, V. "Simulation of Sheet Metal Forming Processes Using FEM", Fifth Canadian CAD/CAM and Robotics , Proc. SME, pp. 1-18

Romanowski, W.P., 1959, Handbuch der Stanzereitechnik

Saran, M.J., 1990, Schedin, E., Samuelsson, A., Melander, A. and Gustafsson, C. "Numerical and Experimental Investigations of Deep Drawing of Metal Sheets", ASME transactions, vol. 112,., pp. 272-277

Sitamaran, S.K., 1989, "A Hybrid Computer-Aided Engineering System for Process Sequence Design in Axisymmetric Sheet Metal Forming", Ph. D. dissertation, Ohio State University, Columbus, OH

Sommer, N.,1986, "Blank Holder Force and Design of Blank Holders in Deep Drawing" (in German), Doctoral Dissertation, Technical University of Hannover

Stoughton, T.B., 1985, Finite Element Modelling of 1008 AK steel Stretched over a Rectangular Punch with Bending Effects, Research Report No.-Ph.-1228, General Motors Research Laboratories,

TMEH, 1984, Tool and Manufacturing Engineers Handbook, 4th Edition, Editors C. Wick, J.T. Benedict, and R.F. Veilleux, vol. II.

Van de Koolwijk, H.P.M., 1992, FEM simulations of Deep Drawing and Redrawing Process (in Dutch), WPA report No. 1336, Eindhoven University of Technology, The Netherlands

Wang, C.T., 1992, Kinzel, G. and Altan, T. "Plane Strain Sheet Bending -Part 2- Advanced Topics, Chapter VI", Report No. ERC/NSM-S-47-92, Ohio State University, Columbus, OH

Woo, D. M., 1964, "Analysis of the cup drawing process", Journal of Mechanical Engineering Sci., Vol. 6, pp. 116-131

Woo, D. M., 1968, "On the complete solution of the Deep Drawing problem", Int. J. Mech. Sci., Vol. 10, pp. 83-94

APPENDIX A

FORMULATION OF "DEFORM"

Contact condition

The contact condition is described by the expression (A.1):

$$[v].\, n = 0 \quad , [\,t\,] = 0 \tag{A.1}$$

where
- v = velocity vector
- t = traction vector
- n = unit normal to contact surface
- $[\,]$ indicates the discontinuity across the contact boundary

Actually, Equation 3.4 expresses that the velocity and traction component in the contact surface direction is continuous, thus the condition is that no discontinuity may occur. Another condition for the traction is that, in the tangential direction, the traction should also satisfy the frictional law as in Equation (3.2) or (3.3). The interface boundary condition to describe contact between deforming bodies in variational form is given in Equation (A.2), [Oh et al, 1989]:

$$\int_S K_i.\Delta V_n.\delta\Delta V_n.dS + \int_S \delta\Delta V_s.dS = 0 \tag{A.2}$$

where
- ΔV = penetrating velocity in normal direction
- ΔV_s = sliding velocity in tangential direction
- t_s = a traction representing frictional stress
- K_i = a penalty constant, this is a large positive constant to penalize penetration

The contact conditions, as shown in Equation (A.1), cannot directly be used in FEM simulation, because of the discretization of the boundary and the kinematic

constraints imposed on the element. Therefore, in FEM the contact condition should be relaxed and imposed in an average sense, [Oh et al, 1991]. A typical contact configuration is shown in Fig. A.1. The kinematics of the contact condition in FEM can be defined by simple geometrical relations. For example, the penetrating velocity ΔV at node 1 is defined by the relative motion between node 1 and line segment 34 in normal direction to line segment 34. The penetrating velocity at node 4 is defined by the relative distance change rate between node 4 and slave side 12 in the direction normal to side 12. When the master sides 34 and 45 are not collinear, then the penetrating velocity at node 4 should be adjusted in such a way that pure sliding by slave side 12 should give zero penetrating velocity at node 4. The penetrating velocity at node 2 can be determined in the same manner. By using the penetrating and sliding velocities obtained at nodes 1, 4 and 2, the Equation (A.1) can be evaluated assuming that penetrating and sliding velocities are linearly distributed between nodes. The integration of the interface condition is carried out over the slave elements, [Oh et al, 1991].

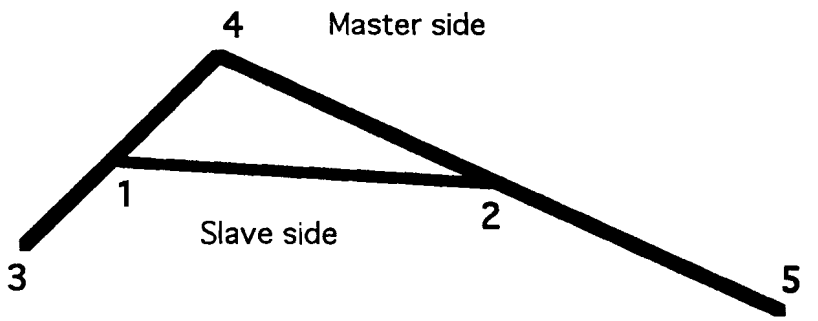

Fig. A.1. Typical contact configuration in finite element analysis, [Oh, et al. 1991]

Computational aspects and formulation

Equilibrium condition: $$\sigma_{ij,j} = \frac{\delta \sigma_{ij}}{\delta e_j} = 0 \qquad \text{(A.3)}$$

where e_j = unit vector.

Strain-rate definition $$\varepsilon_{ij} = \frac{1}{2}\left(v_{i,j} + v_{j,i}\right) \qquad \text{(A.4)}$$

where v is velocity vector

ε_{ij} is strain - rate

Levy-Von Mises

Constitutive relation $$\sigma_{ij} = \frac{2\bar{\sigma}}{3\bar{\dot{\varepsilon}}}\dot{\varepsilon}_{ij} \qquad \text{(A.5)}$$

where
σ = effective stress
$\dot{\varepsilon}$ = effective strain rate
ε_{ij} = strain rate component

Effective stress $$\bar{\sigma} = \sqrt{\tfrac{3}{2}(\sigma_{ij}.\sigma_{ij})} \qquad \text{(A.6)}$$

Effective strain rate $$\bar{\dot{\varepsilon}} = \sqrt{\tfrac{2}{3}(\dot{\varepsilon}_{ij}.\dot{\varepsilon}_{ij})} \qquad \text{(A.7)}$$

Boundary conditions
$\sigma_{ij} n_j = F_i$ on S_f (A.8a)
$v_i = v_i$ on S_v (A.8b)

where
σ_{ij} = stress component
v = velocity component

The deviatoric stress components are defined by

$$\sigma_{ij} = \sigma_{ij} - \delta_{ij}\frac{\sigma_{kk}}{3} \qquad \text{(A.9)}$$

where δ_{ij} = Kronecker delta

The field equations can be solved by a variational principle expressed as:

$$\delta\pi = \int_V \delta\varepsilon.dV + \int_V K\varepsilon_{kk}\delta\varepsilon_{mm}dV + \int_S F_i\delta v_i dS = 0 \qquad \text{(A.10)}$$

where
V = volume of workpiece
S = surface of workpiece
K = large positive constant to penalize penetration

The variational functional can be converted to non-linear algebraic equations by utilizing the FEM discretization procedure. In DEFORM, the solution of the non-linear simultaneous equations is obtained either by the direct iteration method or the Newton-Raphson method (conventional or modified), [Oh et al. ,1991].

APPENDIX B

CALCULATION OF THE SHIFT OF THE NEUTRAL AXIS

The derivation of the equations is based on the plastic volume conservation. In Fig. B1 the portion of the sheet in which the axis shifts is shown.

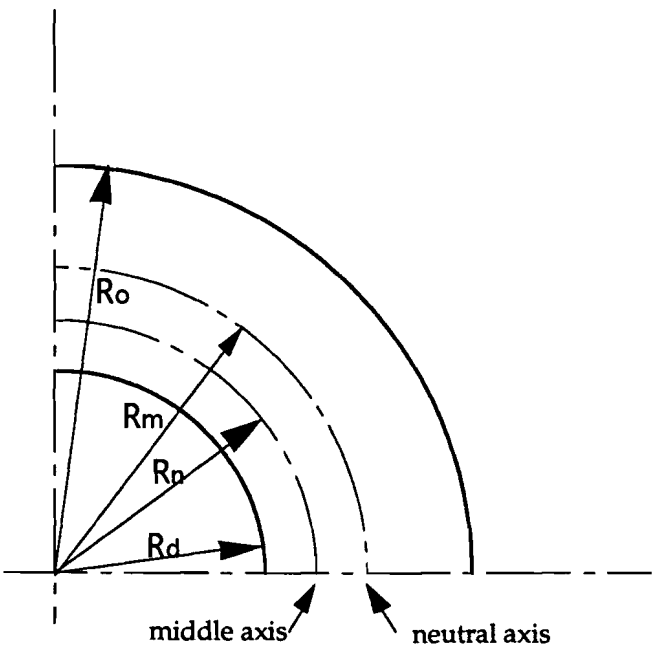

Fig B.1 Definition of the symbols as used in calculation of the shift

Radius of neutral axis: $R_n = l_0 / \phi$ (B.1)

Initial volume : $v_0 = l_0 . t_0 . w$ (B.2)

Initial area: $A_o = l_0 . t_0$ (B.3)

The width w is constant in plane-strain situation, so when applying volume conservation it is the same as area conservation.

Area conservation under the bending area:

$$A = \frac{\phi}{2}(R_e^2 - R_i^2) = A_0 = l_0 . t_0 \qquad (B.4)$$

So the bending angle can be written as :

$$\phi = \frac{2l_0.t_0}{(R_e^2 - R_i^2)} = \frac{2l_0.t_0}{(R_e - R_i)(R_e + R_i)} = \frac{2l_0.t_0}{R_m.t} \qquad (B.5)$$

Where: $t = R_e - R_i$

$$R_m = \frac{(R_e + R_i)}{2} = r_d + t/2$$

Equating the two equations in (A.1) and (A.5) results in the modified radius of the neutral axis due to thinning:

$$R_n = R_m(\frac{t}{t_0}) = (R_i + \frac{t}{2})(\frac{t}{t_0}) \qquad (B.6)$$

The approximation for the current thickness, based on volume constancy:

$$\varepsilon_{2,width} = 0 \rightarrow \varepsilon_{1,membrane} + \varepsilon_{3,thickness} = 0 \qquad (B.7)$$

Then $\ln(\frac{t}{t_0}) = -\varepsilon_{1,membrane} \rightarrow t = t_0.e^{-\varepsilon_{membrane}}$ (B.8)

The radius of the neutral axis can now be written as :

$$R_n = (R_i + t_0/2.e^{-\varepsilon_{membrane}})e^{-\varepsilon_{membrane}} \qquad (B.9)$$

The shift can be written as in Equation (B.10):

$$d = R_m(1 - \frac{t}{t_0}) = (R_i + t_0/2.e^{-\varepsilon_{membrane}})(1 - e^{-\varepsilon_{membrane}}) \qquad (B.10)$$

APPENDIX C

BENDING , SLIDING, AND UNBENDING EFFECTS DURING IN-PLANE TENSION

The moment equilibrium of a sheet, which is bent conform to the die radius (Fig. 4.4) , and subjected to sliding and unbending is given in Equation (C.1)

$$(T + dT)R_m + (M + dM) - M - T.R_m - F.r_d = 0 \qquad (C.1)$$

Where the friction force F is given by Equation (C.2):

$$e^{\mu(\phi_0 - \phi).r_d / R_m} \qquad (C.2)$$

The relationship between P and T is obtained by force equilibrium in radial direction, using a membrane approximation (neglecting bending moments), and ignoring.

$$P.r_d.d\phi = 2T\sin(\frac{d\phi}{2}) \qquad (C.3)$$

The solution is:

$$T = P.r_d \qquad (C.4)$$

Substituting (C.2) and (C.4) in (C.1) results in:

$$dT + \frac{dM}{R_m} = \mu(\frac{r_d}{R_m})T.d\phi \qquad (C.5)$$

To integrate (C.5) easily an approximation for the force T is made, based on a modified foil-friction formula [Wang, 1983].

$$T = \frac{1}{2}\left[T_b e^{\mu\phi_0 . r_d / R_m} + T_s e^{\mu(\phi_0 - \phi).r_d / R_m}\right] \qquad (C.6)$$

Integration Equation (C.5) from $\phi = 0$ to ϕo (outlet of the bend) gives the draw force after sliding and unbending. The draw force is written as in Equation (C.7)

$$T_s = T_b.e^{\mu\phi_0 . r_d / R_m} - \frac{2}{1 + e^{-\mu(\phi_0 - \phi).r_d / R_m}} \frac{M_s - M_b}{R_m} \qquad (C.7)$$

The calculation of M_b in Equation (C.7) is derived now:

The axial stresses are defined by Equation (C.8) for elastic bending and Equation (C.9) for plastic bending with Hollomon's hardening law (pre-strain assumed to be zero):

$$\sigma_x = E'\varepsilon_x \quad \text{when} \quad \varepsilon_x \le \varepsilon_0 \tag{C.8}$$

$$\sigma_x = K(F\varepsilon_x)^n \quad \text{when} \quad \varepsilon_x \ge \varepsilon_0 \tag{C.9}$$

With: $E' = \dfrac{E}{1-\nu^2}$,

$\bar{\varepsilon} = F\varepsilon_x$,

and $\bar{\sigma} = K(\bar{\varepsilon})^n$

Where:

ε_0	=	Yield strain	[-]
σ_x	=	Stress in x-direction	[N/mm^2]
ε_x	=	Strain in x-direction	[-]
E	=	Young's modulus	[N/mm^2]
υ	=	Poisson's ratio	[-]

F is a correlation index to consider influences of material normal anisotropy and the stress/strain state. The expression of F depends on the yield theory used. For plane-strain, using Hill's old and new yield criteria, F is written as:

Valid for transverse anisotropic materials, plane-strain, [Hill, 1948]:

$$F = \frac{1+R}{\sqrt{1+2R}}$$

Valid for transverse anisotropic materials, plane-strain, [Hill, 1979]:

$$F = \frac{[2(1+R)]^{1/M}}{2}\left\{1+(1+2R)^{\frac{1}{1-M}}\right\}^{\frac{M-1}{M}}$$

Considering only the elastic-plastic deformation in secondary plastic bending. The characteristic strains, i.e. the yield strain ε_0, the maximum strain at outer convex surface, ε_{max}, and the strain at the inner concave surface, ε_i, are found to be:

$$\varepsilon_0 = \frac{\sigma_0}{E'} \tag{C.10}$$

$$\varepsilon_i = -\ln(1 + \frac{t/2 - d}{R_d}) \tag{C.11a}$$

$$\varepsilon_{max} = \ln(1 + \frac{t/2 + d}{R_d}) \tag{C.11b}$$

Where σ_0 is initial yield stress, and d is the shift of the neutral axis, measured from the middle axis. These strains are necessary to calculate the bending moment M_b.

Bending moment per unit width is defined as in Equation (C.12):

$$M = \int_{-t/2}^{t/2} \sigma_x . y . dy \tag{C.12}$$

This equation has to be integrated. This complex integration is derived in [Wang, Kinzel, and Altan, 1992]. The final result after integration is as in Equation (c.13):

$$M = \frac{2}{3} R_n^2 E' \varepsilon_o^3 + K F^{n+1} R_n^2 \left\{ \frac{1}{n+2} \left[\varepsilon_{max}^{n+2} - 2\varepsilon_0^{n+2} + \varepsilon_i^{n+2} \right] + \frac{3}{2(n+3)} \left[\varepsilon_{max}^{n+3} + \varepsilon_i^{n+3} \right] \right\} \tag{C.13}$$

All the characteristic strains are defined in Equation (C.10) and (C.11a and C.11.b). These strains are a function of the shift distance of the neutral axis, d, the bending radius (i.e. the die corner radius), r_d and the sheet thickness t. Therefore, once the membrane strain is known from the membrane codes, the shift of the neutral axis can be calculated. Then the characteristic strains can be calculated, and from these strains the bending moment M_b , which is required to calculate the increase in tensile force T_s, can be calculated.